OPERANDO OPTICAL AND QUANTITATIVE ELECTROCHEMICAL STUDIES OF SOLID OXIDE FUEL CELL ANODE DEGRADATION AND REGENERATION

by

Elias Deen Pomeroy

A dissertation submitted in partial fulfillment

of the requirements for the degree

of

Doctor of Philosophy
in
Chemistry

MONTANA STATE UNIVERSITY
Bozeman, Montana

January 2022

DEDICATION

For Lyndon Fayne Pomeroy

ACKNOWLEDGEMENTS

First, I would like to thank my Advisor, Prof. Robert Walker, for his mentorship and empowering me to pursue my own research interests. I would also like to thank our collaborators at NRL, especially Dr. William Maza, Dr. Daniel Steinhurst, and Dr. Jeff Owrutsky for all their help with research, writing, and making me feel at home in Washington, DC. Thank you to past members of the Walker Research Group, especially Dr. Märtha Welender and Dr. Melissa McIntyre, for answering all my questions and showing me the ropes. Thank you to my committee members, Prof. Roberta Amendola, Prof. Erik Grumstrup, Prof. Stephen Sofie, and Prof. Nick Stadie for their insightful instruction, thoughtful questions, reasonable suggestions, and patiently listening to me during meetings. Thank you to Dr. Doreen Brown for her tireless assistance navigating through the graduate school details and paperwork. And thank you to Dr. Craig Ogilvie, for being a Graduate Dean on the side of the graduate students.

I would also like to thank my father, Deen Pomeroy, for his assistance and advice designing high temperature furnaces and the other arts and crafts projects during my dissertation research. Last, but not least, I would like to thank Sarah Hopfner for her endless support.

TABLE OF CONTENTS

TABLE OF CONTENTS CONTINUED

TABLE OF CONTENTS CONTINUED

LIST OF TABLES

Table Page

LIST OF FIGURES

Figure Page

LIST OF FIGURES CONTINUED

Figure Page

LIST OF FIGURES CONTINUED

Figure Page

ABSTRACT

Solid Oxide Fuel Cells (SOFCs) are high temperature (600-1000 °C) devices that can generate electricity with extremely high efficiencies from a wide variety of fuels, including H2, CH4, Biogas, and crushed coal. Unfortunately, the SOFC anodes are highly sensitive to gas phase contaminants, including sulfur and carbon containing fuels. Sulfur is ubiquitous in all carbon containing fuels, with concentrations as low as a few parts per million to as high as 1% by mass. At all concentrations sulfur substantially decreases SOFC performance. Conventional models propose that sulfur decreases fuel cell performance by blocking anode active sites, preventing electrochemical reactions, and reducing surface area for heterogeneous catalysis. Carbon containing fuels can rapidly degrade SOFCs due to graphitic carbon formation. Graphite blocks active sites on the anode, causes damage within the anode microstructure, and removes electrocatalytic material via metal dusting. Studies presented in this work used *operando* optical techniques and quantitative electrochemistry to study degradation and remediation of SOFC anodes. First, since typical electrochemical techniques infer microstructural changes rather than directly measuring surface area, a traditional electrochemical technique, chronocoulometry (CC), was adapted to SOFCs for the first time to measure the electrochemically active area of the anode. This technique showed that active area is temperature dependent, and that sulfur participates in electrochemical reactions, decreasing performance with sluggish oxidation kinetics, rather than simply blocking active sites. Carbon monoxide, on the other hand, decreased the number of active sites, rather than participating in electrochemical reactions, either by blocking active sites or forming carbon. Then, a comparative study was undertaken of different methodologies of carbon remediation, comparing electrochemical oxidation, molecular oxygen, and steam as methods to remove graphite accumulated on SOFC anodes. This study found that with all methods, CO2 played a key role in removing carbon, that both electrochemical oxidation and steam removed carbon more globally than oxygen, and that imaging the entire cell is critical for understanding the complex, spatially and temporally heterogeneous chemistry occurring across SOFC anodes. Finally, sulfur was employed to passivate SOFC anodes operating on dry methane, significantly reducing carbon formation with only slight decreases in electrochemical performance.

CHAPTER ONE

INTRODUCTION

Motivation and Background

Solid Oxide Fuel Cells (SOFC) are a promising technology that can radically reduce CO_2 emissions, thus lessening the stress on global warming while still utilizing many of the fuels that are currently employed by traditional combustion-based energy production processes. Furthermore, SOFCs are also well suited to producing electricity from renewable fuels such as H_2 from water hydrolysis and plant-based biofuels.

SOFCs are electrochemical conversion devices that oxidize fuels to generate electricity. Since they produce their energy electrochemically, SOFCs can achieve conversion efficiencies as high 88% with combined heating and power applications.[1] Some SOFCs can also operate in reverse, converting CO_2 and H_2O into synthesis gas (syn-gas), a mixture of CO and H_2. As the name synthesis gas would suggest, CO produced by electrolysis can then be converted into a variety of high-value hydrocarbons through the Fischer-Tropsch process.[2]

While SOFCs have great potential to change the complexion of power generation strategies, their durability is limited. SOFCs are susceptible to a number of degradation pathways, including metal particle sintering, C formation on anodes, and a number of contaminants in both the oxidant and fuel feeds. Of these degradation pathways, sulfur in the incident fuel and C formation have been the focus of my doctoral research. Research described in this dissertation adapted a traditional electrochemical technique –

chronocoulometry – to characterize SOFC microstructure in a manner never before attempted, and with careful application of combined optical techniques, mass spectrometry, and electrochemistry the mechanisms of C remediation on SOFC anodes were explored. The result of these later studies is a comprehensive and detailed roadmap describing how different carbon removal strategies lead to heterogeneous chemistry across electrocatalytic anodes in functioning SOFCs.

Solid Oxide Fuel Cells

Solid Oxide Fuel Cells are composed of two electrodes, chosen for their electro-catalytic activity, separated by an ionically conductive ceramic electrolyte. At the anode, fuel is oxidized to produce electrons. H_2 is oxidized to produce H_2O, and C containing fuels are oxidized to produce CO_2 and H_2. The electrons generated at the anode pass through an external circuit to perform work and are then consumed at the cathode where molecular oxygen is reduced to produce oxide ions that diffuse through the electrolyte to the anode. A representative schematic of electrolyte supported, and anode supported cells are included in Figure 1.

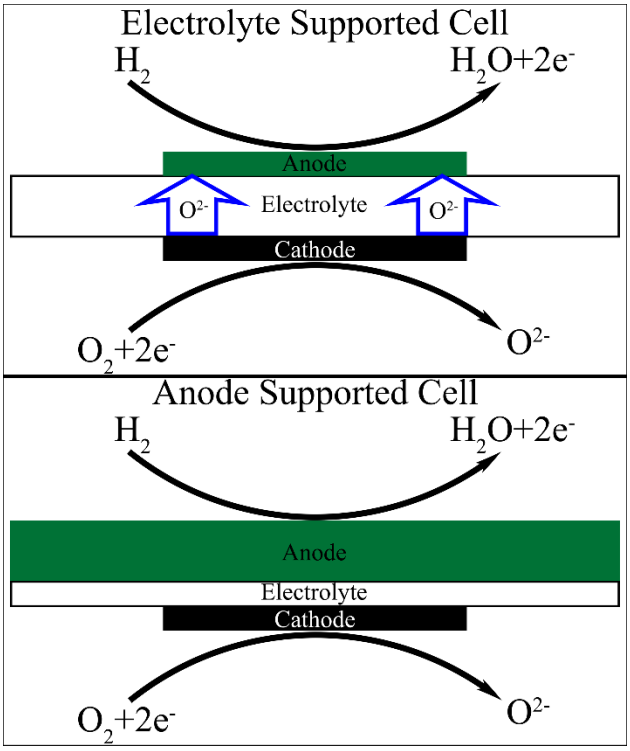

Figure 1 Illustration of electrolyte supported (top) and anode supported (bottom) SOFC

The critical component of SOFCs is the electrolyte, an oxide conducting ceramic. The most common electrolyte is cubic zirconia stabilized with 8% (by mol) yttria. The yttria both stabilizes the cubic structure of zirconia and generates oxide vacancies in the zirconia's crystal lattice. Both of these effects increase the oxygen conductivity of the electrolyte[3]. The activation energy of oxygen diffusion is about 100 $\frac{\text{kj}}{\text{mol}}$, and as a result SOFCs must operate at high (>600 °C) temperatures to create sufficient oxide flux for usable currents.[4]

Cathode materials must combine catalytic activity, ionic and electronic conductivity, and good thermal expansion match to the other cell components. Typically, this material is a mixed ion-electron conductor (MEIC) such as the perovskite material $La_{0.85}Sr_{0.15}MnO_3$

(LSM). The substitution of Sr for La generates electron holes, that produce the electronic conductivity of the material.[5] SOFC cathodes, while important, will not be the focus of this research proposal.

This thesis focused on SOFC anode material degradation and regeneration. SOFC anodes have similar requirements to the cathodes, and for this reason a Ni-YSZ ceramic metallic composite is usually chosen.[3] Ni is electronically conductive and has excellent catalytic activity for a variety of fuels, including H_2, CH_4, crushed coal, and even NH_3.[6-8] Ni is also relatively inexpensive as compared to precious metal catalysts, such as the Pt catalysts used in PEMFCs. Ionic conductivity comes from mixing Ni with additional YSZ to form a ceramic-metallic (or cermet) composite. Anodes are typically produced by mixing NiO powder with YSZ with appropriate stoichiometries, then sintering at high temperatures. The NiO is then reduced with hydrogen *in-situ* to create a porous Ni-YSZ cermet simultaneously increasing the TPB length and dispersing the Ni particles to increase their active surface area. The cermet structure also has the added effect of making SOFC structures heterogeneous, which makes their chemical behavior complex. The performance of the fuel cell is enhanced by optimizing important parameters of the two primary reactions that occur in SOFC anodes, illustrated in Figure 2 below.

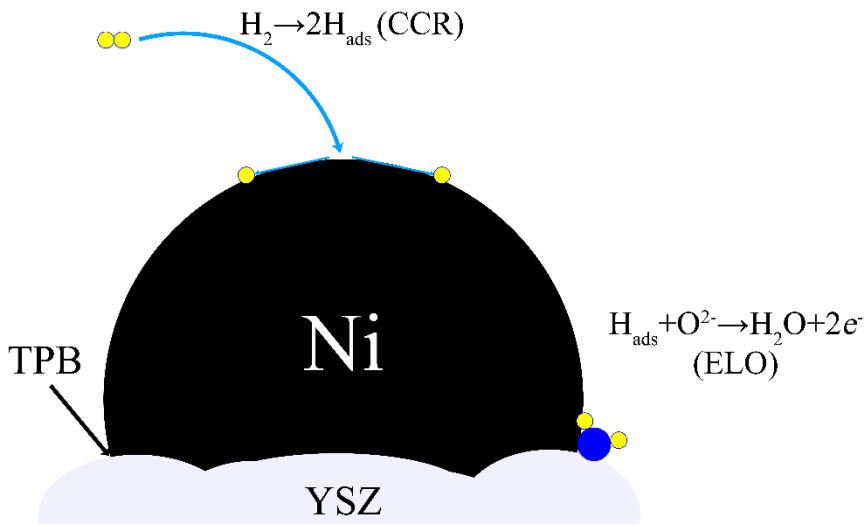

Figure 2 Schematic representation of CCR and ELO reactions

The first reaction is the catalytic cracking of the fuel on the Ni surface (CCR), a process enhanced by the increased surface area. The simplest example of this reaction occurs with hydrogen as follows:

$$H_{2(g)} \longrightarrow 2H_{Ads} \quad (1)$$

The second reaction is the electrochemical oxidation (ELO) that occurs at the three-phase-boundary (TPB) where the electronically conducting Ni, ionically conducting YSZ, and gas phase fuel mixture all meet:

$$2H_{ads} + O^{2-} \rightarrow H_2O(g) + 2e^- \quad (2)$$

An SOFC's electrochemical performance is directly tied to the EO reaction, since the exchange current is directly proportional to the TPB length, but additional adsorbed species provided by the CCR also increase the rate.[9] One goal of my research was to determine the effects of fuel stream contaminants on each of these reactions and the resulting impact on SOFC performance.

SOFC Degradation

While SOFCs remain a promising electrical power generation technology, their durability remains susceptible to S and C induced degradation of Ni-YSZ cermet anodes. Studying how SOFC anodes degrade in functional devices is challenging due to the high temperatures, strongly oxidizing/reducing polarizations, complex electrode structure, and need for dual atmosphere environments. Fuel cell degradation occurs by limiting one of the two previously discussed reaction pathways, either by limiting the catalytic surface area for CCR, or blocking TPB sites for ELO.

S is the most common and well-studied SOFC fuel contaminant. S can be found in nearly all C containing SOFC fuels, including biogas, reformed coal gas, natural gas, and diesel reformate.[10] S concentrations range from the 5 ppm added to natural gas as a safety odorant to more than 1% by mass in sour natural gas.[11] Removing H_2S from fuel streams can be done using wet scrubbers, though if very clean fuels are required catalytic sorbents may be necessary (e.g. ZnO).[12] For higher weight fuels that may have S incorporated into the C chain, catalytic desulfurization needs to be performed prior to utilization.[13] Unfortunately, even small levels of S added back to the gas as an odorant can have deleterious effects on SOFC anodes, especially at lower temperatures.[14, 15] Fuel cell performance degrades rapidly, at partial pressures as low as 0.2 ppm. This degradation is S concentration dependent, and, depending on the operating temperature and fuel composition, can achieve an apparent saturation effect at partial pressures as low as 5 ppm.[14] Performance degradation is also temperature dependent, increasing sharply and becoming irreversible at temperatures below 850 °C.[14]

Two mechanisms are thought to be responsible for S degradation, reversible S adsorption and irreversible sulfide formation. Based on thermodynamic calculations sulfide formation occurs only at partial pressures of S greater than 1%, even at 800 °C, making sulfide formation less likely in SOFC applications.[14] In a study by Hagen *et. al.* the sulfur tolerance of anode supported cells with Ni-YSZ anodes and YSZ electrolytes were compared to cells with Sc doped YSZ in both anodes and electrolytes.[16] The precise Sc doping is not reported in this or a previous publication which detailed cell manufacturing in more detail.[17] The cells used H_2 rich humidified CH_4 at 850 °C for 500 hrs., and were then analyzed using SEM. Irreversible performance degradation was only observed in the non-doped samples, and SEM imaging revealed decreased Ni percolation near the electrolyte, see Figure 3.

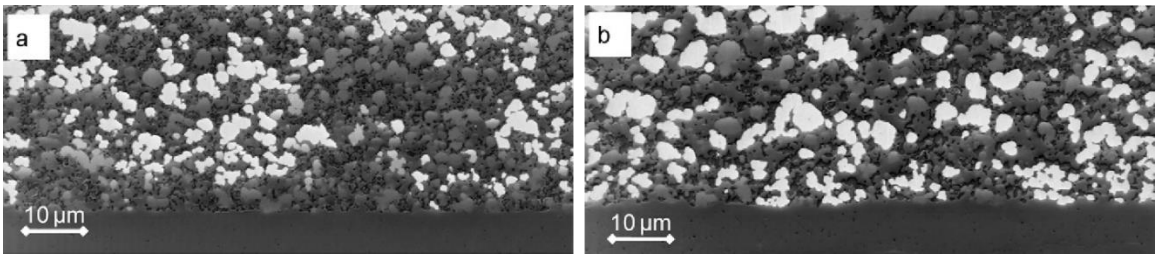

Figure 3 Polished cross sections of the electrolyte/anode interface of a) Ni-YSZ-LSM and b) Ni-ScYSZ-LSM cells, the dark layers are electrolyte material, and the light spots are percolated Ni particles in the anode.[16]

These results then explain that the irreversible degradation that occurs below 850 °C results from loss of percolated Ni particles near the electrode/electrolyte interface.[16]Additionally, fuel identity also plays a role in anode degradation. In a study by Sasaki *et. al.* also comparing S tolerance of 8%-YSZ and 10%-ScSZ cells, cells were operated at 850 °C using syngas at varying H_2/CO ratios. Cell degradation was consistent at high H_2/CO ratio,

but when H_2/CO became sufficiently low, ~ 0.1 ppm, degradation was extensive, and the cell was no longer able to oxidize fuel. This observation indicates that S could be selectively poisoning SOFC anodes, permitting H_2 oxidation while preventing CO oxidation. This study also found that the ScSZ cells were more tolerant to sulfur poisoning than the YSZ cells.[14] The selective nature of S poisoning could point to a method to improve SOFC performance by minimizing another important SOFC degradation pathway, C formation.

Since S can be removed from a fuel stream, graphitic C formation remains the primary degradation pathway for SOFCs operating with C containing fuels.[18-24] C degrades SOFC performance by blocking catalytic surface area, TPB sites for electrochemical performance, and can eventually cause Ni loss in the cell via metal dusting.[19] Conditions for C formation are dependent on C-H-O ratios, temperature, and electrochemical polarization.[25] Sasaki *et. al.* performed thermodynamic calculations to construct ternary diagrams for C formation at a variety of temperatures and fuels, see Figure 4.

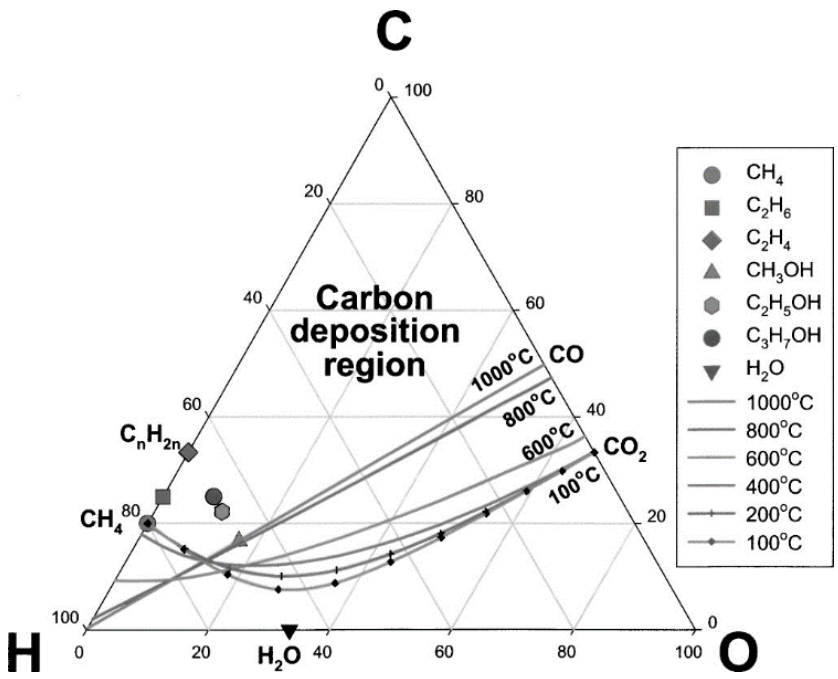

Figure 4 C-H-O diagram indicating when C will form at different temperatures and where certain fuels lie on this diagram.[25]

These conditions are a helpful starting point for determining whether C is likely to form given a mixture of fuel and oxidizers, but since these calculations do not take into consideration other conditions likely to be present in an SOFC environment (catalytic surfaces, non-faradaic oxide flux through the electrolyte, small leakages from environment) etc., and that SOFCs are intrinsically not a system at thermodynamic equilibrium, C formation must still be studied empirically. C formation on SOFCs is typically studied electrochemically by monitoring how electrochemical performance changes under conditions where C is likely to form.[26-31] Koh *et. al.* monitored cell performance with methane at different thermodynamic and electrochemical conditions to assess whether fuel cell performance degradation was reversible or irreversible. The authors reported that in conditions where C formation was not thermodynamically favored,

e.g. humidified methane, cell performance losses were reversible and less severe than under dry methane, where cell performance losses were irreversible. The higher degree of cell performance loss and irreversible cell damage was assigned to more extensive C formation. The degree to which C has formed is occasionally measured *ex situ*, using scanning electron microscopy (SEM) imaging, or temperature program oxidation (TPO) to quantify carbon deposition.[26, 28, 29] For example, in a study performed by Alzate-Restrepo, *et al.*, C formation on SOFC anodes at 800 °C with differing CO to H_2 ratios. Surprisingly, the amount of C deposited was least under CO alone, with the most at 3:1 CO:H_2 ratio. Further increases in H_2 led to decreasing amounts with deposited C. C formation on Ni based catalytic systems have been well studied for decades, and a number of C mitigation strategies for those systems have been applied to SOFCs, including the use of reforming agents, such as steam and oxygen, and doping either Ni or YSZ with alternative materials in an attempt to promote C tolerance.[19, 27, 32, 33] In the study by Niakolas, *et al.*, Au doped Ni-GDC anodes were operated with CH_4 and substoichiometric amounts of steam. The authors observed no significant decrease in performance over 200 hrs, an effect attributed to a lack of C formation. These methods appear to be successful in improving C tolerance but impose increased material processing costs or dramatically reduce cell performance, either by diminishing electrical efficiencies or by blocking active sites in the TPB. In the analysis done by Iotme, methane oxidation rates using Co, Fe, and Cu based electrodes all saw increased C tolerance, but decreased electrocatalytic activity.[32] Additionally, even with a highly tolerant material, C formation can still occur, reducing electrochemical

performance. In such cases, a method for C remediation much be employed to remove C from the anode.

Carbon remediation is less commonly studied, with more studies in the literature focused on developing C tolerant materials.[19, 27, 32-34] Researchers who have considered carboon remediation typically focus on maximizing SOFC recovery after C deposition, employing a mixture of oxidizing and reducing agents to remove C without causing significant changes to electrode microstructure.[30, 35, 36] Subotić *et. al.* employed a variety of C gasification strategies to return a pre-coked anode supported cell to previous performance, with the best being a mixture of H_2 and H_2O, able to return the cell to full performance after 44 hrs. While useful, these studies do little to explore the mechanisms of C remediation. Research intent on identifying mechanistic details of carbon removal have been performed by this group and others, combining non-invasive optical methods such as Raman Spectroscopy with electrochemical measurements to quantify C deposition, as well as determine the relative rates of carbon removal and cell damage done with different C removal strategies.[20, 37, 38] In one report, authors found that steam appeared to remove C most rapidly, being followed by O_2 and CO_2.[37] O_2 appeared to cause the most damage to cell microstructure, with steam causing the least.[37] Experiments using electrochemical methods to remove C found NiO formed once nearly all C had been removed from the cell, and reported significant degradation to fuel cell performance.[20] This finding was attributed to extensive damage to the anode microstructure observed in subsequent *ex situ* SEM experiments.

My Ph.D research was performed both at Montana State University and at the Naval Research Laboratory (Washington, DC). Experiments combined.newly adapted electrochemical methods together with near infrared thermal imaging, Fourier transform infrared emission spectroscopy, and mass spectrometry identification of products to deduce the mechanisms for S induced degradation and remediation of C induced degradation of SOFC anodes. Understanding those experimental methods will be essential to understanding the conclusions I was able to derive from those data.

Techniques/Experimental Methods

Due to the high temperatures and chemical environments required for SOFCs operation, *operando* techniques are historically difficult to employ. My Ph.D research used custom designed SOFC assemblies that permit simultaneous optical and electrochemical access to fuel cell. This dual capability will enables *operando* optical tools and electrochemical measurements to directly correlate cell performance with real time chemical changes occurring on the anode surface.

Electrochemistry

SOFCs are traditionally studied using a combination of electrochemical impedance spectroscopy, linear sweep voltammetry and chronopotentiometry.[8, 39] These techniques provide meaningful insight into cell performance and degradation. The electrochemical analysis is monitored using a potentiostat. Data presented in this dissertation were measured using a Gamry 3000 potentiostat, equipped to perform a variety of

electrochemical analysis, including both potentiostatic (constant voltage) and galvanostatic (constant current) experiments.

Electrochemical Impedance Spectroscopy (EIS) measures the impedance of a cell as a function of the frequency of an AC wave.[40] Impedance is represented as a complex number and is measured by monitoring how an oscillating electric wave changes amplitude and phase as it passes through a circuit. Changes in the wave amplitude are assigned to the real portion of impedance and are due to Ohmic resistance in the circuit. Changes in the wave phase are assigned to the imaginary portion and arise from capacitive and inductive elements in the circuit. The impedance can then be plotted either as the phase angle between the real and imaginary portions of impedance vs. the frequency (Bode plot) or as the magnitude of the imaginary portion (capacitive impedance) vs. the real portion of impedance (Ohmic impdedance) as a Nyquist plot. In order for changes in real and imaginary impedances to be interpreted in a mechanistic context, a model cell must be created, where different elements in the cell are assigned to electrochemical and mass transport processes. For SOFCs, the processes occurring at the anode, cathode and electrolyte are modeled with parallel RC circuits for each.[39, 41, 42] Capacitance is frequently assumed to be non-ideal, allowing some current to flow once the effective capacitor is charged, and is assigned the symbol *Q*, (rather than *C*). With these models, changes in the structure and functionality can therefore be monitored *in operando*. For example, Koh *et. al.* monitored C formation from CH_4 decomposition on anode supported cells at 750 °C using EIS, the plot of which can be seen in Figure 5. The arcs for H_2 are much smaller than those for CH_4, which is due to the difference between the electrochemical kinetics between

H oxidation and C oxidation. As C was deposited on the cell, the values for Z_{real} and Z_{im} increase, indicating a decrease in cell performance as more C accumulated.

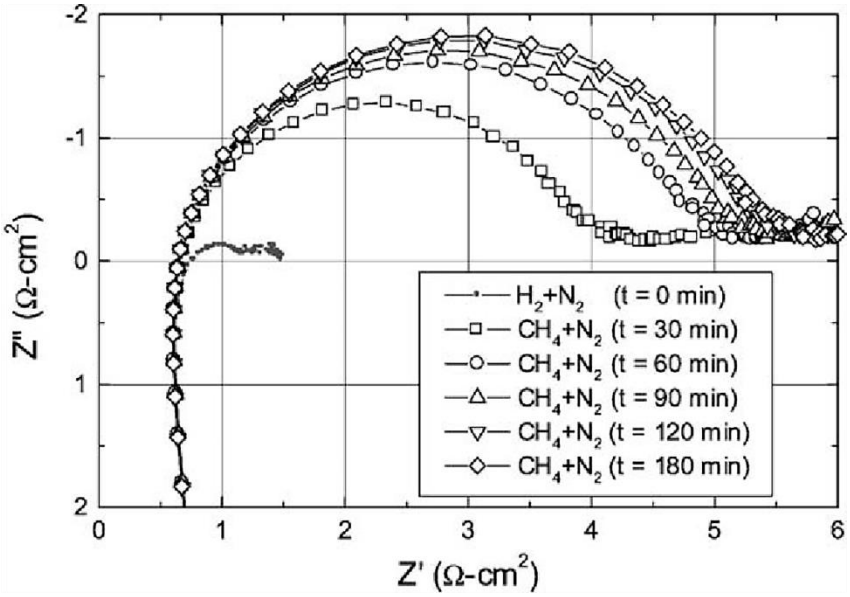

Figure 5 Temporal evolution of EIS spectra of anode supported cell operating on methane at 750 °C.[31]

While other techniques may show that cell performance returns to previous values, EIS data can be used to infer that there were structural changes that occurred to the cell during operation.[16, 43]

Linear Sweep Voltammetry (LSV) is an electrochemical technique where the current is measured as potential is increased at a constant rate.[40] This technique can provide a number of indicators about cell performance. A non-linear response at low current can indicate activation potential, while a non-linear response at higher current can indicate mass transfer limitations.[44] The slope, when in a linear regime, is indicative of the overall Ohmic cell resistance.[40] Shallower slopes are desirable figures of merit. Changes in LSV shape indicate that cell performance has changed and is useful when studying contaminants

effects on SOFCs.[43] Power can also be plotted on LSV plots, which is simply the product of voltage and current. In an article published by Zha *et. al.* LSV was used to initially characterize electrolyte cell performance at 700 °C, 800 °C, and 900 °C prior to exposure to H_2S, and can be seen in Figure 6. [45]The steeper slopes and lower power curves at lower temperature result from the increased barrier for oxide transport at lower temperatures, and is indicative of oxide transport being rate determining for these cells.

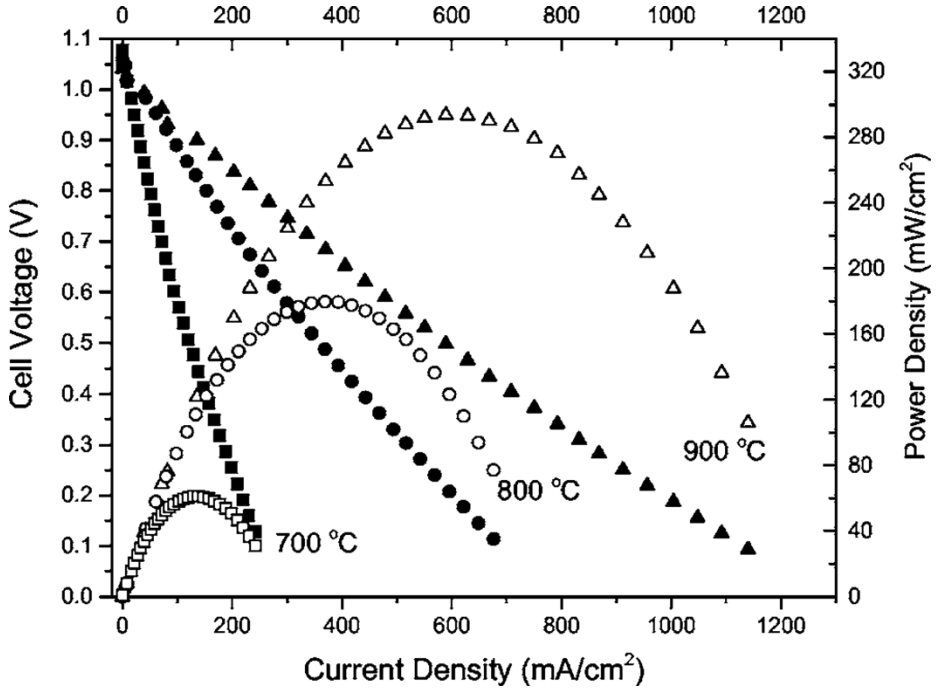

Figure 6 LSV and power curves of electrolyte supported cells at 700 °C, 800 °C, and 900 °C.[45]

Chronopotentiometry measures the potential of the cell, either at a constant current or at open circuit voltage (OCV), as a function of time. Changes in the OCV are usually the result of changes in the gas phase composition or deposition of electroactive material onto an electrode, such as C.[6, 14, 40] Changes in potential at constant current occur as a result of factors including changes in electrode microstructure, material deposition onto an

electrode, or the blocking of active sites by a fuel stream contaminant.[14, 18] Therefore, chronopotentiometry is commonly applied in characterizing the behavior of fuel stream contaminants. S, for instance, causes an immediate potential drop to a value that remains constant for many hours.[14-16] For example, in an article published by Sasaki *et. al.* chronopotentiometry was monitored at 200 mA/cm^2 on an electrolyte supported cell operating on 5 ppm H_2S in humidified H_2 at 1000 °C, seen in Figure 7.[14] Once H_2S was no longer being added to the fuel stream the potential increased as the cell required less of an overpotential to generate the requested current.

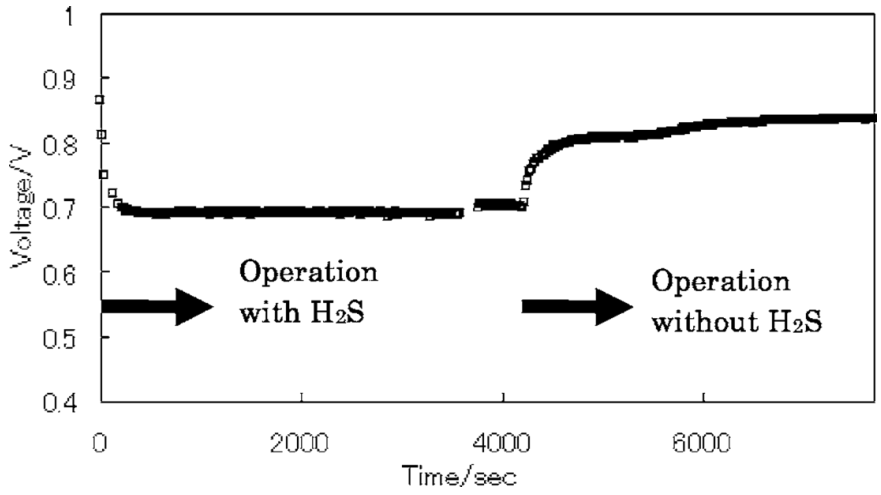

Figure 7 Chronopotentiometry of electrolyte supported cell at 1000 °C operating on humidified H_2 with 5 ppm H_2S.[14]

At higher currents, the potential drop is diminished, possibly due to the oxidation of S to form SO_2.[45] A similar technique, Chronoamperometry, provides similar information by monitoring current at a fixed potential as a function of time.[40]

These methods provide quantitative descriptions of electrode degradation that can be related, qualitatively, to changes in anode microstructure and material composition. EIS

provides the most information about the degradation mechanism, though this capability is limited in its accuracy of the test cell and requires independent validation of any mechanisms proposed to explain changes in conversion efficiency. LSV provides qualitative information about the ability of the cell to generate electrons for power, but due to the complex nature of SOFCs, current models are frequently not predictive. Chronopotentiometry is effective in measuring real-time the degradation of a fuel cell, operating either in thermodynamically controlled conditions (OCV) or under kinetically controlled conditions (constant current or potential). However, none of these techniques directly monitor changes to electrode microstructure. To accomplish this task, I adapted a traditional electrochemical technique to SOFCs chronocoulometry. Chronocoulometry (CC) was initially developed to monitor adsorbed species on an electrode with solution-based systems.[46, 47] To adapt this technique to SOFCs, a series of step potentials are used to determine the amount of excess charge at no applied over potential. With chronocoulometry data one can correlate the number of adsorbed reactants to a putative TPB length and determine how that length changes under a variety of conditions. Since CC is newly developed for SOFCs, Chapter 2 describe in more detail how this technique was adapted to SOFCs and notes potential limitations of this novel application.

Near Infrared Thermal Imaging

Near Infrared Thermal Imaging (NIRTI) monitors the intensity N-IR light between 700 and 1200 nm and correlates that intensity to temperature with independent data from attached thermocouples. Reactions that cause a change in electrode temperature or material changes that cause changes in thermal emissivity can be monitored across the entire

electrode simultaneously. Differentiating those two factors can be challenging. Generally, reversible changes to cell temperature are associated with reactions occurring on the cell, whereas irreversible changes are correlated to materials changes. NIRTI has been extremely valuable for studying SOFCs, whether monitoring chemistries occurring on the cells or the effects of thermal gradient induced stresses on SOFC materials.[21, 22, 48-57] The system employed in this work and developed at the Naval Research Laboratory uses a 14-bit, 656 by 492 pixel, CCD camera (Allied Vision Technologies, Stingray F033B ASG) and can monitor changes as small as 0.1 °C at 800 °C with a spatial resolution of 200 μm at 5 Hz.[21, 22, 48, 50, 51, 53-55, 57] Since NIRTI can image the entire cell in real time, this capability is crucial for monitoring spatially distributed materials and chemical reactivity changes.

FTIRES

The other half of the infrared duplex system at NRL takes the N-IR light and disperses the emitted light off a grating to monitor the change in infrared emissivity using an Fourier Transform Infrared Spectrometer (Mattson Instruments, Inc. Model Number: RS-10000) (FTIRES).[21, 22, 55] Since the gas phase reactants are at an elevated temperature for SOFC operation, some of those species are in an excited vibrational states. As they relax to the ground state, they emit IR light at discrete frequencies that is collected by the interferometer in the FTIR spectrometer. The resulting interferogram is deconvoluted to report the emitted light intensity at a given frequency. The gas phase components have known IR emission lines, and the intensity of those lines can be correlated to the concentration of gas phase reactants in the headspace above the cells. These results are validated independently using downstream mass spectrometry measurements. Despite the

elevated temperature, the amount of IR light emitted by the gas phase reactants is low, and long collection times are required to monitor the entire IR spectrum of interest. Therefore, the temporal resolution of FTIRES is only about 1 minute.

Mass Spectrometry

The final tool for SOFCs characterization is another method that measures the concentration of gas phase chemicals, mass spectrometry (MS). The MS instrument employed for these experiments is a Pfieffer Thermostar Quadrupole fitted with an ambient pressure inlet. The MS ionized gas phase analytes then pass through a quadrupole to filter a specific mass to charge, or M/Z, ratio. As an ion hits the detector, the current through the filament increases, so the current is therefore linearly proportional to the concentration of the ions generated. The current of the detector is monitored while the quadrupole sweeps through a variety of M/Z ratios, enabling accurate detection of a variety of gas phase reactants. By altering the partial pressure species of interests without a reaction surface for them, the current measured by the MS can be correlated to the partial pressure of a relevant reactant or product. Discrepancies between MS and FTIRES can indicate reactions occurring in the gas phase, and strong correlation between MS and FTIRES enables MS to monitor headspace partial pressures.

Synopsis and Scope of Thesis

The remainder of this dissertation is organized as follows: Chapter Two will outline the development and application of CC to SOFCs. Chapters Three and Four detail investigations into the relationship between temperature and CO/H_2S partial pressures on

TPB length and electrochemical performance using CC and NIRTI. Results from Chapter Three include the temperature dependence of TPB boundary length, how sulfur participates in electrochemical reactions, and how NIRTI in combination with CC was used to determine the synergistic effects of cell heating on electrochemical measurements, using that information to determine that H_2 oxidation follows first order reaction kinetics. Chapter Four studied how CO affects TPB length with and without H_2S. CO appears to block TPB sites, diminishing TPB length by either via non-participation in electrochemical reactions, or by inducing graphitic C formation. The addition of H_2S removes the apparent effects of CO, indicating that it prevents CO adsorption. Chapter Five shifts focus, instead using *operando* NITRI, FTIRES, MS, with simultaneous electrochemical measurements to determine the mechanisms of C removal using electrochemical oxidation, molecular oxygen, and steam. A stepwise process for C oxidation with a catalytic requirement for CO_2 production were determined, and spatially heterogenous chemistry was observed. Finally, Chapter Six explores future directions for SOFC related research, especially the use of sulfur passivated anodes for coke free hydrocarbon oxidation on SOFCs. Chapters Three and Four have already appeared in press, and there is some redundancy in the introduction and experimental section of the cells. Chapter Five has been prepared for submission to the Journal of Physical Chemistry, C

CHAPTER TWO

CHRONOCOULOMETRY

Background and Double Potential Step Chronocoulometry

Chronocoulometry was initially developed to quantitatively determine the amount of adsorbed species on an electrode.[40] This technique has been used extensively in solution-based systems to monitor adsorbed reactants, determine reactant concentration and even estimate bond strengths of reactant species. For example, Li, *et al*. used chronocoulometry to quantify chloride adsorption on a Pt 111 surface at a variety of potentials and pH's.[58] The authors found that Cl strongly chemisorbed to the platinum surface, and that chloride adsorption was strongly affected by the availability of hydronium at negative potentials, with synergistic behavior between hydrogen and chloride, and hydroxide at positive potentials, where hydroxides and chlorides compete for surface sites.[46] This analysis, and most chronocoulometric analysis focused on adsorbed reactants requires Double Potential Step Chronocoulometry (DPSCC) procedures. As the name would suggest, DPSCC is a double potential step technique that integrates the resulting current with time in order to determine the amount of charge that has passed. The initial step must be sufficiently high to drive the electrochemical system into a diffusion limited regime. The second step returns the cell to an appropriate equilibrium potential.

To determine where appropriate potentials for steps are located, cyclic voltammetry characterization is typically carried out for the system being studied. Potentials where

diffusion limited current occur are easy to locate, namely where current and potential become independent, usually indicated by a vertical line on a potential vs current plot. The potential for the second step is determined to be where the reactant of interest is neither oxidized or reduced.[40, 46, 59] When the current is determined by diffusion it is described by the Cottrell equation:

$$i(t) = \frac{nFD_0^{\frac{1}{2}}C_O^*}{\pi^{\frac{1}{2}}t^{\frac{1}{2}}} \tag{3}$$

where n is the number of electrons passed in the reaction, C_O^* is the concentration of the reactant in the bulk fluid, D_0 is the diffusion coefficient, and t is time. By integrating the current response with respect to time, one can determine the amount of charge that has been passed through the circuit, and is represented by the equation:

$$Q(t) = \frac{2nFAD_0^{\frac{1}{2}}C_O^*t^{\frac{1}{2}}}{\pi^{\frac{1}{2}}} + Q_{dl} + nFA\Gamma_O \tag{4}$$

where Q_{dl} is the double layer charging, and Γ_O is the surface excess of the oxidant species. To determine the amount of charge due to a species adsorbed to the surface, the current response can be plotted against the square root of time. If the system is truly in a diffusion limited current regime, the resultant plot will be linear and the intercept is from combined contributions from adsorbed reactants and double layer charging. The intercept should be positive. The double layer charging, charging due to the intrinsic accumulation of charged species at the electrode-electrolyte interface, can be eliminated by returning the potential to an initial potential where a reactant is neither oxidized or reduced. Current in this regime is almost entirely due to the discharge of the double layer, and again plotting charge as a

function of the square root of time allows one to determine the amount of charge from double layer capacitance, which should be negative.[40] A plot of the charge vs time$^{1/2}$ is called an Anson Plot, and a representative from the original paper is included in Figure 8. The difference between the intercepts between the Anson Plots are used to determine Q_{ads} An Anson plot from the original paper is included below.

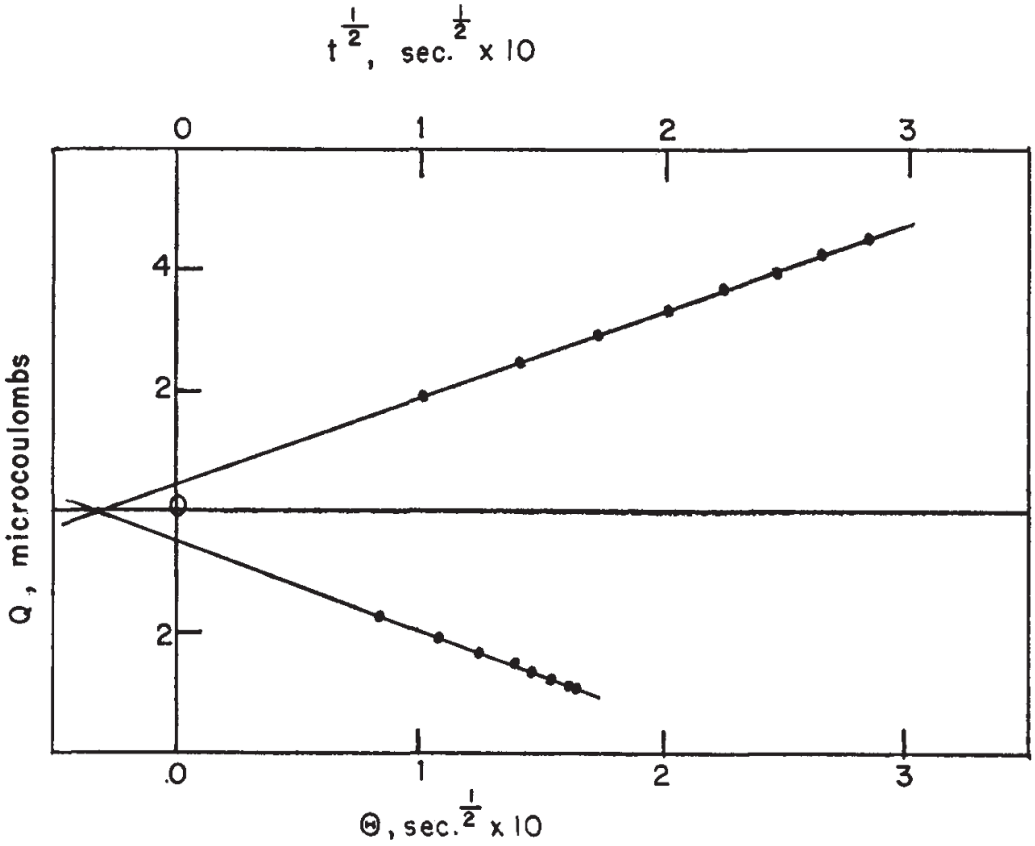

Figure 8 Anson Plot for a solution based system using a Hg drop electrode.

This technique was used to determine the quantity of $Co(en)_3^{2+}$ and $Co(en)_3^{3+}$ adsorbed on a mercury drop electrode. Mercury drop electrodes are commonly used to develop new quantitative electrochemical techniques since the liquid electrode ensures consistent, easily

determined surface area. Literature using DPSCC typically omit Anson Plots, and instead simply state rather just the conclusions derived from them.

Unfortunately, for SOFCs, the application of DPSCC is not as straight forward, as can be seen in data acquired from a functioning SOFC and shown in Figure 9. The intercept during the initial step is negative, indicating of current with some degree of charge transfer kinetics dependence. Even with very dilute H_2 and overpotentials well in excess of short circuit values, the intercepts never become positive for the initial step, and the measured DL charging is insufficient to make it positive. This result arises because overpotentials sufficiently high to force SOFC into a diffusion limited regime are also sufficiently high to oxidize the electrode. As a result, instantaneously applied potentials never appear to be capable of forcing SOFCs into a diffusion limited current at early times. Fortunately, when the current is instead determined entirely by adsorbed reactants, there is another chronocoulometric technique to determine the population of adsorbed reactants.[40, 60]

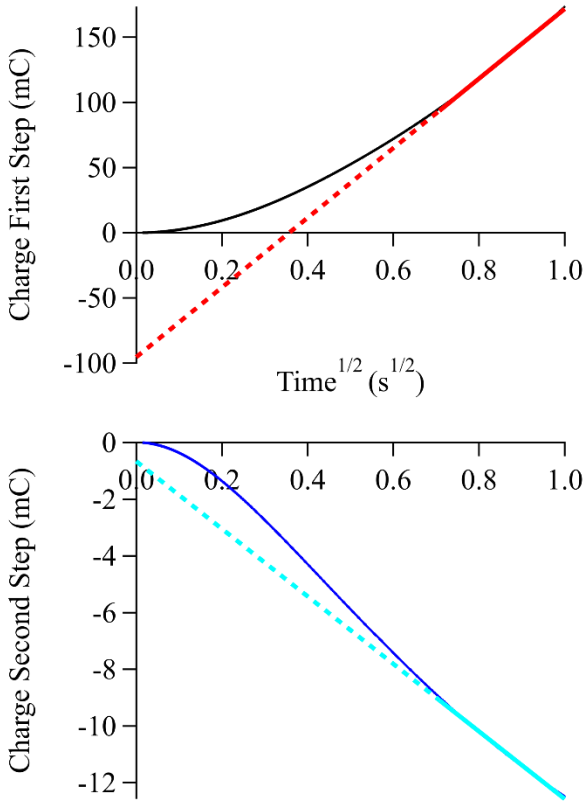

Figure 9 Anson plot for electrolyte supported SOFC in 50% H_2 at 650 °C with a 1.0 V applied overpotential using a 2-electrode geometry.

Multi-Potential Step Chronocoulometry

Multi-Potential Step Chronocoulometry (CC), was initially used to monitor the electroreduction of Bovine serum albumin (BSA) with a hanging mercury drop electrode, determining that during electroreduction a monolayer of BSA was reduced, breaking 8 or 9 of its disulfide bonds.[60] Since this technique requires many potential steps to determine adsorbed reactant concentrations, it is much less commonly used than DPSCC. To understand why this methodology works for SOFCs, one must consider the basic model for an SOFC electrode, namely, a parallel RC circuit, shown below in Figure 10.[39]

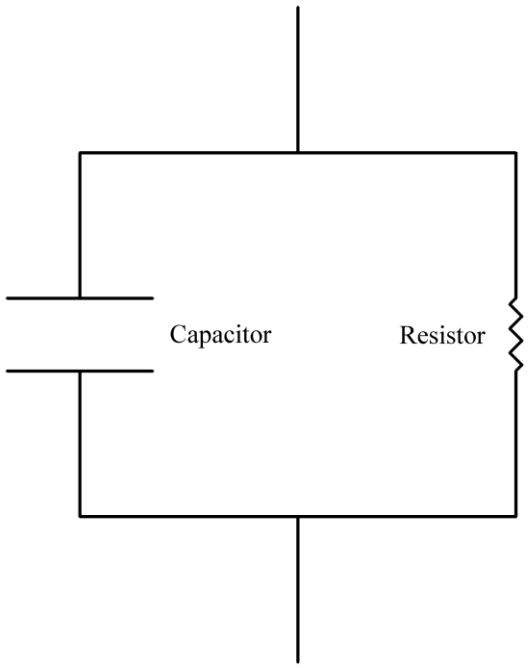

Figure 10 A model RC circuit for a single electrode

When we apply a step potential, or a near instantaneous change in potential, the current at earliest time flows rapidly onto the capacitor, the current during this time is proportional to the change in potential, until it begins building up charge. Current then begins to flow across the resistor. Once the voltage across the capacitor equals the applied overpotential, current flows entirely through the resistive elements. This description models how fuel cells eventually reach a constant current state under potentiostatic conditions, and the current at that state is determined solely by resistive elements in the cell. Measuring the integrated current during that step determines the number of electrons that have passed through the circuit in a given time. For this ideal circuit the charge is expressed by Equation 5:

$$Q(\eta, \tau) = \left(C + \frac{\tau}{R}\right)\eta \tag{5}$$

where Q is the amount of charge generated at the electrode, η is the step's applied overpotential, C is the capacitance, and R the resistance. Charge, then, is dependent on the applied potential, η, and the amount of time that has elapsed, τ. SOFCs behave similarly to this with one exception. Since an SOFC's fuel must first adsorb onto the cell prior to oxidation, SOFC anodes begin with an additional initial charge, or

$$Q(\eta, \tau) = \left(C + \frac{\tau}{R}\right)\eta + Q_{ads} \tag{6}$$

Where Q_{ads} is the charge from those initially adsorbed species. If τ is held constant, this equation is linear, so to determine Q_{ads} we can monitor charge at a series of increasing polarizations to the cell, with sufficient relaxation time between steps to ensure the cell has returned as much to equilibrium as possible, illustrated in Figure 11.

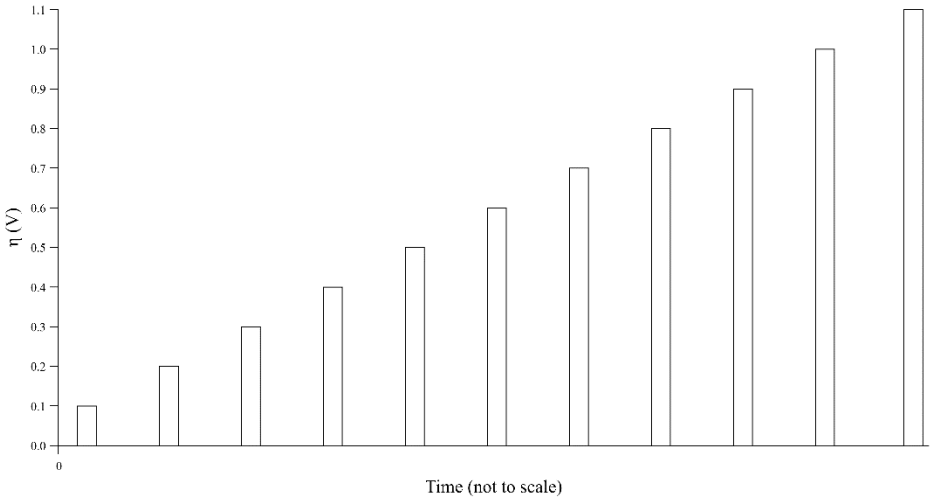

Figure 11 Plot of polarizations vs time for a chronocoulometry experiment

If total charge is plotted at a constant τ as a function of overpotential and analyzed with a linear regression, we can determine Q_{ads}. For the ideal circuit, Q_{ads} would be 0 since there should be no initial charge on the cell. For an ideal fuel cell, Q_{ads} would have a

positive value corresponding to the fuel "pre-adsorbed" onto the electrode. Q_{ads} for an actual fuel cell can be measured as negative if the fuel cell is in a two-electrode geometry, where the current and potential are being measured and altered from the same electrodes. With a two-electrode geometry, the potential being applied is diminished by resistance across the electrolyte, so the potential experienced at the electrode is less than what is being applied by a potentiostat. To improve the technique's accuracy, a reference electrode must be used during CC measurements. Representative plots of Q_{ads} vs η in two electrode and three-electrode geometries for an SOFC operating with H_2 are shown in the Figure 12.

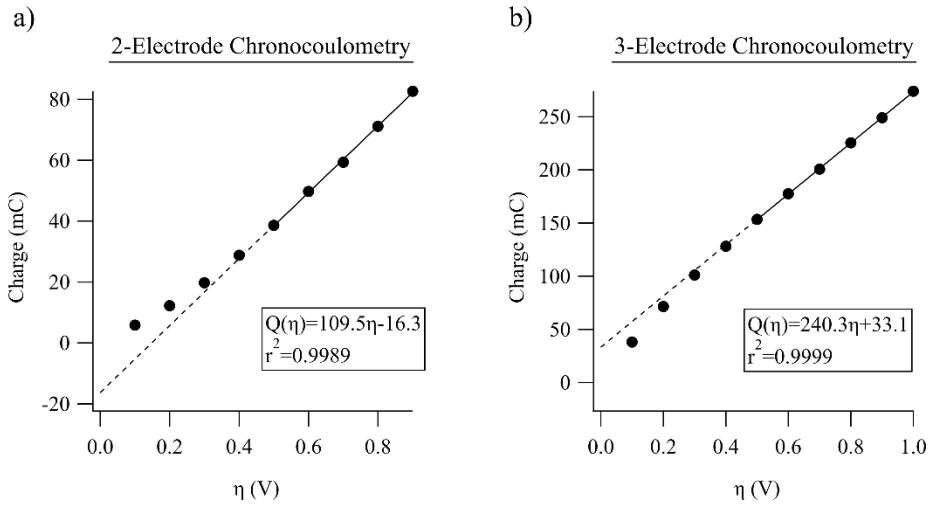

Figure 12 Representative plots of Q_{ads} vs η at τ=1 second using electrolyte supported cells at 650 °C in 50% H_2 (with Ar as the carrier gas) in a a) two electrode geometry and b) three electrode geometry.

Data in Figure 12 show values for Q_{ads} are positive only in the three-electrode geometries and both the slope and values for charge are greater in the three-electrode geometry. This result arises from the uncompensated resistance between the working and reference electrode is smaller when the reference electrode is placed as close to the working electrode (anode) as possible.

The use and placement of a reference electrode for three-electrode geometries is controversial for SOFCs.[42, 61-64] Specifically, controversies arise from induction loops and other artifacts from measurements using AC potentials. However, CC is a DC measurement, and any effects from induction during the initial polarization step are linearly dependent on potential, and would not contribute to the intercept. Additional information regarding placement and materials for a reference electrode will be discussed shortly.

CC has an important advantage over DPSCC, namely, CC can monitor time dependent data. Once Q_{ads} is measured accurately at a given τ, changes over time can be monitored by repeating this process for increasing values of τ. An ideal fuel cell would have a constant value for Q_{ads}, regardless of the value of τ. However, since this work examines real systems, the current at very early times must be limited by the potentiostat to prevent damage from extremely high current values as the capacitor charges after the near instantaneous potential step. The time required for the capacitor to charge is known as the cell time constant and is proportional to RC, or the resistance the cell experiences and its capacitance. At times before the cell time constant, the values for Q_{ads} are dependent on instrument response, and are therefore not reliable. Consequently, Q_{ads} is expected to rise to a positive constant value. During polarization, however, the fuel cell system can experience synergistic effects that can add polarization dependent concavity to the measured response and the measured value of Q_{ads} can change. If synergistic effects cause a negative concavity, or less charge than expected as a function of potential, the value of Q_{ads} will begin to rise over time. If synergistic effects cause a negative concavity, or more charge than expected as a function of potential, Q_{ads} will decrease with time. Determining

what might cause these changes in concavity can be both challenging and illuminating for processes occurring on the electrode surface. A representative Q_{ads} vs τ plot is shown below in Figure 13.

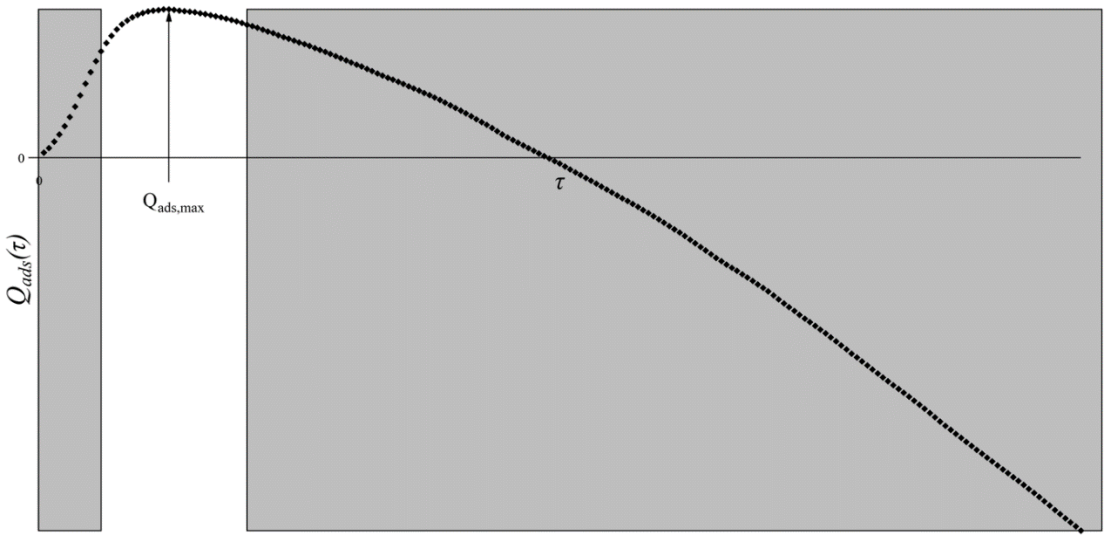

Figure 13 Plot of Q_{ads} vs τ for an electrolyte supported cell at 800 °C operating with H_2. The grey box on the left indicates times before the cell time constant, and the box on the right indicates times where synergistic effects are causing deviations from expected behavior. $Q_{ads,max}$ is indicated with the arrow.

Since the values at early times are determined by instrument response, and those at long times can be affected by synergistic effects there is a narrow window where the values measured are physically significant. Additionally, this window also corresponds to the time where the plots of Q vs η are most linear, and associated uncertainties are the smallest. The maximum value $Q_{ads,max}$, is used to determine the amount of charge from adsorbed reactants at equilibrium.

Experimental Considerations

CC is a very useful tool, since it can, given the limitations described above, monitor changes to TPB length under a variety of conditions, and can be easily incorporated into SOFC experiments. Ssome considerations for experimental design must be taken into account, however, to perform CC experiments. First, the use of a three-electrode geometry, a simplified version of which is illustrated in the Figure 14.

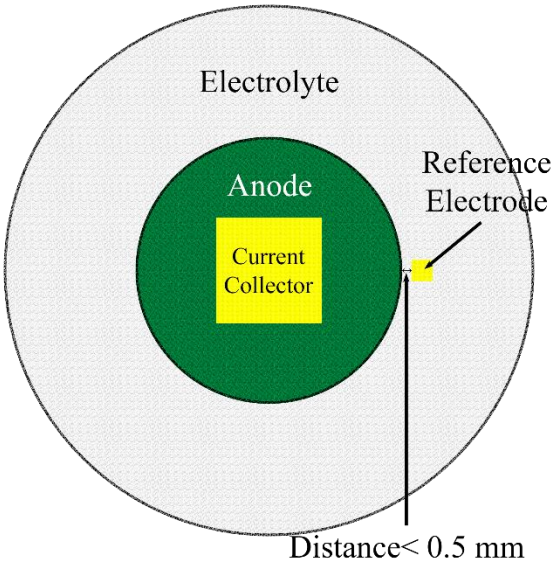

Figure 14 Illustration of SOFC with three-electrode geometry, using gold for current collector and reference electrode. The distance between the reference electrode and anode is noted as less than 0.5 mm.

As stated previously, the use of a three-electrode geometry is controversial, but essential for applying accurate overpotentials between the reference and working electrodes. Those controversies mostly arise from apparent inductance effects observed in EIS data , but any such effects would occur before the cell time constant and should not be relevant to CC measurements. Secondly, since the cell is being perturbed by the potential

steps, measuring either OCV or current during the rest period between potential steps is important to ensure that the cell has adequate time to return to an equilibrium state and changes during potential steps are minimized. While each SOFC assembly is different, repeated measurements for button cells used in this work showed that 60-90 s provided adequate relaxation time. Third, the material for the reference electrode must be chemically stable and non-catalytic. Therefore, Au is an excellent candidate, since it is chemically inert under SOFC operating conditions, and was used for all studies described in this dissertation. Fourth, the cell time constant and synergistic effects that can narrow the window when CC measurements are physically significant, must be taken into account. SOFC cells with poor performance (thick electrolytes, poor catalytic materials, inconsistent connections to leads, etc.) can increase the cell time constant. One of the synergistic effects that can occur on the cell and cause a positive concavity in Q vs η are thermal changes occurring on the cell, which will be discussed in Chapter 3. Additionally, rapid, irreversible loss of TPB sites while polarizing the cell can cause a negative concavity for Q_{ads} vs η, as was observed when polarizing a cell under Ar, without fuel present, seen in Figure 15. In this situation, Q_{ads} results entirely from electrochemical oxidation of the Ni anode itself.

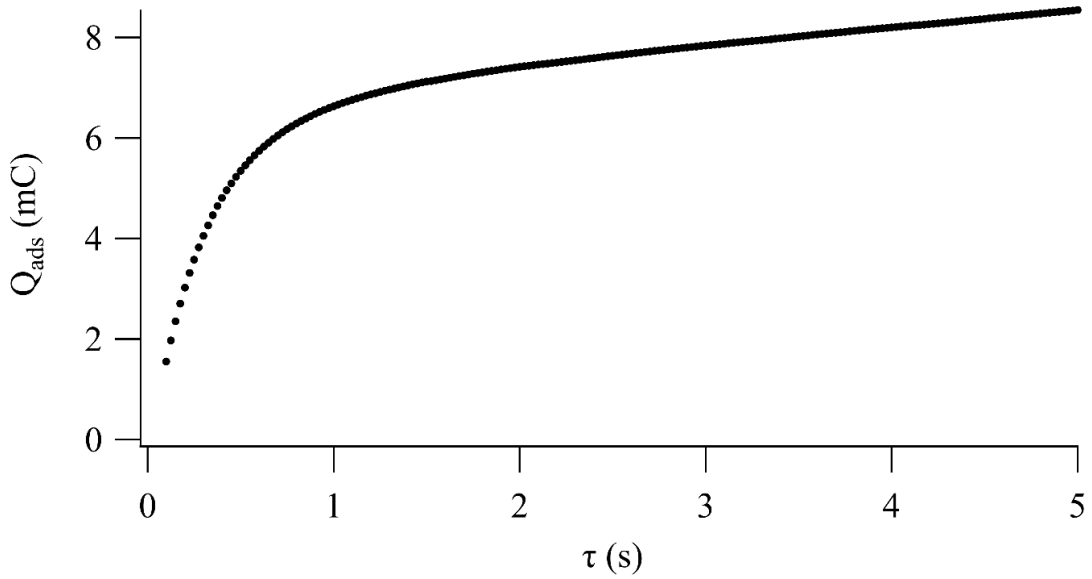

Figure 15 Q_{ads} vs τ for an electrolyte suported cell at 700 °C under pure Ar.

Between an unfavorable cell time constant and the synergistic effects from thermal and material changes that occur when the polarization step is applied, the window where CC measurements correspond to physical meaningful effects can shrink to zero. The best solution to both limiting cases is to decrease the area of the working electrode, and if possible, to an ultramicroelectrode.[40, 59] An ultamicroelectrode improves the cell time constant by decreasing the area of the cell and cell capacitance. With a sufficiently small electrode, little fuel is oxidized so thermal changes are minimized, and so long as the electrode material does not change, synergistic effects will also be minimized. A smaller electrode may also enable the differentiation of chemical reactions with different, but very rapid, kinetics. For example, Yu *et. al.* were able to use a 20 μm diameter electrode and accuratly monitor current responses from 300 μs to 500 ms for ferrocyanide/ferricyanide system adsorbed on a Pt electrode.[59] These experiments were performed using DPSCC,

and were therefore time independent. With CC time dependent data are generated. The use of an ultramicroelectrode also enables the use of patterned anodes, which have been very useful in determining SOFC surface chemistry mechanisms. While SOFC electrodes are not well-controlled, microeletrodes, this analysis suggests that future studies using model electrodes constructed from SOFC materials may prove instructive for determining elementary step rate constants in these electrocatalytic systems.[65-68]

In the subsequent chapters, CC will be used to characterize changes in triple phase boundary length for SOFCs operating at different temperatures and under different fuel conditions. CC was able to determine that TPB length was temperature dependent, increasing at increasing temperatures, and that CO diminished that TPB length. CC was also able to monitor S surface coverage and was key in determining that S participates in electrochemical reactions, rather than simply blocking TPB sites. CC also determined that S prevents CO adsorption, preventing it from decreasing TPB. CC is a powerful tool for determining SOFC behavior, and, with a few simple changes to cell wiring geometries, can easily be incorporated for SOFC characterization.

CHAPTER THREE

ELECTROCHEMICAL SULFUR OXIDATION IN SOLID OXIDE FUEL CELLS STUDIED BY NEAR INFRARED THERMAL IMAGING AND CHRONOCOULOMETRY

Contribution of Authors and Co-Authors

Manuscript in Chapter 3

Author: Elias D. Pomeroy

Contributions: Conceptualization, methodology, data collection and analysis, writing-original draft, review and editing

Co-Author: William A. Maza

Contributions: Conceptualization, methodology, data collection and analysis, writing-review and editing

Co-Author: Daniel A Steinhurst

Contributions: Data collection and analysis, writing-review and editing

Co-Author: Jeffrey C. Owrutsky

Contributions: Supervision, funding acquisition, Writing-review & editing

Co-Author: Robert A. Walker

Contributions: Supervision, funding acquisition, Writing-review & editing

Manuscript Information

Elias D. Pomeroy, William A. Maza, Daniel A. Steinhurst, Jeffrey C. Owrutsky and Robert A. Walker

Journal of the Electrochemical Society

Status of Manuscript:
____ Prepared for submission to a peer-reviewed journal
____ Officially submitted to a peer-reviewed journal
____ Accepted by a peer-reviewed journal
_x__ Published in a peer-reviewed journal

IOP Publishing Limited

Published: December 1, 2020
DOI: 10.1149/1945-7111/abcc31

ELECTROCHEMICAL SULFUR OXIDATION IN SOLID OXIDE FUEL CELLS STUDIED BY NEAR INFRARED THERMAL IMAGING AND CHRONOCOULOMETRY

Elias D. Pomeroy[a], William A. Maza[b], Daniel A. Steinhurst[c], Jeffrey C. Owrutsky[b] and Robert A. Walker[a,d]

[a]Department of Chemistry and Biochemistry, Montana State University, Bozeman, MT 59717 USA

[b]Naval Research Laboratory, Chemistry Division, Washington, DC 20375

[c]Nova Research, Inc., Alexandria, VA 22308

[d]Montana Materials Science Program, Montana State University, Bozeman, MT 59717

Abstract

A newly adapted electrochemical technique, chronocoulometry, was used to characterize sulfur's effect on the performance of porous Ni-YSZ anodes in electrolyte supported, solid oxide fuel cells (SOFCs) operating with dry H_2 at 600, 650, 700 and 800 ˚C. Chronocoulometry data together with near-infrared thermal imaging show that H_2S poisoning is more complex than sulfur simply blocking electrochemically active sites. Thermal imaging supports findings that SOFC susceptibility to sulfur poisoning depends strongly on temperature with higher performance and greater sulfur tolerance at higher temperatures. Chronocoulometry data are consistent with this description. Chronocoulometry results, however, are also more nuanced and show that sulfur adsorbed

to the triple phase boundary (TPB) can be electrochemically oxidized, thereby limiting performance loss that would result simply from blocked or inaccessible electrochemically active sites. Furthermore, chronocoulometry results imply an increased TPB length at higher operating temperatures and suggest that the spatial extent of a SOFC electrode's electrochemically active region plays a significant role in electrode surface chemistry. A simple model is developed to interpret the chronocoulometry results and determine the relative amount of sulfur adsorbed to the anode's active triple phase boundary.

Introduction.

Solid oxide fuel cell (SOFC) tolerance to fuel stream contaminants, especially chlorine and sulfur, have been extensively studied in the community with the goal of determining the mechanisms by which they degrade fuel cell performance. Chlorine, for example, can be found in reformed coal gas, especially US bituminous coal, and biogas, with reported partial pressures from 10 to 500 ppm[69, 70] Cell performance degrades rapidly when in the presence of chlorine at partial pressures as low as 20 ppm, and the degradation is concentration dependent up to 100 ppm of chlorine, after which it exhibits a saturation effect.[69, 71] Interestingly, small amounts of H_2 in SOFC fuel streams have been shown to preserve anode performance when operating with carbon-containing fuels in the presence of chorine.[43, 55, 72, 73] Chlorine degradation has been attributed to two distinct mechanisms – reversible physisorption and irreversible chemisorption – although the relative importance of each mechanism remains controversial.[71, 74]

Similarly, sulfur has long been identified as being deleterious for SOFC operation. As a contaminant frequently found in natural gas, *syn*-gas and biogas, sulfur species are believed to occupy active sites thereby limiting the amount of fuel that can be electrochemically oxidized. In addition, sulfur can react with anode materials leading to reduced electrocatalytic activity and reduced charge transport capability.[75] Most studies of sulfur-induced anode degradation have focused on Ni-containing anodes,[45, 76-79] although attention has turned recently to developing new anode materials with improved sulfur tolerance, including Cu based electrodes, mixed conducting electrodes, and composite metal sulfide electrodes.[19, 80-83] Community consensus is that if SOFCs are to become a viable contributor to large-scale energy conversion strategies that include carbon containing fuels, these devices will need improved resilience to contaminants including sulfur and chlorine that lead to long term electrode degradation and eventual device failure.[19, 76] Developing this resilience, in turn, requires knowing how and under what conditions sulfur compromises electrode stability and performance.

Sulfur-induced degradation depends on the contaminant's concentration in incident fuel feeds. When exposed to small amounts of sulfur – typically ≤ 10 ppm H_2S – Ni-YSZ anodes suffer rapid initial performance loss followed by a longer, slow degradation.[75, 77, 84] Removal of H_2S leads to partial recovery. The extent of anode degradation is also current density dependent with little or no long-term degradation being observed in SOFCs operating with small current densities and H_2S tainted fuels.[14, 16, 85] Higher current densities lead to irreversible performance degradation and loss of the percolated Ni network where damage extends for microns beyond the electrode-electrolyte boundary.

Sulfur's effects on Ni-YSZ anodes also depend on operating temperature. At higher operating temperatures (≥ 800˚C) sulfur-induced degradation is much less pronounced and sulfur's long term effects on performance are largely reversible.[14, 15] This result has been attributed to sulfur's intrinsic volatility. At lower operating temperatures (≤ 700˚C) as sulfur chemisorption becomes increasingly favored over desorption, degradation is more likely to be irreversible. Supporting these experimental findings have been a series of thermodynamic[77, 86] and *ab initio* calculations[87] that considered reaction pathways for nickel-sulfide formation through sulfur chemisorption followed by structural rearrangements that adopt different Ni_xS_y polymorphs.

Higher sulfur concentrations (≥ 100 ppm) result in more extensive nickel sulfide formation and changes in anode microstructure that result in reduced electrode surface area and charge transport capabilities.[88, 89] *Post mortem* Raman experiments identified Ni_3S_2 as a product formed on Ni-YSZ anodes exposed to 100 ppm H_2S for 5 days[90] while *in situ* Raman data reported that Ni_3S_2 underwent a structural transition near 565˚C.[91] Subsequent Raman experiments confirmed the formation of Ni_2S_3 formation at lower temperatures and complementary optical microscopy studies continued to track the formation of nickel sulfides at temperatures up to 715˚C.[92] At higher temperatures, nickel sulfide crystals disappeared and the authors proposed this observation could be explained by Ni_3S_2 melting and filling microstructure pores.

Mechanisms describing sulfur-induced degradation in SOFCs frequently rely upon results from electrochemical measurements made as a function of H_2S pressure (pH_2S), device operating temperature and/or applied potential. Electrochemical data are often

accompanied with extensive *post mortem* analyses where changes in anode microstructure and composition are compared with results from unused anodes and/or anodes that have been operated in the absence of sulfur.[80] While insightful and instructive, findings from these reports are necessarily limited. Traditional electrochemical measurements utilized for SOFCs tend to consider only relative changes in performance and not quantitative measures of chemical reaction rates nor how these rates change with pH_2S and temperature. *Postmortem* analyses assume changes that occurred during operation are preserved during cooldown and disassembly. Findings presented in work described below use results from near infrared (NIR) thermal imaging and chronocoulometry - a traditional electrochemical method for estimating numbers of active sites on an electrode - to clarify how sulfur affects the electrochemical activity of Ni-YSZ anodes operating with dry hydrogen between 600 to 800˚C. Results show that adsorbed sulfur should not be regarded simply as an adsorbate that blocks an anode's actives sites along the triple phase boundary (TPB), but rather as a species that can also be electrochemically oxidized. Furthermore, chronocoulometry data also suggest that the TPB's spatial extent throughout the anode depends on temperature in ways that can be quantified and interpreted based on oxide diffusion kinetics through the anode cermet microstructure.

Experimental.

Cell Preparation and Assembly

Experiments were performed with 25 mm diameter electrolyte-supported Hionic™ cells purchased from Fuel Cell Materials. Each button cell is comprised of a 130-170 μm thick scandium stabilized zirconium electrolyte, a ~50 μm thick 30 weight % NiO-yittria

stabilized zirconia (Ni-YSZ) anode and a ~50 μm thick lanthanum strontium doped manganate (LSM) cathode. Each electrode contained a gadolinium doped ceria (GDC) active layer between the electrode and electrolyte. A gold wire attached to a 100 mm^2 gold mesh was attached to the anode with gold paste and used as the current collector. An additional gold wire was attached to the electrolyte with a gold paste deposit located at least 0.5 mm away from the anode that served as a reference electrode. A gold wire was similarly attached to a 100 mm^2 platinum mesh attached to the cathode with platinum paste. Cells were then pasted to a 25 mm diameter alumina tube using alumina paste. This assembly was encased in a 50 mm alumina tube, together with two 6.4 mm OD alumina tubes used as gas inlet and outlet ports, and capped on one end with a 38 mm sapphire polished IR optical window allowing optical access to the anode surface. The assembly was then placed in a tube furnace together with an additional thermocouple for calibration of the thermal imaging data and heated to operational temperatures overnight at a ramp rate of 1 °C/min. Additional details about the assembly have been reported elsewhere[57, 93]

Electrochemical Impedance Spectroscopy

Electrochemical experiments were performed using a Gamry Reference 3000 potentiostat and a 2-electrode geometry for linear sweep voltammetry (LSV), electrochemical impedance spectroscopy (EIS), and open circuit potential (OCV) characterization. A 3-electrode geometry was used for chronocoulometry studies. Cell performance was characterized using EIS with a frequency range of 50,000 to 0.1 Hz at OCV. Results for EIS shown in Figure 16 illustrate how resistance increased with increasing H_2S concentrations and lower temperatures. These data are included here to

illustrate the general impedance behavior of the devices used in these studies. Additional analysis of EIS results appears in the results section in the context of correlating impedance behavior with findings from chronocoulometry experiments.

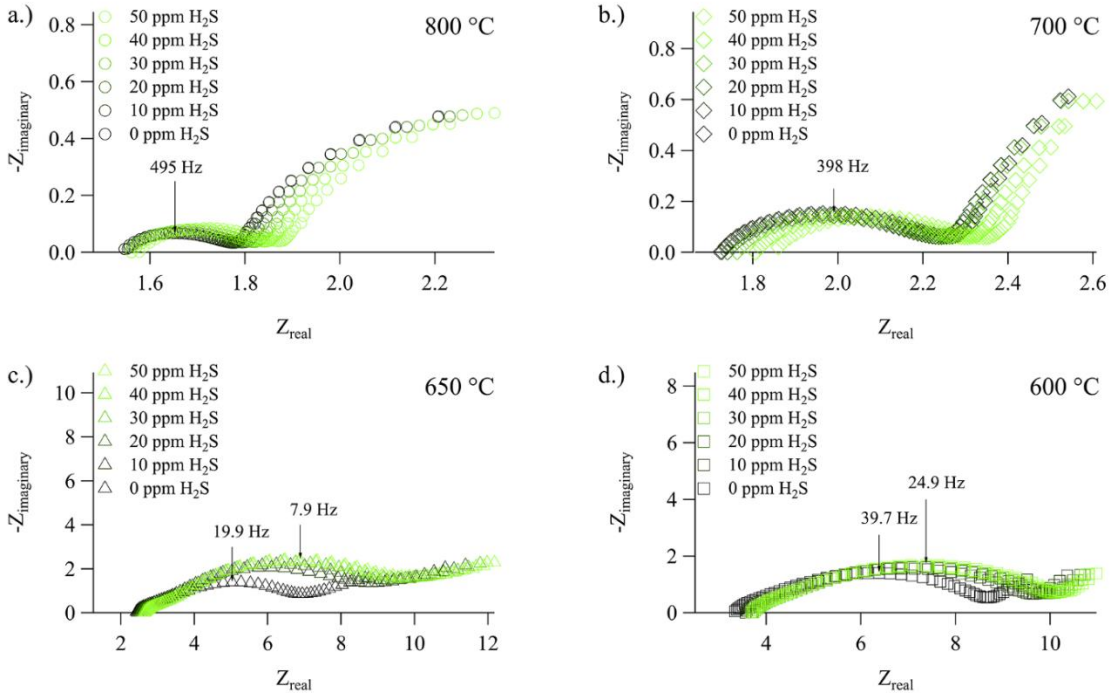

Figure 16 EIS data at a.) 800 °C, b.) 700°C, c.) 650 °C and d.) 600 °C. Each EIS trace was taken after chronocoulometry experiments, prior to changing H_2S concentration.

Near Infrared Thermal Imaging (NIRTI)

Thermal images were acquired with a ~ 5 Hz collection rate using a 14-bit, 656 by 492 pixel, CCD camera (Allied Vision Technologies, Stingray F033B ASG) with a telephoto lens (Navitar, Zoom 7000) using collection software written in-house in LabView v8.5. A long-pass filter (Hoya R72) with a nominal cutoff wavelength of 720 nm was used to block visible light from the anode and surrounding surfaces. Details, including temperature and spatial resolutions for this system, have been reported elsewhere.[21, 22, 50] The intensity was averaged over a region of interest (ROI), as indicated in the thermal

image shown in Figure 17. Data presented in this work report results from the ROI exhibiting the greatest changes in temperature during an applied chronocoulometry overpotential. These ROI were selected for analysis, and temperature changes over those pixels were averaged to produce data reported below. Intensities measured by the CCD were converted to temperature by calibration to a thermocouple located within the furnace, external to the cell. Temperature changes are measured in the ROI with 0.2˚C precision, a spatial resolution of ≤ 100 µm and a time response of ~ 0.2 seconds.

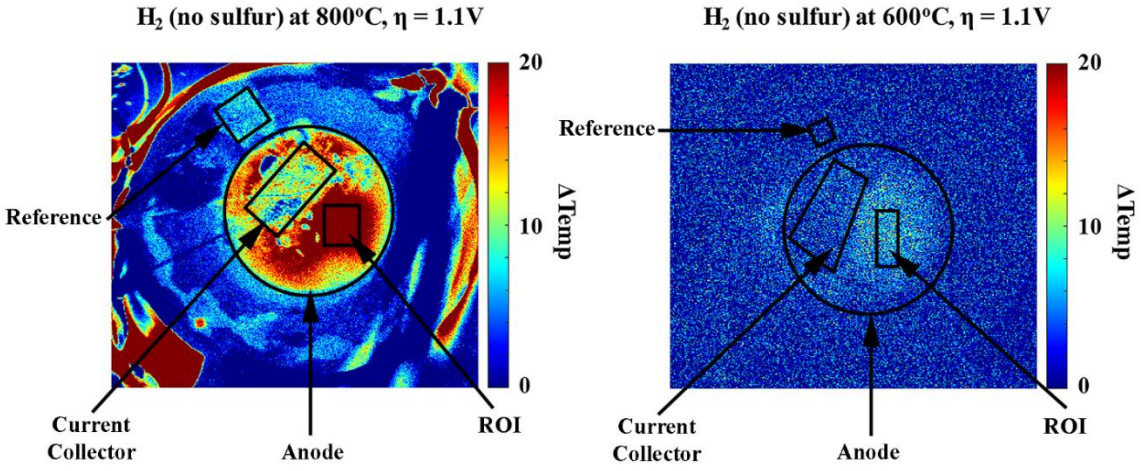

Figure 17 Thermal imaging for SOFCs polarized to 1.1 V without H_2S at a.) 800 °C and b.) 600 C. Relevant portions of the electrode assembly have been highlighted.

Chronocoulometry

Chronocoulometry uses a series of stepped polarizations (Figure 18a) to measure the charge generated from reactants adsorbed at an electrode interface. Since accurate polarization is required for these experiments, minimizing resistances between the reference and working electrode assumes critical importance. Limiting uncompensated resistance is best accomplished by placing the reference electrode as close to the working

electrode as is practical. In a more traditional, liquid electrolyte based system, this task simply requires placing the reference electrode close to the working electrode in the electrolyte solution. In SOFCs, the placement of the reference electrode is complicated by the fact that the electrolyte is a solid, and numerous reports have considered optimal reference electrode placement in order to make accurate impedance measurements.[61, 62, 64] However, since chronocoulometry measurements use constant, stepped potentials, any induction effects are lost in the large capacitive discharge that occurs prior to the cell time constant being reached. Reference electrodes in experiments described below were placed ~0.5 mm away from the anode following the work of Rutman *et al*.[61] In this geometry, care must be taken not to short the reference electrode to the working electrode. Additionally, since both 2 and 3-electrode geometries were used during these experiments, experiments where polarization occurred in a 2-electrode geometry will refer to the potential vs. Cathode (cat.) and experiments in a 3-electrode geometry will refer to potential vs. Reference (ref.).

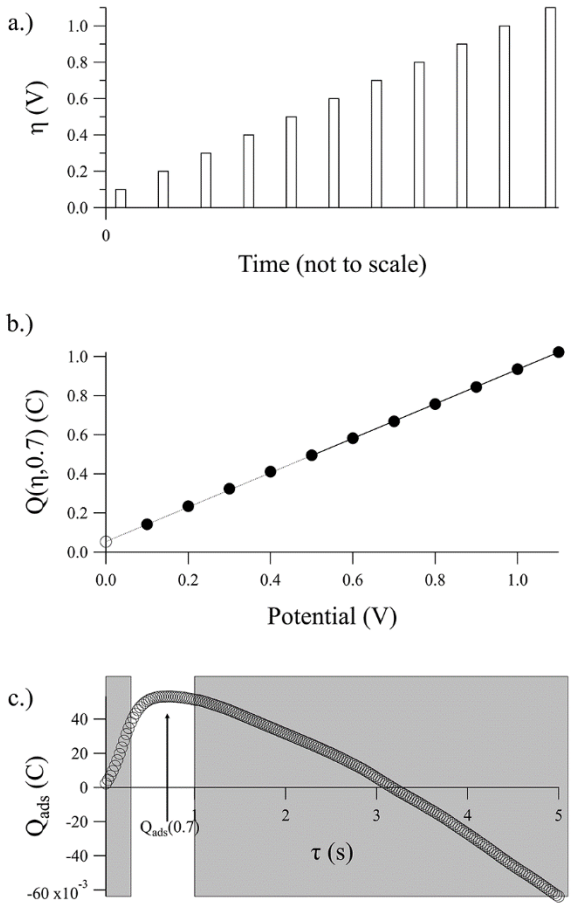

Figure 18 Schematic diagrams illustrating the procedure and representative data from a chronocoulometry experiment with a.) polarization as a function of time b.) measured charge as a function of polarization at 0.7 seconds, with the intercept highlighted by the open circle, and c.) $Q_{ads}(\tau)$ with the intercept in b.) pointed at by the arrow.

A chronocoulometry experiment is comprised of a series of increasing potential steps versus time as shown in the plot in Figure 18a. The experiment begins with a fixed-duration polarization step with the current being sampled every 100 μs. The sampling rate is chosen to balance the desire for high-resolution data with data file size. After the polarization step, the fuel cell is returned to OCV (vs. ref.). During this time, the incident H_2 re-reduces any NiO that formed when the potential step was applied. The interval at

OCV also allows any products formed from electrochemical oxidation to desorb and diffuse away from the region within and above the working electrode. To determine the interval required between potential steps, we monitored OCV until it returned to a steady state value. In principle, OCV (vs. ref.) should be 0.0 V. However, gas concentrations may be heterogeneous throughout the chamber, and slight changes in local partial pressures between the reference electrode and working electrode will cause non-zero values for OCV (vs. ref.). Typically, the OCV (vs. ref.) measured in these chronocoulometry experiments was ≤ 0.01 V. Once OCV (vs ref.) stabilized, the next polarization step was applied at a slightly higher potential. This process was repeated until the polarization was roughly equal to the OCV (vs. cat.). To assess uncertainties and allow meaningful statistical analyses of data from these measurements, three or more equivalent experiments were carried out for a given gas phase composition. Following three or more reproducible experiments with a given gas phase composition, the gas phase composition was changed and a new set of chronocoulometry experiments were performed.

In a typical chronocoulometry experiment the cell was polarized for 5s increasing in 0.1 V increments in the range between 0.1 V and 1.1 V (vs. ref.). After each polarization step, the cell was allowed to equilibrate at OCV (vs ref) for one minute. The measured currents were sampled at 10 kHz, and integrated with respect to time in order to determine the amount of charge, $Q(\eta,t)$, that was generated as a function applied overpotential (η) and time (t). Each chronocoulometry experiment was repeated twice for a total of three independent data sets at a given temperature and pH_2S. A detailed description of how chronocoulometry data were analyzed and interpreted is provided in the Results section.

Gas flows were held at a constant total gas flow of 200 sccm, 100 sccm of which was H_2, an appropriate flow of 200 ppm H_2S in Ar to reach the desired H_2S partial pressure with the balance being Ar. Partial pressures of H_2S were increased in 10 ppm increments and held at that partial pressure for roughly 30 minutes. Prior to altering the H_2S partial pressure EIS and LSV were performed to monitor cell degradation. Cathode gas flows were held constant, with 20% O_2 in Ar at 100 sccm total gas flow.

Control experiments performed with an inert gas atmosphere (with and without H_2S) followed similar procedures but with several notable differences. First, a series of benchmark experiments were performed identical to those described above (with H_2 as a fuel and no sulfur present) to confirm that the SOFC was functioning as intended. After the final OCV step in the final benchmark experiment, the fuel flow was decreased to 0 sccm, and the Ar carrier gas flow was increased to maintain constant gas flow over the anode. The OCV was monitored, and 10 minutes after the gas phase concentration was changed a polarization step was applied. In this instance, the only charge that could be generated resulted from Ni oxidation. The ten minute interval was chosen to ensure that no residual H_2 remained in fuel lines or in the chamber above the anode. After the polarization step, H_2 was reintroduced to the incident gas flow to re-reduce any Ni that had been oxidized. After the cell was reduced for 10 minutes, H_2 was again turned off for 10 minutes and a polarization step at a higher potential (vs. ref.) was applied. This process was repeated until the cell polarization reached 0.7 V approximately matching OCV (vs. cat.) without fuel.

These control experiments employed a Princeton Applied Research Versastat 3 potentiostat for all electrochemical measurements. EIS and LSV characterizations were

performed in between chronocoulometry experiments to ensure that the SOFC continued to behave consistently. Chronocoulometry experiments used polarizations from 0.07 V to 0.7 V in 0.07 V increments. Total gas flow rates were also maintained at 200 sccm. The cells were initially reduced and benchmarked by EIS and chronocoulometry performed with 100 sccm H_2 (in Ar). For the control chronocoulometry experiments H_2 was removed, and Ar flow was increased to maintain gas flow balance. The cell was then polarized, and after polarization 100 sccm of H_2 was reintroduced, and Ar flow was decreased to 100 sccm for 10 minutes. This process was repeated for each polarization step, and each chronocoulometry experiment was repeated twice for a total of three replicates. Sulfur control experiments repeated the same process, except during the third repetition, 30 ppm of H_2S was added during the Ar only step. This sulfur was removed when the H_2 was added.

Analysis of Chronocoulometry Data.

Since the data can be analyzed in different ways, a more detailed discussion about how the data are processed follows. The amount of charge produced in a chronocoulometry experiment is a function of both overpotential, η, and integration time τ, or $Q(\eta, \tau)$, described by

$$Q(\eta, \tau) = \left(C + \frac{\tau}{R}\right)\eta + Q_{ads}(0V, \tau) \quad (7)$$

where C is the capacitance of the electrode, R is the resistance of the electrode, and $Q_{ads}(0V,t)$ is the amount of charge that can be generated from species adsorbed to the anode TPB at 0V applied overpotential for a fixed integration time. In the limit that $Q_{ads}(0V,t)$ results from Faradaic processes, this quantity can be expressed as $nFA\Gamma_F$ where n are the number of electrons transferred, F is Faraday's constant, A is the TPB area and Γ_F is the

surface coverage of adsorbed fuel species in the TPB region. In the limit that the TPB is ideal, the dimensionality of A and Γ_F would reduce to a length and a 1-dimensional coverage.

Once the values for charge at each overpotential are obtained, those values at a given integration time (τ') are plotted vs η as shown in Figure 18b. Typically, linear regressions were performed in 25 ms increments to determine $Q_{ads}(\tau)$ at a fixed overpotential. Due to an electrochemical activation potential, an effect that became noticeable at lower operating temperatures, charge generated at $\eta < 0.5$ V were omitted from the linear regression. Neverthless, these data were reviewed to characterize thermal behavior at lower applied potentials. The intercept of each linear regression, $Q_{ads}(0V, \tau')$, and the associated uncertainty was recorded. Linear regressions were then repeated, with subsequent regressions using a higher value for τ, until τ' is equal to the full polarization duration (Figure 18c). Since each chronocoulometry experiment was run in triplicate, the values for $Q_{ads}(0V,\tau)$ were averaged and their uncertainties propagated. For an ideal experiment, the value of $Q_{ads}(0V,\tau)$ would be a constant for the duration of the experiment, reflecting a constant number of electrochemically active sites.

SOFCs are complex devices, however, with different phenomena that can affect chronocoulometric behavior. Whenever a process such as capacitive discharge or anode material oxidation causes changes in the curvature of the $Q(\eta,\tau)$, the value for $Q_{ads}(0V, \tau)$ can change. Since these processes cause changes in the curvature of the data, their effects are apparent in observed non-ideal chronoamperometry behavior. For an ideal RC circuit with the elements in parallel, the current at early time is dominated by capacitive charging

that decays exponentially to a constant. In principle, the amount of current generated from an ideal RC circuit would have limiting behavior approaching infinite current produced at early times. However, measurements prior to the full discharge of the cell tend to be dominated by instrument response. This behavior manifests as a rising value of $Q_{ads}(0V,\tau)$ at short times. (See the shaded box at early times in Figure 18c.) At longer times the fuel cell's response to polarization approaches ideal behavior in the limit that only Faradaic processes contribute to the measured current. However, polarization dependent deviations from ideal current behavior cause $Q_{ads}(0V,\tau)$ to change with time, and this deviation can cause unexpected changes in $Q_{ads}(0V,\tau)$. For example, if the current produced by the cell increases with time with $\frac{di}{dt}(\eta) = \frac{d^2Q}{dt^2} > 0$, the value for $Q_{ads}(\tau')$ takes on increasingly negative values as the slope of the line in Figure 18b increases. (See the shaded box at later times in Figure 18c.) Alternatively, if a process causes the cell resistance to slowly increase with time, thereby decreasing the amount of current, the value of $Q_{ads}(\tau')$ will gradually increase as the slope of the line in Figure 18b decreases.

Results.

This work focuses on experiments that measured two observables: temperature and current. Thermal imaging mapped temperature changes while chronocoulometry tracked the current response accompanying periodically applied, stepped overpotentials. Together, these two techniques led to a cohesive and internally consistent picture of how S affects the early-stage electrochemical performance of Ni-YSZ anodes as a function of H_2S concentration and operating temperature. For clarity, the following sections present first

the thermal imaging data and then the chronocoulometry data. In a separate section, results from both experiments are linked together through an Arrhenius analysis to show how adsorbed sulfur is electrochemically oxidized following adsorption to the Ni-YSZ anode and how this behavior changes with H_2S partial pressure and temperature.

Near Infrared Thermal Imaging.

NIRTI analyses of thermal changes across SOFC electrodes is a proven technique for characterizing reactivity where the near IR emission changes depend on the exo/endothermicity of relevant surface reactions.[20-22, 48, 50, 51, 57, 73, 93] Changes in temperature (ΔT) are the measured difference between the intensity of NIR light when the cell is at 0 V and when the cell is polarized. Two trends are evident in the NIRTI data shown in Figures 19a – 19e: 1) ΔT depends on the operating temperature in the absence of H_2S (Figure 19a); and 2) the way ΔT depends on the presence H_2S varies with operating temperature (Figures 19b-19e). H_2 oxidation is exothermic with positive temperature changes ($\Delta T \geq 0$) that increase with applied overpotentials (η) (Figure 19a). At 600˚C, no change in temperature occurs when $\eta = 0.1$ V (vs. ref.). At 800˚C, ΔT is +4 °C for $\eta = 0.1$ V. These values increase to ΔT = +6˚C and +19˚C at 600˚C and 800˚C, respectively, for an applied overpotential of $\eta = 1.1$ V.

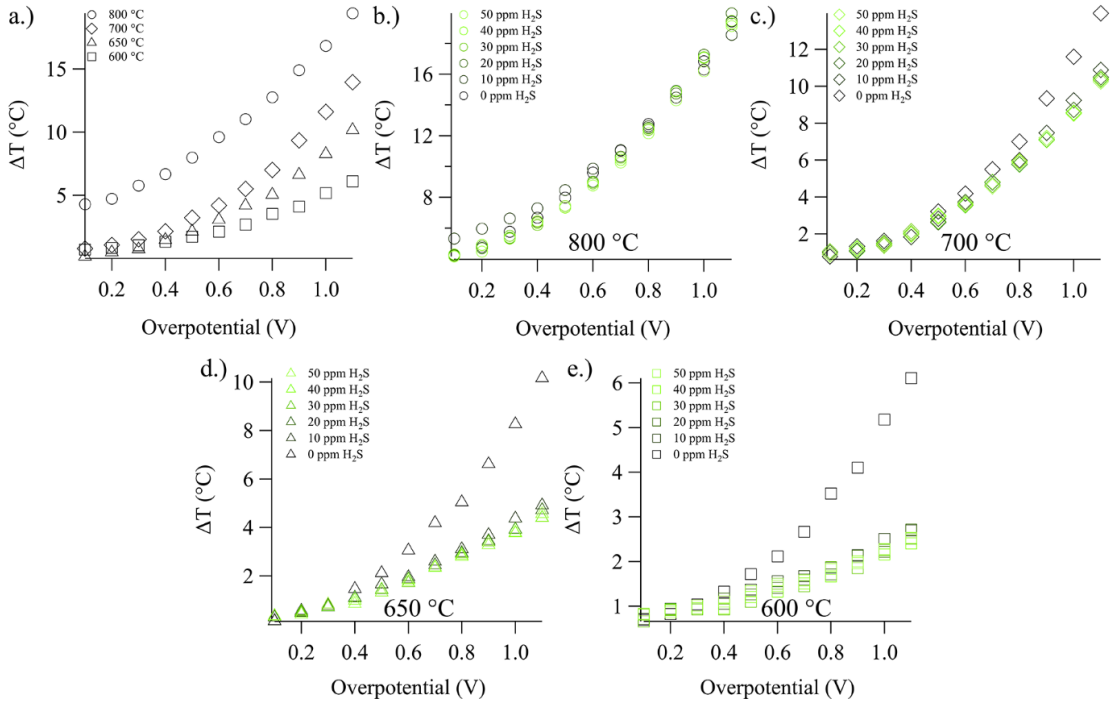

Figure 19 Results for thermal imaging with different temperatures a.) in the absence of H_2S, and in the presence of 0-50 ppm H_2S at b.) 800 °C, c.) 700 °C, d.) 650 °C, and e.) 600 °C.

The presence of sulfur affects this behavior as is evident in Figures 19b-19e. Figure 19b shows that at lower temperatures (600˚C), the addition of sulfur to the incident fuel suppresses the ΔT as a function of applied overpotential, such that with η = 1.1 V, ΔT drops by more than factor of 2 (from +6.0˚C to +2.4˚C). This effect becomes less pronounced at higher temperatures. On average, ΔT at η = 1.1 V decreased by 58%, 55%, 25%, and 1% at 600 °C, 650 °C, 700 °C, and 800 °C, respectively when sulfur was present. The absolute temperature change was between 4-6 °C, though changes in the heat capacities of the materials, gases, and other small variations from experiment to experiment make analysis of the absolute temperature changes at different temperatures difficult. A point to note is that at a given operating temperature, ΔT was much less sensitive to the *amount* of sulfur

in the incident fuel feed for pH_2S between 10-50 ppm. This observation is consistent with reports that note a sulfur saturation effect for $pH_2S \geq 5$ppm.[14]

Chronocoulometry

Chronocoulometry has been newly adapted to SOFCs, and the work herein suggests that the technique is a promising means to assess contaminant induced degradation mechanisms. Figure 20a shows typical chronocoulometric behavior for an anode operating with uncontaminated H_2. Each time-point in Figure 20a represents the $\eta = 0$ V intercept of a chronocoulometry plot ($Q(0V,\tau)$) obtained as shown schematically in Figure 18b. As noted above, in the limit of ideal behavior, if $Q_{ads,max}$ is related to the number of electrochemically active sites on the anode, these plots should be flat as a function of time. $Q_{ads,max}$ may change depending on the extent of an anode's electrochemically active region, a quantity that will depend on temperature and associated oxide mobility through the YSZ porous network. This issue will be addressed in the Discussion section.

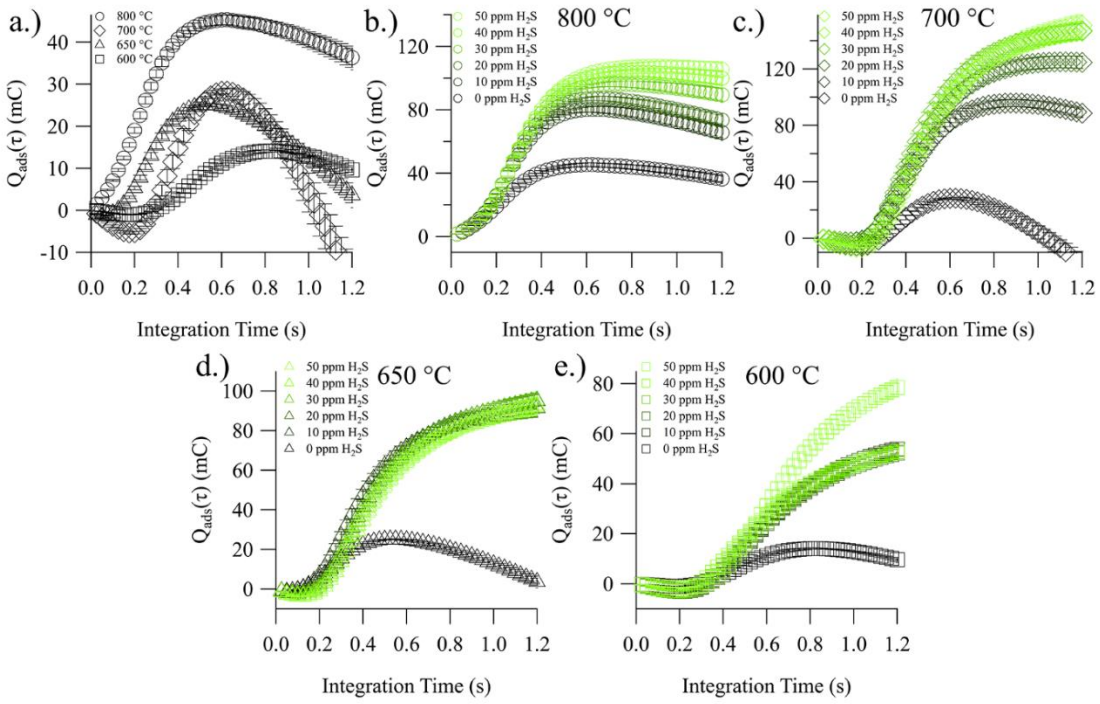

Figure 20 Adsorbed charge (Q(0V, t') for different chronocoulometry experiments at different temperatures and as a function of pH_2S. a.) in the absence of H_2S, and in the presence of 0-50 ppm H_2S at b.) 800 °C, c.) 700 °C, d.) 650 °C, and e.) 600 °C.

The data in 5a are clearly not flat. The data also show distinctive temperature dependences. The rise in Q_{ads} at early τ is excluded from the analysis, since the charge generated during this time originates from the capacitive discharge of the electrode in response to the step potential and is mostly due to instrument response.[40] At long times, additional charge is generated via steady-state faradaic current, and the statistical uncertainty in the intercept increases as well, as can be seen by the magnitude of the error bars in Figure 20. Additionally, as will be discussed below, thermally-dependent chemical processes will affect the current resulting in a diminished $Q_{ads}(0V,\tau)$ complicating interpretation. These competing processes leave a narrow time window when the values of

$Q_{ads}(0V,\tau)$ can be assigned to interpretable SOFC physical properties. The peak value for $Q_{ads}(0V,\tau)$, $Q_{ads,max}$, corresponds to that region of the measured data having the best linear correlation between charge generated in a chronocoulometry experiment and the applied overpotential, strongly supporting the validity of the description of electrode processes provided above. Additionally, if we assume that each charge transfer event occurs at individual active sites, then this value is directly related to the number of TPB active sites. This treatment differs slightly from an earlier report where the value of τ when $Q_{ads}(\tau)$ was greatest without H_2S was then used to determine $Q_{ads,max}$ in the presence of H_2S.[94] The values for $Q_{ads,max}$ can be seen in Figure 21 and Table 1.

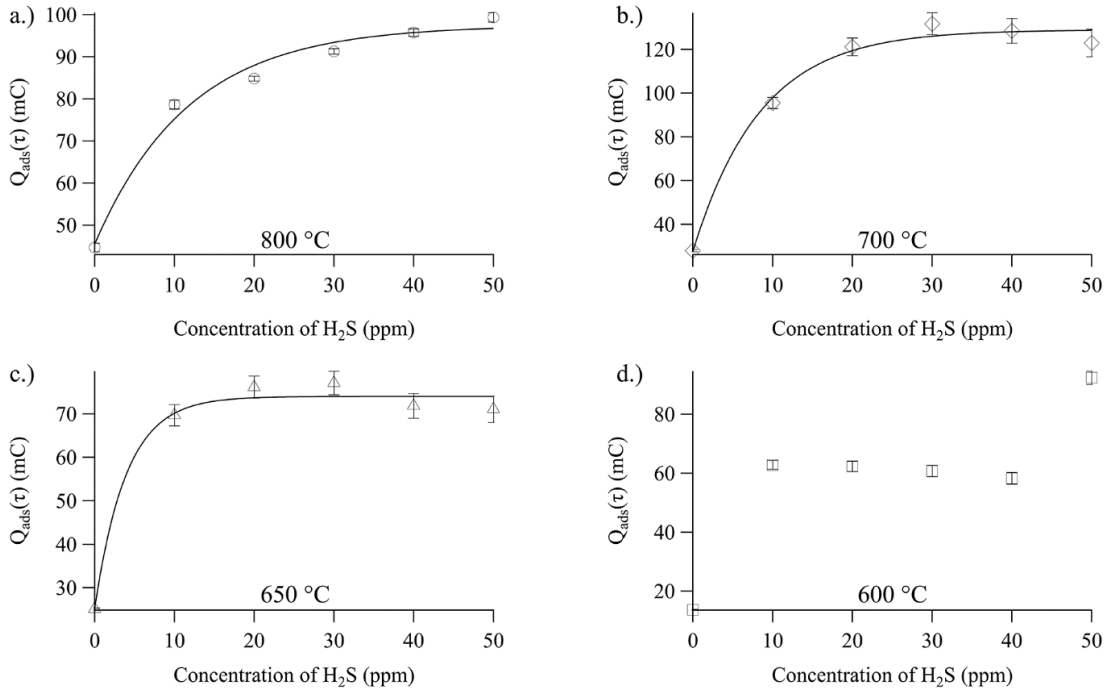

Figure 21 Chronocoulometry results of Q_{ads}(C.) as a function of H_2S concentration at a.) 800 °C, b.) 700 °C, c.) 650 °C, and d.) 600 °C.

Temperature	H_2S Concentration (ppm)	N (nmoles)	Θ_s when n=4	Θ_s when n=6
600	0	142 ± 1	0	0
	10		1.19 ± 0.03	0.71 ± 0.02
	20		1.18 ± 0.04	0.71 ± 0.03
	30		1.15 ± 0.04	0.69 ± 0.03
	40		1.08 ± 0.04	0.65 ± 0.03
	50		1.92 ± 0.05	1.15 ± 0.03
650	0	260 ± 3	0	0
	10		0.593 ± 0.03	0.36 ± 0.02
	20		0.67 ± 0.03	0.41 ± 0.02
	30		0.69 ± 0.03	0.42 ± 0.02
	40		0.62 ± 0.03	0.37 ± 0.02
	50		0.61 ± 0.03	0.37 ± 0.02
700	0	290 ± 6	0	0
	10		0.80 ± 0.04	0.48 ± 0.03
	20		1.11 ± 0.05	0.67 ± 0.04
	30		1.24 ± 0.05	0.74 ± 0.04
	40		1.20 ± 0.06	0.72 ± 0.04
	50		1.13 ± 0.03	0.68 ± 0.05
800	0	460 ± 11	0	0
	10		0.25 ± 0.03	0.15 ± 0.03
	20		0.29 ± 0.03	0.18 ± 0.03
	30		0.34 ± 0.03	0.21 ± 0.03
	40		0.38 ± 0.03	0.23 ± 0.03
	50		0.40 ± 0.03	0.24 ± 0.03

Table 1 Values for the number of active sites at each temperature as well as the surface coverage at each temperature and H_2S concentration from chronocoulometry.

The evolution of $Q_{ads}(0V,\tau)$ during the first 1.2 seconds are shown in Figure 20. Figure 20a shows how $Q_{ads}(0V,\tau)$ changes while operating with dry H_2 (with no H_2S) at temperatures ranging from 600˚C to 800˚C. Several trends are common to these traces at all temperatures. Specifically, $Q_{ads}(0V,\tau)$ rises smoothly at each temperature before turning over and decreasing. In one instance (700˚C), $Q_{ads}(0V,\tau)$ actually becomes negative for integration times ≥ 1.0 sec, caused by increased curvature in $Q(\eta, \tau)$. In general, $Q_{ads}(0V,\tau)$ increases with increasing temperature, a trend that likely reflects greater oxide transport through the electrolyte at higher operating temperatures. In addition, the maximum in

$Q_{ads}(0V,\tau)$, $Q_{ads,max}$, generally occurs at earlier times with increasing temperature. As described in more detail below, we propose that the time-dependent behavior of $Q_{ads}(0V,\tau)$ results from the parametric dependence of current on local and global temperature differences that drive $Q_{ads}(0V,\tau)$ to negative values in the absence of H_2S.

The remaining panels in Figure 20 show how $Q_{ads}(0V,\tau)$ behaves in the presence of H_2S at different operating temperatures. Contrary to expectation, introducing H_2S does not diminish the amount of charge generated but rather *increases* $Q_{ads,max}$ relative to the H_2S-free conditions shown in Figure 20a. In other words, adsorbed sulfur leads to more charge being available at early times through electrochemical oxidation. This effect appears to saturate at H_2S concentrations $\leq$ 20 ppm, especially at lower operating temperatures. The $Q_{ads,max}$ with lowest uncertainties recorded for each H_2S concentration at the four different operating temperatures are reported in Figure 21. At 800 °C and 700˚C, where the saturation effect is the least pronounced, concentration dependent $Q_{ads,max}$ results are statistically distinguishable. An analysis of theEIS data shown in Figure 16 found that at these higher temperatures both R_{bulk} and R_{pol} were statistically indistinguishable for different H_2S concentrations. At 600 °C and 650 °C, R_{bulk} was still statistically indistinguishable for different H_2S concentrations, but at these lower temperatures, R_{pol} increased upon the addition of 10 ppm H_2S. R_{pol} values were indistinguishable from each other at higher H_2S concentrations. In general, these data, both chronocoulometry and EIS, have saturated or approach an asymptotic limit as H_2S concentrations reach 50 ppm. These results highlight the utility of chronocoulometry as a tool for differentiating H_2S concentrations on SOFC electrodes, especially at higher temperatures. The saturation effect

was general in all cases, except for the marked increase in $Q_{ads,max}$ for 50 ppm H_2S at 600 °C. This measurement is unlikely to be an outlier since the value is calculated from 10 separate polarizations across 3 experiments, and is consistently higher than those measurements taken at 600˚C with 40 ppm H_2S. Future work will examine if this rise in $Q_{ads,max}$ at low temperatures and high pH_2S reflects new electrochemical oxidation reactions or simply an abrupt increase in the amount of adsorbed sulfur at lower temperatures. If the latter, this result may have consequences for the ability of intermediate temperature SOFCs to operate with fuels having high sulfur content.

Control experiments were carried out in order to assess the reliability of chronocoulometry as a means of evaluating an anode's electrochemical activity and to assess the effects of H_2S on anode performance in the absence of H_2. These studies consisted of performing chronocoulometry experiments under an inert, Ar atmosphere and under Ar with only 50 ppm H_2S (and no H_2). Data from these experiments had much greater uncertainties, resulting, in part, from presumed changes in anode microstructure that occurred during polarization without fuel.[20, 72, 95, 96] Results from these control studies are shown in Figure 22 and report $Q_{ads}(\tau)$ when no H_2 is available.

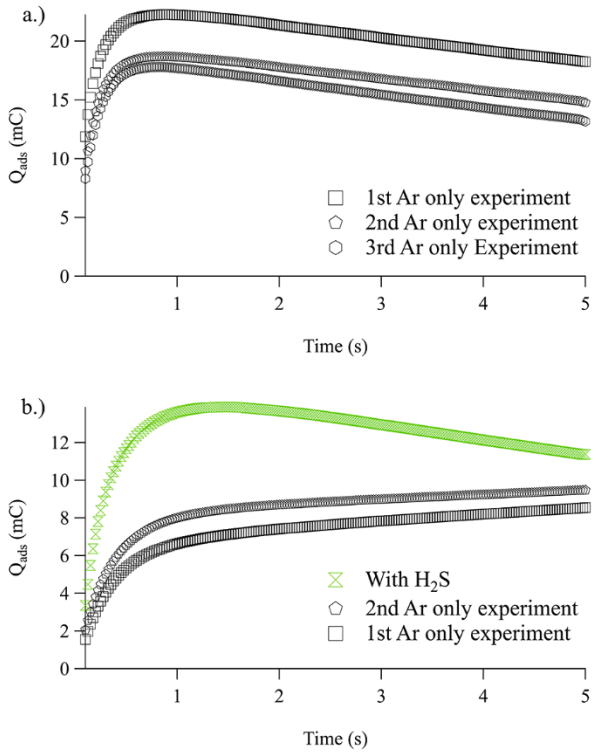

Figure 22 Results for experiments without H_2 at 700 °C a.) with only Ar and b.) with Ar only for the black traces, then 30 ppm H_2S for the green trace. The individual traces correspond to different experiments on the same fuel cell, with the first experiment being the first chronological experiment, followed by the 2nd and 3rd experiments.

These control experiments were carried out at 700˚C. In these experiments, the only source of current was electrochemical oxidation of the anode itself when Ar-only was used and anode Ni and H_2S in experiments carried out with Ar with 50 ppm H_2S. Qualitatively, the results in Figure 22a (Ar-only) are more similar to the behavior seen in Figure 20d (650˚C) and 20e (600˚C) with H_2S than those in 5c (700˚C) with uncontaminated H_2. These qualitative similarities imply a steady state of available charge at the TPB when operating without fuel (other than H_2S) and that anode oxidation is more similar to cases where H_2S is occupying active sites. Assuming that the only source of current is Ni oxidation, during

the first experiment, there were 245 nmoles of Ni oxidized at the lowest polarization, and 619 nmoles of Ni were oxidized at the highest. There were 166-530 nmoles oxidized during the second trial, and 133-496 nm oxidized during the last. The data in the absence of H_2S (Figure 22a) show a positive, slowly changing value for $Q_{ads}(\tau)$ over the duration of the polarization step. (Note that the data in Figures 22a and 22b extend to 5 sec rather than the 1.2 sec durations reported in Figure 18.) $Q_{ads}(0V,\tau)$ diminishes between experiments. That trend reverses in the presence of 30 ppm H_2S (Figure 22b), with increasing values for $Q_{ads}(0V,\tau)$ between experiments, but the qualitative behavior remains the same, with a positive value for the duration of the polarization. Similar to what was seen when operating with H_2, upon addition of H_2S the value for $Q_{ads}(0V,\tau)$ increases significantly. There were 185-887 nmoles of Ni oxidized during the first experiment (Ar-only), 165-784 nmoles during the second experiment. With H_2S added to the incident gas flow, the amount of charge produced (from either Ni or adsorbed H_2S) ranged from 74-950 nmoles. Continued presence of trace residual H_2S, despite thorough purging, may explain increasing $Q_{ads}(0V,\tau)$ between the Ar-only experiments reported in Figure 22b, but microstructural changes resulting from repeated Ni/NiO redox cycling could also explain the decrease in the total amount of charge generated between the 1st and 2nd experiments.

Several aspects of the chronocoulometry data warrant mention. First, in the absence of H_2S, $Q_{ads,max}$ rises monotonically with temperature (Figure 20a and Table 1). Since hydrogen oxidation is the dominant source contributing to $Q_{ads,max,}$ the increased value could indicate an increased number of TPB active sites, increased oxide conductivity, or both. (This assessment assumes that H_2 dissociative chemisorption to the Ni surface is not

rate limiting.) Second, the introduction of H_2S at all temperatures causes a rise in the value of $Q_{ads,max}$. This rise is readily evident in Figure 21. Similar to the thermal imaging results, the results in Figures 21a-c indicate that any effects from H_2S saturate at ≤ 20 ppm at temperatures below 800 °C. Also, the sharp rise in $Q_{ads,max}$ at 600 °C and 50 ppm H_2S noted earlier is curious and unexplained. Third, interpreting $Q_{ads,max}$ as a function of the operating temperature presents challenges. If $Q_{ads,max}$ reflected primarily the amount of adsorbed sulfur, then one might conclude that the anode at 700˚C has accumulated the most sulfur. This conclusion is not supported by thermal imaging data (Figure 19) nor the EIS data (Figure 16).

Arrhenius Analysis.

Figure 23 shows extended $Q_{ads}(0V,\tau)$ traces out to 5 sec for cells operating with H_2 (black) and H_2 with 50ppm H_2S (green) at 800˚C (Fig 8a) and 600˚C (Fig 8b). In the absence of H_2S, as can be seen in Figure 23a and the H_2-only data in 8b, $Q_{ads}(0V,\tau)$ eventually assumes negative values with no sign of approaching an asymptotic limit. Only when operating at low temperature (600˚C) in the presence of H_2S does $Q_{ads}(0V,\tau)$ reach a limiting positive value as would be expected for an ideal RC circuit. Changes in the value of $Q_{ads}(0V,\tau)$ are unexpected, and as noted earlier, are attributed to changes in the curvature of $Q(\eta,\tau)$. To determine if a change in curvature was occurring, we examined the chronoamperometry data from each potential step in a chronocoulometry experiment. A detailed analysis of the chronoamperometry data showed that an SOFC operating with H_2 (in the absence of H_2S) produced increasing current shortly after capacitive discharge rather than reaching a steady state value that would be expected for an ideal RC circuit.

This non-ideal behavior was more pronounced at higher polarizations and higher operating temperatures. Conversely, following exposure to H_2S at lower operating temperatures, the chronoamperometry data resembled ideal RC behavior and reached a constant steady state value. This "ideal" behavior was also observed for experiments performed without fuel (Figure 22).

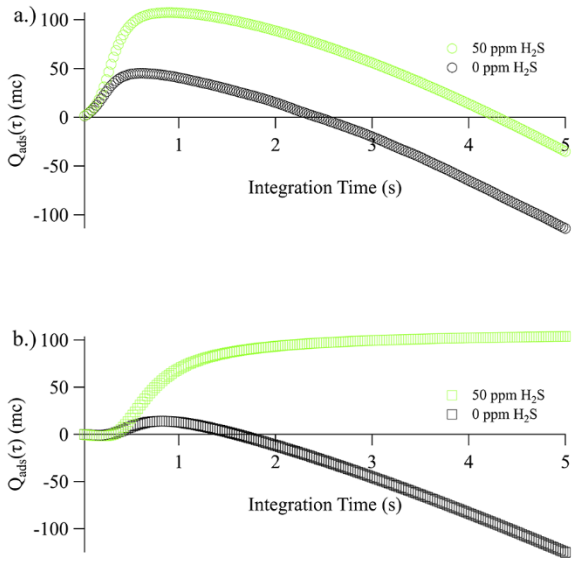

Figure 23 Plots of $Q_{ads}(\tau)$ at a.) 800 °C with 50 ppm H_2S and without and b.) 600 °C with 50 ppm H_2S and without shown til 5 seconds.

We propose that the higher currents (and corresponding $Q_{ads}(0V,\tau)$) at higher operating temperatures can be attributed to cell heating from electrochemical H_2 oxidation during polarization. Higher temperatures accelerate oxide transport and increase electrochemical oxidation at a given overpotential. Since current for a fuel cell system is a direct measure of the electrochemical oxidation rate, and since this rate is, by definition, proportional to a rate constant, we used the measured current at a given time and the corresponding change in surface temperature within the ROI obtained from the thermal

imaging to generate 1st order Arrhenius plots. In carrying out this analysis, the points prior to the current reaching the minimum value were removed since the deviation from a steady state value after capacitive discharge was the behavior of interest.

The plots resulting from this analysis at 600 °C and 800 °C are shown in Figure 24. The values for temperature are determined via thermal imaging of the cell during polarization. Figure 24a, 24b, and 24c show a clear linear correlation between log current vs T^{-1} whereas no such correlation is evident in Figure 24d (600˚C, 50 ppm H_2S). The slopes of the plots in Figures 24a, 24b, and 24c are not truly reflective of traditional activation energies since the current is measured for the entire cell, while the thermal imaging data report on only a small region of the cell where the greatest thermal changes occurred. However, the strong correlation *does* indicate that the observed deviation from ideal circuit behavior is a thermally activated process driven by the exothermic H_2 oxidation. The results in Figure 19a and 19e show a strong correlation between the localized thermal changes on the anode surface and polarization. Since the current depends on both operating temperature and potential, $Q(\eta,\tau)$ shows a parametric dependence on temperature, giving it a positive curvature driving down the value of $Q_{ads}(0V,\tau)$. Where the thermal changes of the cell are minimal (Figure 23b) the value of $Q_{ads}(\tau)$ remains positive and stable.

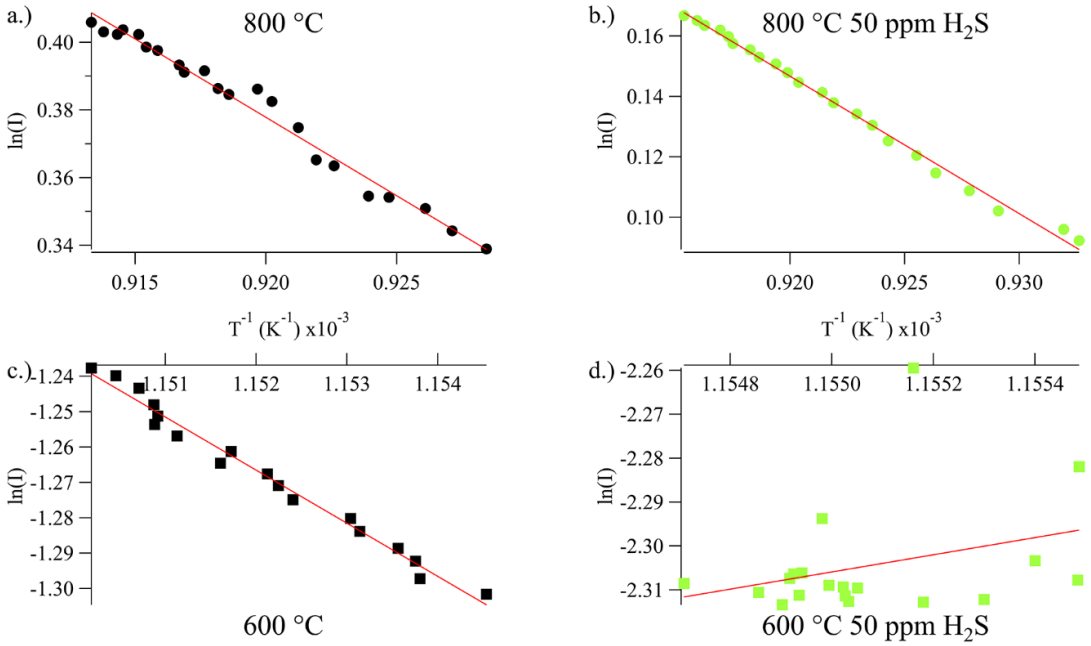

Figure 24 Results from Ahhrenius analysis a.) without H_2S at 800 °C, b.) with H_2S at 800 °C, c.) without H_2S at 600 °C, d.) with H_2S at 600 °C. 1st order Arrhenius plot results are shown as red lines.

800 0 ppm H_2S		800 50 ppm H_2S		600 0 ppm H_2S		600 50 ppm H_2S	
T (°C.)	I (Amps)	T (°C.)	I (Amps)	T (°C.)	I (Amps)	T (°C.)	I (Amps)
804.1	1.403	799.3	1.097	593.1	0.2721	592.7	0.1044
805.6	1.411	800.0	1.101	593.7	0.2733	592.4	0.1021
806.8	1.420	803.3	1.108	593.7	0.2747	592.8	0.1009
808.4	1.425	804.8	1.115	593.9	0.2757	592.5	0.0999
809.3	1.426	806.5	1.122	594.2	0.2770	592.4	0.0995
810.9	1.438	807.5	1.128	594.3	0.2780	592.8	0.0993
811.7	1.441	808.9	1.133	594.8	0.2795	592.6	0.0990
812.5	1.455	809.7	1.139	594.9	0.2806	592.9	0.0989
813.7	1.466	810.5	1.144	595.0	0.2815	592.8	0.0990
814.3	1.471	811.7	1.148	595.4	0.2824	592.7	0.0990
815.6	1.469	812.3	1.152	595.3	0.2833	592.8	0.0991
816.1	1.472	813.5	1.156	595.7	0.2845	592.8	0.0991
816.7	1.479	814.1	1.159	595.9	0.2855	592.9	0.0992
817.7	1.479	814.7	1.163	595.9	0.2861	592.8	0.0993
817.9	1.482	815.6	1.165	595.9	0.2871	592.8	0.0994
818.9	1.488	816.0	1.168	596.0	0.2884	593.0	0.0994
819.4	1.490	816.9	1.171	596.2	0.2894	592.9	0.0995
819.7	1.495	817.1	1.173			592.8	0.0996
820.4	1.497	817.6	1.176			592.9	0.0996
820.7	1.495	818.4	1.178				
821.3	1.496	818.8	1.180				
821.9	1.501	819.5	1.181				

Table 2 The values of temperature and current for the Ahrrenius analysis at 800 and 600 °C, with 50 and 0 ppm H2S

Discussion.

Polarization-driven changes in electrode surface temperature as measured by NIRTI are sensitive to operating temperature (Figure 19a). The effects of H_2S also show a strong temperature dependence, with H_2S having the very little effect on ΔT at 800˚C (Figure 19b) and a strong suppression of ΔT at 600˚C (Figure 19e). A simple explanation is that at lower temperatures S more strongly binds to electrochemically active sites at the

triple phase boundary and inhibits H_2 oxidation leading to measurably smaller ΔT at the anode surface as a function of applied overpotential. At higher temperatures, sulfur adsorption/desorption favors S desorption, limiting the amount of adsorbed sulfur and ΔT is much less pronounced.

The thermal response is not the only observable that depends on system temperature. The magnitude of $Q_{ads,max}$ also shows a significant temperature dependence (Table 1). In principle $Q_{ads,max}$ should reflect the electrochemically active TPB length and be determined by the electrode geometry. Assuming that electrode microstructure doesn't change measurably during a chronocoulometry experiment, one might reasonably expect $Q_{ads,max}$ to remain constant. In the limit that $Q_{ads,max}$ reflects the amount of charge available through electrochemical oxidation of species adsorbed to the TPB, a rising $Q_{adss,max}$ implies either a larger fraction of occupied sites for a fixed TPB *or* more TPB becoming available as operating temperature increases. Previous studies have shown that at SOFC operating temperatures, a reducing atmosphere and strong anodic overpotentials both deplete oxides from a YSZ surface.[48, 97] Without available oxides at the TPB, electrochemical reactions cannot proceed. Given the high activation energy required for oxide diffusion through YSZ, one expects that the electrochemically active depth of a Ni-YSZ cermet anode to more restricted at lower temperatures simply due to slower oxide diffusion kinetics through the YSZ cermet network. Therefore, we propose that $Q_{ads,max}$ increases with operating temperature due to increased oxide percolation throughout the anode microstructure thereby increasing the number of available sites for electrochemical oxidation and the apparent TPB length.

The addition of H_2S also leads to a significant rise in the value of $Q_{ads,max,}$ as is readily apparent in Figure 21. Adding small amounts of H_2S to the incident fuel results in a clear and significant rise in the amount of charge generated in a chronocoulometry experiment. By making several assumptions, we can use the $Q_{ads,max}$ data to estimate the relative surface coverage of sulfur, Θ_S. The first assumption is that H_{ads} and S_{ads} both use the same active sites in the TPB. Generally, both S and H are known to adsorb to single Ni atoms.[98, 99] Next, if we assume that the number of sites at equilibrium does not change between experiments, and that S reacts to form products with adsorbed S having only a single oxidation state, then any mechanism describing the electrochemical oxidation occurring in a chronocoulometry experiment needs to include only two generalized chemical reactions:

$$2\mathrm{H_{ads}} + \mathrm{O^{2-}} \rightarrow \mathrm{H_2O} + 2\mathrm{e^-} \tag{8}$$

$$\mathrm{S_{ads}} + \frac{n}{2}\mathrm{O^{2-}} \rightarrow \mathrm{SO_{\frac{n}{2}}} + n\mathrm{e^-}. \tag{9}$$

The amount of charge generated from H_{ads} and contributing to the chronocoulometry data is then

$$Q_{ads,H} = F\Gamma_H A \tag{10}$$

and the amount of charge from S_{ads} is

$$Q_{ads,S} = \frac{n}{2}F\Gamma_s A \tag{11}$$

where A is the length of the TPB, Γ_H and Γ_s are the surface concentrations of hydrogen and sulfur, respectively, and F is Faraday's constant. The number of active sites can be expressed as

$$N = \Gamma_H A + \Gamma_s A. \tag{12}$$

In the absence of S_{ads}, N depends only on adsorbed hydrogen and the total number of active sites (N_0) is obtained:

$$N_0 = \Gamma_{H,0} A = \frac{Q_{ads,H,0}}{F}. \tag{13}$$

When $S_{ads}>0$, the total charge from adsorbed species must be

$$Q_{ads,H,S} = Q_{ads,H} + Q_{ads,S} \tag{14}$$

or, by substitution,

$$Q_{ads,H,S} = F\Gamma_H A + 4F\Gamma_s A. \tag{15}$$

By eliminating $\Gamma_s A$, $Q_{ads,H,S}$ becomes

$$Q_{ads,H,S} = F\Gamma_H A + nF(N - \Gamma_H A) \tag{16}$$

which can be rearranged to solve for $\Gamma_H A$ to become

$$\Gamma_H A = \left(\frac{n}{n-1}\right) N - \frac{Q_{ads,H,S}}{(n-1)F}. \tag{18}$$

The surface coverage of S_{ads} then becomes

$$\Theta_s = \frac{N_0 - \Gamma_H A}{N_0}. \tag{19}$$

Using this treatment, Θ_S can be found for each temperature and concentration used, and can be found in Table 1.

Assuming SO_2 is the primary SO_x product results in non-physical values for Θ_S at some temperatures. If a combination of SO_x species produced where n=4 (SO_2) and n=6 (SO_3), then calculated surface coverages fall into a plausible range. The case where n=2, or when SO gas is produced, is not considered since SO_2 and SO_3 are both more thermodynamically favorable and SO_2 is kinetically more favorable.[99, 100] Comparing sulfur coverages calculated from Equation 18 and 19 show a clear trend with higher Θ_S (approaching or exceeding 1.0) at 600 °C as compared to 800 °C. This trend agrees with substantially reduced surface temperature changes observed at 600 °C as measured by thermal imaging. At 800 °C Θ_S is low (< 0.5) and sulfur's poisoning effects, as measured by thermal imaging, are negligible. Surprisingly, even with Θ_S ~ 20% - 30% at 800 °C, thermal imaging shows no measurable thermal cooling brought about by S adsorption. Additionally, with Θ_S between 70 and 100% at 600 °C, the thermal response was only diminished by 58% by introduction of 50 ppm H_2S. Were H_2S merely blocking active sites in the TPB, performance would be expected to diminish linearly with Θ_S . Therefore, the mechanism responsible for SOFC anode sulfur poisoning must involve more involved chemistry than simply blocking active sites. Together with the increase in $Q_{ads,max}$ in the presence of H_2S, S_{ads} must be participating in electrochemical oxidation, thereby diminishing SOFC anode performance with sluggish electrochemical oxidation kinetics. Such a situation may promote anode Ni oxidation as has been reported for Cl contamination, but this possibility remains to be tested.[55, 72]

Finally, strong linear correlations between the rate of electrochemical oxidation and inverse temperature shown in Figure 24a, 24b, and 24c support three conclusions. First, electrochemical oxidation of H_2 and H_2S on SOFC anodes generally follows first order kinetics. Second, whatever process is responsible for S oxidization at lower temperatures (e.g. 600˚C) is not a first order kinetic process. Lastly, deviations from expected electrochemical behavior observed in the generated current are due to the thermally activated changes in the electrochemical oxidation of H_2 and H_2S. Together with the uncorrelated behavior observed in Figure 24d, the observed anode heating during polarization likely causes the deviations from expected chronoampometry behavior. Since the temperature changes are also polarization dependent, Figure 19, the increased current from heating added additional curvature to $Q(\eta,\tau)$, driving down the value of $Q_{ads}(0V,\tau)$, and eventually driving it to the negative values observed in the chronocoulometry at longer times. When this heating does not occur such as at lower temperatures in the presence of H_2S, $Q_{ads}(0V,\tau)$ remains relatively constant and consistent with expected electrochemical behavior for an ideal R-C circuit.

Conclusions

Chronocoulometry, when coupled with optical techniques including thermal imaging, is an effective tool that enables one to infer mechanisms of SOFC operation. Not only is the method sensitive to changes in gas composition, it can also measure changes in the number of reactive sites as a function of temperature. Increasing system operating temperature improves SOFC performance by improving oxide flux through the electrolyte and by increasing the number of available active sites in the anode. This effect is attributed

to an increase in TPB length resulting from improved oxide diffusion kinetics throughout the anode microstructure. The amount of H_2S adsorbed on the cell diminishes with increasing system temperature, and chronocoulometry data show that H_2S does not simply block active sites in the TPB. Instead H_2S participates in electrochemical reactions, thereby reducing reactivity and increasing cell resistance through sluggish oxidation kinetics. A complicated interdependence exists between the temperature changes and chronocoulometry results and was assigned to an Arrhenius-like temperature dependence. Since chronocoulometry is newly adapted to SOFCs, non-ideal behavior leads to challenges when interpreting results. However, by coupling chronocoulometry with thermal imaging, the source of non-ideal electrochemical behavior was identified to be thermally induced, and this correlation demonstrated that oxidation reactions in SOFC anodes are typically driven by first order kinetic processes. Chronocoulometry will continue to be a powerful new tool in the arsenal of electrochemical analytical techniques used to study SOFCs.

Acknowledgments

The authors gratefully acknowledge support from the Office of Naval Research (Grant numbers N00014-17-1-2808 (MSU) and N0001419WX00410 (NRL)).

CHAPTER FOUR

OPERANDO OPTICAL STUDIES OF SULFUR CONTAMINATION IN SYNGAS OPERATION OF SOLID OXIDE FUEL CELLS

Contribution of Authors and Co-Authors

Manuscript in Chapter 4

Author: William A. Maza

Contributions: Conceptualization, methodology, data collection and analysis, writing-original draft, review and editing

Co-Author: Elias D. Pomeroy

Contributions: Conceptualization, methodology, data collection and analysis, writing-review and editing

Co-Author: Daniel A Steinhurst

Contributions: Data collection and analysis, writing-review and editing

Co-Author: Jeffrey C. Owrutsky

Contributions: Supervision, funding acquisition, Writing-review & editing

Co-Author: Robert A. Walker

Contributions: Supervision, funding acquisition, Writing-review & editing

Manuscript Information

William A. Maza, Elias D. Pomeroy, Daniel Steinhurst, Robert A. Walker, and

Jeffrey C. Owrutsky

Journal of Power Sources

Status of Manuscript:
____ Prepared for submission to a peer-reviewed journal
____ Officially submitted to a peer-reviewed journal
____ Accepted by a peer-reviewed journal
_x__ Published in a peer-reviewed journal

Elsevier

Published: October 31, 2021
DOI: 10.1016/j.jpowsour.2021.230398

OPERANDO OPTICAL STUDIES OF SULFUR CONTAMINATION IN SYNGAS OPERATION OF SOLID OXIDE FUEL CELLS

William A. Maza[a], Elias D. Pomeroy[b], Daniel Steinhurst[c], Robert A. Walker[b], and Jeffrey C. Owrutsky[1]

a. Chemistry Division, US Naval Research Laboratory, Washington, D.C.
b. Department of Chemistry and Biochemistry, Montana State University, Bozeman, MT
c. Nova Research, Inc., Alexandria, VA

Abstract

Near-infrared thermal imaging, voltammetry, and chronocoulometry have been used to examine electrochemical oxidation mechanisms in solid oxide fuel cells (SOFCs) operating with model syngas mixtures ($CO + H_2$) at 800 °C with and without a sulfur-containing contaminant. Questions persist regarding the electrochemical oxidation of H_2 vs. CO especially on the role of CO activation and CO mobility in porous SOFC cermet anodes. Chronocoulometry, electrochemical impedance spectroscopy, and *operando* optical methods are also used to characterize contaminant effects of SOFC operation at 800 °C in the presence of 50 ppm(v) sulfur to gain insight into its effect on syngas SOFC operation. The chronocoulometry results indicate that in the absence of sulfur contaminants, electrochemical oxidation of adsorbed CO does not contribute to current

production, possibly because of rapid carbon formation at the anode surface. This discovery suggests that initially adsorbed H_2 is the primary source of charge at early times in the electro-oxidation of syngas fuels. Furthermore, in the presence of sulfur contaminants, chronocoulometry data show that S competitively occupies ~ 30% of the electroactive sites at the triple phase boundary and contributes to the total initial charge likely via electrochemical oxidation of S to SO_2.

Introduction

Synthesis gas, or syngas, is a mixture of H_2, CO, sometimes containing small amounts of CO_2, often generated by the reforming of carbon and carbon containing fuels using oxidants such as H_2O, CO_2, or O_2. These processes are also known as wet reforming, dry reforming, and partial or full oxidation (depending on the relative concentrations of O and C present), respectively, and they play an integral role in strategies for efficient and durable SOFC power generation from a wide array of fuel sources. [101-103] In addition to the primary components of syngas, these fuel mixtures often include impurities such as sulfur- and chlorine- containing species as well. These impurities are detrimental to SOFC operation and can cause electrode degradation and device failure. [104-106]

Despite their importance to SOFC operation, the contributions of H_2 and CO to power generation with syngas fuels are still uncertain.[107-117] H_2 is believed to be the primary source of power production in SOFCs operating with syngas [15, 67, 114, 118], although CO oxidation is believed to occur at larger overpotentials.[113, 117] Moreover, a multi-step mechanism describing CO oxidation has been proposed that depends on the relative concentrations of CO and CO_2. [115] Direct evidence validating these mechanisms remains

elusive, however, and even less is known about how contaminants affect H_2 and CO electrochemical oxidation SOFCs. [102, 119]

Recently, we have coupled *in situ* electrochemical methods with *operando* Raman spectroscopy [23], Fourier transform infrared emission spectroscopy [120], and *operando* near infrared thermal imaging [120] to develop material- and molecule- specific insight into the processes controlling simulated syngas conversion in SOFCs. [120] O*perando* Raman spectroscopy has shown that highly ordered graphitic carbon readily forms at the anode surface of SOFC membrane electrode assemblies (MEAs) at open circuit potential as a result of the reverse Boudouard reaction. [120] Significantly less carbon is deposited on the anode when the SOFC is polarized galvanostatically.[23, 120] These studies noted that carbon formation on the anode surface appeared to follow zeroth order kinetics and should, therefore, be independent of the fuel stream's CO content.[120] Data showed that the amount of carbon formed on the anode surface also depends on the SOFC's operational temperature with significantly less carbon observed at temperatures above 750 °C. [120] Along these lines, we have long been interested in the nature and mechanisms of carbon formation and removal from the surfaces of anodes [24, 34, 37, 121] and the effect of contaminants such as sulfur and chlorine.[51, 55, 73, 94, 122]

Recently, results from *operando* Fourier transform infrared emission spectroscopy (FTIRES) and near infrared thermal imaging (NIRTI) indicated that CO may play a role in power generation at 800 °C despite the electrochemical oxidation of H_2 being more kinetically favored and that electrochemical oxidation of CO likely occurs via direct oxidation of CO. [120] Furthermore, any surface carbon (C^*) formed from the reverse

Boudouard reaction is probably removed via gasification with H_2O formed *in situ* by the electrochemical oxidation of H_2. These results support an active role of CO to power generation in syngas fuels [113, 116, 117] but fail to fully address the mechanism of CO conversion to power and, more importantly, the role of carbon formation on power generation and durability. [23, 120] Electrochemical conversion of H_2 to H_2O and CO to CO_2 occurs solely at the nominal three-phase boundary (TPB) in a Ni-YSZ cermet anode. Therefore, knowing if the TPB active-site occupancy reflects the incident fuel composition and assessing the relative barriers required for electrochemical oxidation are important questions that need to be resolved in order to validate and benchmark proposed syngas electrochemical oxidation models.

Our spectroelectrochemical toolbox using *operando* spectroscopies and thermal imaging coupled with simultaneous electrochemical measurements has been expanded to include the chronocoulometry technique. [94, 122] Chronocoulometry has long been used to quantify the adsorption of redox active species on an electrode surface in solution-phase electrochemistry. [40, 123, 124] We combined chronocoulometry with imaging data to investigate sulfur degradation mechanisms in SOFCs operating with H_2 and H_2/H_2S fuels at various temperatures and observed an increase in the charge extracted from surface bound species when S was present, implying that sulfur adsorbed to the SOFC anode's TPB could be electrochemically oxidized.[94, 122] In the studies described below, we present results obtained using chronocoulometry coupled with simultaneous NIRTI measurements to examine the electrochemical oxidation of simulated syngas on Ni-YSZ anodes at 800 °C. In these experiments, the relative amounts of H_2 and CO are varied in order to ascertain

the roles of H_2 and CO in SOFC power generation. The results represent the first time the decrease in the total occupancy of H at electrochemically active sites is quantified in the presence of CO in the form of syngas fuels as well as in the presence of sulfur. In the initial period following application of an overpotential, adsorbed CO does not appear to be oxidized and, in fact, appears to inhibit the overall amount of electrochemical oxidation. Curiously, introducing S (as H_2S) increases the amount of charge collected at a given potential suggesting that as a potential contaminant, CO, may prove as deleterious to efficient SOFC operation as S.

Experimental

Solid oxide fuel cells and membrane electrode assemblies (MEA).

The 25 mm diameter electrolyte-supported NextCell™ button cells (Fuel Cell Materials, Inc., Item# 213206) membrane electrode assemblies were obtained commercially and were comprised of a 12.5 mm diameter 50 μm thick NiO-YSZ/NiO-GDC anode, 25 mm diameter 170 μm thick YSZ-Hionic™ electrolyte, and a 12.5 mm diameter 50 μm thick LSM/LSM-GDC cathode. The functional layers in the anode and cathode are NiO-YSZ and LSM, respectively; and the GDC-composites are interlayers separating the anode and cathode from the electrolyte for reasons that are not immediately apparent from the manufacturer's website. We will note that ceria containing interlayers are commonly used to block chemical reactions between LSM cathodes and YSZ which can lead to the ultimate loss of performance.[125] On the anode side, GDC-composites have been implicated in contributing to an increase in the sulfur tolerance of anode. [126] The formulation and fabrication of the button cells is proprietary to Fuel Cell Materials, Inc;

the button cells used were all of the same composition and were used as received without modification.

Conductive Au (Fuel Cell Materials, Inc., Item # 233001) and Pt (Fuel Cell Materials, Inc., Item # 233002) inks coupled the electrodes to Au (anode, 100 mesh, 99.99%, Fisher Scientific) and Pt (cathode, 100 mesh, 99.9%, Sigma-Aldrich) current collectors ($A \approx 0.75$ cm^2), respectively. A third electrode (Au, 100 mesh, 99.99%, Fisher Scientific) was affixed to the surface of the electrolyte with conductive Au ink at a distance > 5 mm from the anode (Figure 25). The MEAs were mounted on the end of a 2.54 cm diameter alumina tube (Sentro Tech Corp.) with Ceramabond 552 (Aremco Products, Inc). This was encased in a 48.1 mm OD alumina tube, together with two 6.35 mm OD alumina tubes used as gas inlet and outlet ports, and capped on one end with a 50.8 mm diameter, 3 mm thick, sapphire polished IR optical window allowing optical access to the anode surface. The assembly was placed in a tube furnace together with an additional thermocouple affixed to the exterior of the assembly for calibration of the thermal imaging data and heated to 800 °C overnight at a ramp rate of 1 °C/min.[50]

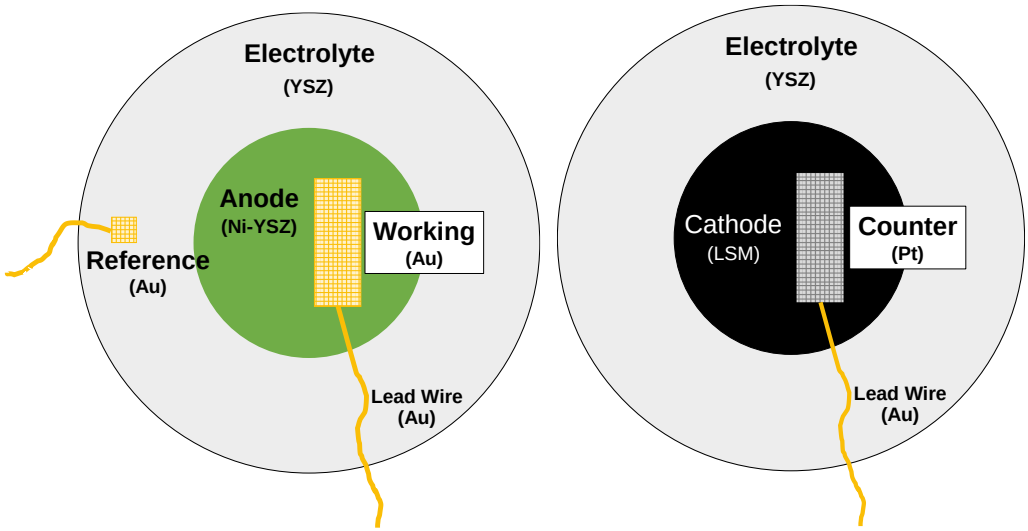

Figure 25 Schematic of the three-electrode arrangement collectively on the anode side (left) and cathode side (right) of the membrane electrode assembly.

Electrochemical experiments.

Chronocoulometry and linear sweep voltammetry (LSV) experiments are performed using a Gamry Reference 3000 potentiostat/galvanostat/ZRA. Chronocoulometry experiments are carried out in a three-electrode arrangement (Figure 25) and LSV experiments are conducted in a two-electrode arrangement. In a typical chronocoulometry experiment, cells are polarized to given overpotentials (η), defined as the difference between the applied potential (E_{app}) and the open circuit potential (E_{ocv}), for ten seconds before returning to E_{ocv}. After returning to E_{ocv} the cell is allowed to equilibrate for an additional sixty seconds to replenish the surface with unreacted fuel before the next potential step.

Near infrared thermal imaging

The NIRTI technique is described in detail elsewhere.[50, 53, 54] Briefly, a CCD camera (Allied Vision Technologies, Stingray F033B ASG) equipped with a telephoto lens

(Navitar, Zoom 7000) and a long-pass optical filter (λ_{cutoff} < 720nm) is used to monitor near-IR emission of the anode surface to spatially resolve the temperature of the anode. A thermocouple affixed to the SOFC assembly tube is used to calibrate the recorded emission intensity corresponding to the surface temperature of the anode. The temperature range of the calibration is one in which the spectral response of the camera is linear (typically $\Delta T < 50$ °C). The values of ΔT reported in this report correspond to the difference in temperature at η obtained at the given time from the average temperature at E_{ocv} under a given fuel mixture.

Results and Discussion

H_2 and syngas fuels (without H_2S)

The maximum current for operation of an electrolyte supported cell with H_2 fuel is ~190 mA, so considering the area of the anode current collector is 0.25 cm^2, the maximum power density at 0.51 V is 0.19 W/cm^2. LSV traces obtained under H_2 and simulated syngas mixtures (the term syngas will refer to simulated syngas from this point forward) having varying compositions indicate that the electrochemical performance of electrolyte-supported MEAs decreases with decreasing H_2 content (Figure 26 and Table 3). For syngas mixtures in which the total fuel content is kept constant at 50%, the short circuit current density (I_{max}), defined as the current density at which the potential difference between the anode and cathode approach zero, and maximum power (P_{max}) output both decrease with increasing CO and decreasing H_2-content. The reduction in the I_{max} and P_{max} with increasing CO-content agrees with previous results. [118, 120]

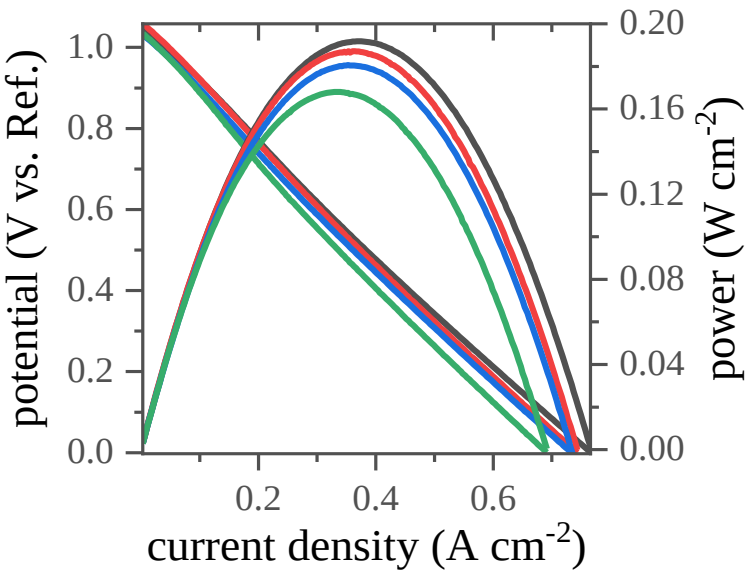

Figure 26 I-V, power curves of SOFC MEAs under 50% H_2 (black) and syngas fuels of varying H_2 and CO compositions containing 50% H_2 + 25% CO (red), 45% H_2 + 5% CO (blue), and 25% H_2 + 25% CO (green) obtained at 800 °C.

Mechanisms responsible for electrochemical oxidation of syngas fuels have generated considerable debate. In particular, the role of CO in the generation of electrochemical power continues to be a topic of great uncertainty.[67, 109, 113, 114, 116-118] The predominant view is that H_2 oxidation dominates electrochemical oxidation at the anode.[67, 114] Questions arise, however, about the role of CO in electrochemical reactions.[67, 127] Electrochemical oxidation of H_2 is kinetically preferred over CO due to the large difference in mass transfer throughout the porous anode network.[67, 114] Moreover, some reports have suggested that contributions to power generation from CO oxidation are negligible in the presence of H_2 and that any CO-derived power is due to the formation of H_2 by the reaction of CO and H_2O by the water-gas-shift (WGS) reaction, Equation 20.[128-130]

$$CO + H_2O \rightarrow CO_2 + H_2 \quad (20)$$

$\Delta H°_{298}$ = -41 kJ mol^{-1}

Other models, however, have included electrochemical CO oxidation and suggest that this syngas component *can* contribute to the overall power output, albeit only at large overpotentials .[113, 115, 117] (Values for the enthalpies of electrochemical oxidation reactions throughout this work are calculated using Hess's Law with values obtained in Table 3 of reference [130]; the value for O^{2-} is assumed to be near the value of O(s). These values are validated by independently calculating the reaction enthalpies associated with the WGSR and wet reforming (-39 kJ mol^{-1} and 215 kJ mol^{-1}, respectively) which are found to be within 5% of the accepted values (-41 kJ mol^{-1} and 206 kJ mol^{-1}, respectively). [131]

Chronocoulometry is a widely used method to probe the adsorption of electrochemically active species onto an electrode surface. [40, 123, 124] This technique is particularly useful in quantifying the surface coverage of the redox active species. Chronocoulometry involves polarizing the electrochemical cell from an initial cell potential with no Faradaic current contribution (e.g. E_{ocv}) to a second potential (E_i) where the Faradaic current is non-zero; we define the difference between E_i and E_{ocv} as the cell overpotential (η). Returning to E_{ocv} for a sufficient period ensures desorption of any electrochemically produced product(s) and allows replenishment of unreacted species on the electrode surface. By monitoring the charge generated (Q_{ads}) as a function of applied overpotential, we can semi-quantitatively assess differences in surface coverage and consumption of fuels at the Ni-YSZ anode as well as the effect of contaminants on these

parameters. This technique has been demonstrated previously on SOFCs [94, 122] where the effect of H_2S on SOFC anodes operating with H_2 was probed as a function of temperature.

The number of adsorbed species, or the occupancy of the electrochemically accessible area (Γ_{ads}, mol cm^{-2}), at the triple phase boundary (TPB) is related to Q_{ads} according to Equation 21:

$$Q_{ads} = nFA\Gamma_{ads} \tag{21}$$

where n is the number of electrons involved in the electrochemical reaction, F is Faraday's constant, and A is the electrochemically active area of the electrode (taken here to be the area of the current collector, ≈ 0.25 cm^2). An example of the temporal galvanic response (Figure 27a), the anode surface temperature change (Figure 27b), and the resulting charge (Figure 27c) over a potential-step (at η = 1.0 V) with H_2 as the fuel (50% by volume with an Ar balance) is shown in Figure 27. Q' plotted in Figure 27c is the intercept of Q vs η at each time point over the potential step.The maximum in Figure 27c corresponds to Q_{ads}. Under 50% H_2 this maximum occurs between 0.6 sec and 0.8 sec after the start of the applied overpotential and yields a $Q_{ads,H}$ value of ~11 mC. Using Equation 21 this amount of charge corresponds to a H_{ads} occupancy ($\Gamma_{ads,H}$) of 1.5x10^{-7} mol cm^{-2} (n = 1 for the electrochemical oxidation of H) at the TPB and is on the same order of magnitude as what has been previously reported. [122]

The transient overpotential applied in a chronocoulometry experiment leads to temperature changes across the anode. These changes are monitored using NIRTI and can be correlated directly with Q_{ads}. The reaction corresponding to Q_{ads} is the electrochemical

oxidation of H on the surface of the Ni-YSZ at or near the TPB. This reaction is endothermic (reaction 3) and should lead to anode surface cooling:

$$2H(Ni) + O^{2-} \rightarrow H_2O + 2e^-(Ni) \quad (22)$$

$\Delta H°_{298}$ = 78 kJ mol^{-1}

However, the NIRTI data in Figure 27 show clearly that oxidation of adsorbed H leads to anode heating which has been previously documented.[93, 120, 122] This anode heating continues past the time corresponding to $Q_{ads,H}$ approaching an equilibrium temperature, ΔT_{eq}, at ~ 10 sec after polarization; this behavior is consistent at all η. An exothermic dissociative H_2 adsorption replenishes the surface hydrogen, contributing to the observed thermal changes:

$$H_2 \rightarrow 2H(Ni) \quad (23)$$

$\Delta H°_{298}$ = -84 kJ mol^{-1}

which, together with reaction 3, may account for the anode heating. While it can be argued that the thermal changes reflect the reaction enthalpy associated with the net electrochemical oxidation reaction of H_2 to produce H_2O (reactions 3 & 4, $\Delta H°$ ~ -6 kJ mol^{-1}) [50, 130], the reaction mechanism is more complex and requires additional data before the elementary steps can be validated.

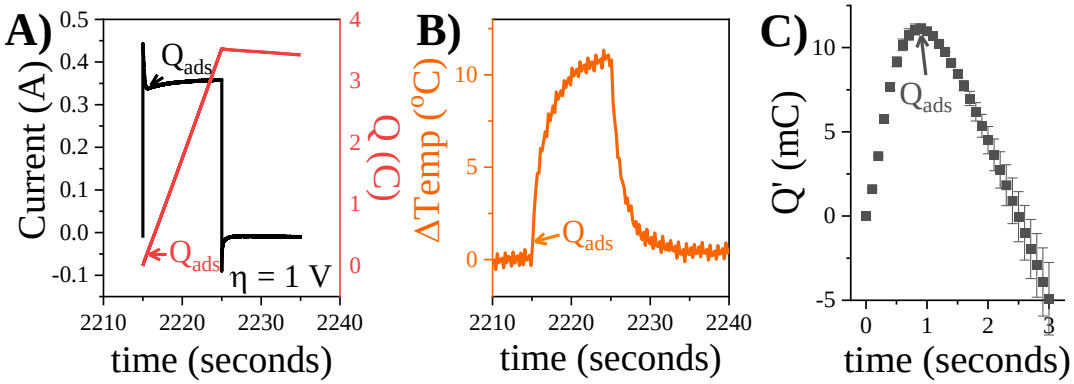

Figure 27 A) Overlay of the temporal current (black line) and associated charge response (red line) of chronocoulometry experiment using a electrolyte supported MEA operating under 50% H_2 fuel at 800 °C. The potential step displayed is at an overpotential (η) of 1.0 V followed by a second potential step back to E_{ocv}. B) The anode surface temporal temperature response corresponding to the chronocoulometry experiment shown in the left panel. C) Plot of the Q vs η intercepts (Q´) for each time point of the experiment shown in the left panel; the data is restricted to only the first 3 sec of the initial potential step to emphasize the time and magnitude of the Q_{ads} corresponding to the amount of adsorbed fuel. The temporal position of Q_{ads} is also highlighted in A) and B) for clarity.

CO (%)	H_2 (%)	E_{ocv} (V)	I_{max} (A cm^{-2})	P_{max} (W cm^{-2})	Q_{ads} (mC)	α_H†	α_{CO}††
0	50	1.05	0.77	0.192	11.1	--	--
25	50	1.06	0.74	0.187	4.80	0.43	0.57
5	45	1.03	0.74	0.181	5.50	0.50	0.50
25	25	1.03	0.69	0.768	6.50	0.59	0.41

† fraction of the total electrochemically active sites occupied by H(s) (*Vide infra.)*

†† fraction of the total electrochemically active sites occupied by either CO or C^* (*Vide infra.)*

Table 3 Electrochemical data obtained at 800 °C under different fuel compositions in the absence of H2S. Error values are ≤ 10%.

In the presence of 25% CO, where the amount of H_2 is maintained at 50%, Q_{ads} is observed to be ~ 5 mC. This value is less than the ~11 mC that is observed under H_2 alone (Figure 28, Table 3). In addition, Q_{ads} is observed at earlier times (by ~ 0.5 sec) compared to operation with H_2 only. This effect could arise from one or more of several causes

including sluggish electrochemical oxidation kinetics of CO adsorbed to the TPB, and/or carbon formation along the TPB that covers Ni and renders the anode less catalytically active. For reasons discussed below, we believe the latter is the more plausible explanation. In addition, if the majority of charge measured in a chronocoulometry experiment comes from more easily oxidized adsorbed hydrogen, the blocking of some sites by CO or C^* allows less hydrogen adsorption leading to faster consumption. Subsequent experiments using H_2S, described below, support the notion that either CO or C^* serve as blocking agents.

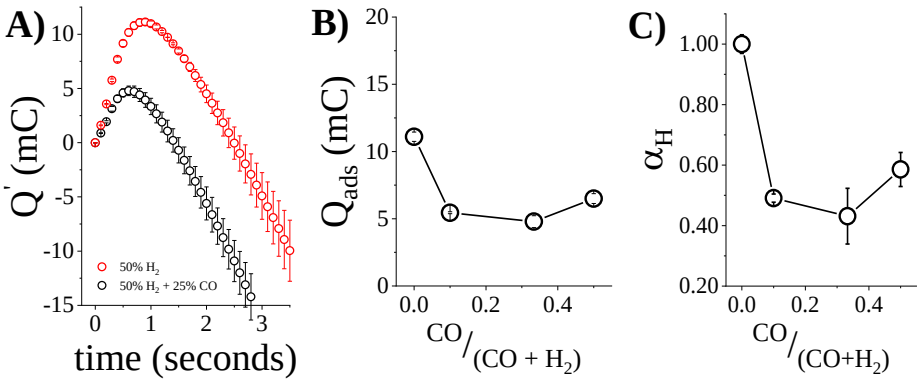

Figure 28. A) Plot of the Q vs η intercepts (Q´) for each time point of experiments under 50% H_2 (black) and syngas containing 50% H_2 + 25% CO, both at 800 °C. B) Q_{ads} and C) anode surface coverage (α_H) by H as a function of the amount of CO present relative to the total fuel content in the syngas.

The relative anode electroactive surface coverage by CO in the syngas fuels can be estimated by adding an additional term for CO coverage to the definition of Q_{ads} assuming CO is electrochemically oxidized and contributes to the charge measured in a chronocoulometry experiment,

$$Q_{ads,syn} = n_H F A \Gamma_H + n_{CO} F A \Gamma_{CO} \tag{24}$$

Assuming that the total number of electrochemically active sites at the TPB does not change between syngas and H_2-alone ($\Gamma_{tot,H}$) [94] Equation 24 can be re-written as

$$Q_{ads,syn} = \alpha_H n_H FA\Gamma_{tot,H} + (1 - \alpha_H) n_{CO} FA\Gamma_{tot,H} \quad (25)$$

where α_H is the fraction ($0 \leq \alpha_H \leq 1$) of the total electrochemically active sites, $\Gamma_{tot,H}$. If $n_H = 1$ and $n_{CO} = 2$ for the oxidations of H and CO, respectively, then rearranging Equation 25 and solving for α_H yields

$$\alpha_H = 2 - \frac{Q_{ads,syn}}{Q_{ads,H}} \quad (26)$$

where $Q_{ads,H}$ is substituted in for the product $FA\Gamma_{tot,H}$ (Equation 25) and is the charge obtained under 50% H_2 (Table 3). If $Q_{ads,syn}$ has contributions from H and CO oxidation, then at all potential values of α_H, $Q_{ads,syn}$ is predicted to be larger than $Q_{ads,H}$. This prediction, however, is not supported by the results. Moreover, values obtained from Equation 26 using the Q_{ads} data shown in Table 3 resulted in unreasonable values for α_H ($\alpha_H > 1$ for all syngas mixtures).

If, on the other hand, CO *is not* electrochemically oxidized on the timescale of a chronocoulometry experiment, then the second term in Equations 24 and 25 is effectively zero and Equation 26 reduces to

$$\alpha_H = \frac{Q_{ads,syn}}{Q_{ads,H}} \quad (27)$$

This resulted in more reasonable values for α_H, ranging between 0.4 and 0.6, with no apparent dependence on the CO content (Figure 28). The decrease in Q_{ads} observed under syngas compared to H_2 alone is likely due to slower, or lack of, electrochemical CO oxidation on the timescale of the chronocoulometry experiment, as suggested by

Equation 27. An alternate explanation is that formation of C^* on the anode surface blocks active sites restricting access to both H and CO. This scenario would require that the electrochemical oxidation of C* occur much more slowly than H, or that C^* is removed by gasification by electrochemically formed H_2O and not through electrochemical oxidation. The latter is plausible since the gasification of C^* is not expected to contribute to the $Q_{ads,syn}$.

Based on the data reported in Table 3, at early times after cell polarization CO does not appear to play a significant role in power generation for CO/H_2 ratios up to 1. In fact, CO appears to *inhibit* electrochemical oxidation and power generation. Additionally, α_H is on average slightly larger than α_{CO} (where $\alpha_{CO} = 1 - \alpha_H$) indicating a larger affinity of the surface towards H_2 over CO up to the CO/H_2 ratio of 1 probed here. We should note that the term α_{CO} cannot distinguish between sites occupied by CO or C^*. The lack of a concentration dependence of H_2 or CO on the Q_{ads} suggests that the consumption of fuel is not diffusion limited but is, rather, charge-transfer limited at the electrode-electrolyte TPB. In Figure 27b, ΔT_{Qads}, which corresponds to the maximum in Figure 27c, is positive as has been previously observed for the electrochemical oxidation of H_2 [93, 120, 122] and depends on the applied overpotential (Figures 27 and 29). At larger overpotentials, there is a nonlinear dependence of ΔT_{eq} on η (Figure 29), ΔT_{eq} corresponds to the maximum in Figure 27b, and is attributed to additional heating from applying large overpotentials in rapid succession.[94, 122] In the region of P_{max} (η ~ 600 mV) ΔT_{Qads} and ΔT_{eq} are within statistical error of each other with a magnitude (ΔT ~ 3.4 °C). This value of ΔT is more than twice the equilibrium value observed in previous chronopotentiometric results (after 5-10 min of applied bias) on anode-supported MEAs at a bias of $^1/_2$ I_{max} (near P_{max}) under H_2 (ΔT ~ 1.1 °C).[120]

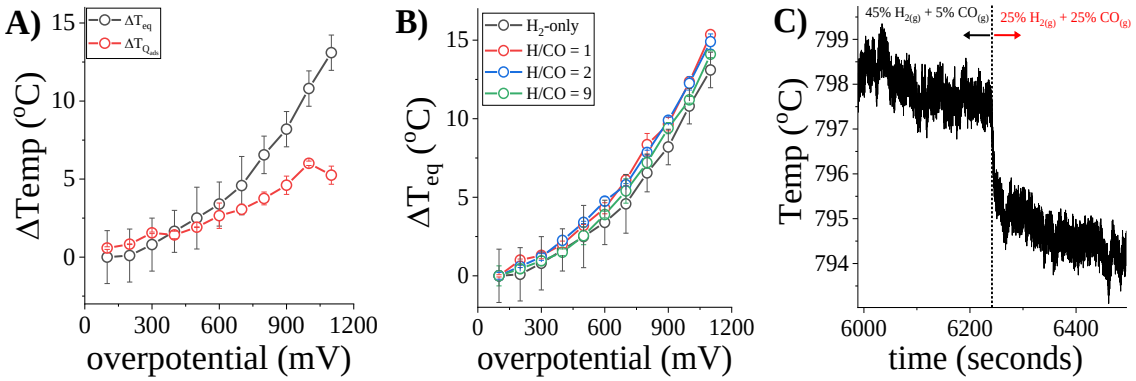

Figure 29 A) Comparison of the difference in anode surface temperature upon polarization at a given η and at E_{ocv} (ΔT) at t = 0.8 sec and t = 10 sec corresponding to ΔT_{Qads} (red) and ΔT_{eq} along the first potential step of the chronocoulometric experiments as a function of overpotential under 50% H_2. B) Comparison of the ΔT_{eq} for 50%-H_2 (black) and the syngas fuel mixtures probed: 25% H_2 + 25% CO (red), 50% H_2 + 25% CO (blue), and 45% H_2 + 5% CO (green). C) Temporal profile of the anode surface temperature near the current collector upon decreasing the H_2/CO ratio from 9 to 1. Operational temperature was 800°C.

The ΔT_{eq} for syngas is similar to that observed when operating under H_2. Under syngas, the ΔT_{eq} is between 2.6 °C to 3.4 °C at P_{max} ($\eta \sim 500$ mV, shown in Figure 29a). These results differ somewhat from what has been observed with anode-supported MEAs operating under syngas for longer times with an applied galvanostatic bias near P_{max}.[120] That report showed temperature changes at similar overpotentials to be 0.5-1.5 °C at H_2/CO ratios between 0.33 and 3. The ΔT results observed in the current work with syngas are within statistical error of those observed under just H_2 (Figure 29b). The small differences in ΔT between H_2 and syngas using chronocoulometry implies similar early-time processes occurring at the anode on the timescale probed. This conclusion would suggest that, under the syngas fuel mixtures used here, adsorbed H is likely the primary, if not the only, fuel consumed at early times.

The effect of H_2S on syngas fuel utilization.

We previously reported the effects of H_2S on H_2 fuels investigated by chronocoulometry. [94, 122] In short, chronocoulometry data showed an unexpected excess of charge generated when small amounts of sulfur (as H_2S) were added to the incident fuel feed. This finding, together with empirical modeling, supported a mechanism where S adsorbed to the TPB is electrochemically oxidized, even at low applied overpotential, and contributes to the overall Q_{ads}.

Figure 30 displays the results obtained for a chronocoulometry experiment at an overpotential step of η = 1.0 V under a syngas mixture of 25% H_2 + 25% CO in the absence and in the presence of 50 ppm(v) H_2S. The Q_{ads} is observed to shift to longer times in the presence of 50 ppm(v) H_2S suggesting that adsorption of S results in a small increase in the charge transfer resistance at the MEA. In addition to the temporal shift of Q_{ads}, the presence of the H_2S increases the magnitude of Q_{ads} from 6.5 mC to 8.9 mC (Table 4). Similar trends are observed under a second, syngas fuel composition of 45% H_2 + 5% CO (with 50 ppm(v) H_2S). The values obtained for Q_{ads} under the syngas mixtures rose ~35-60% when H_2S was present.

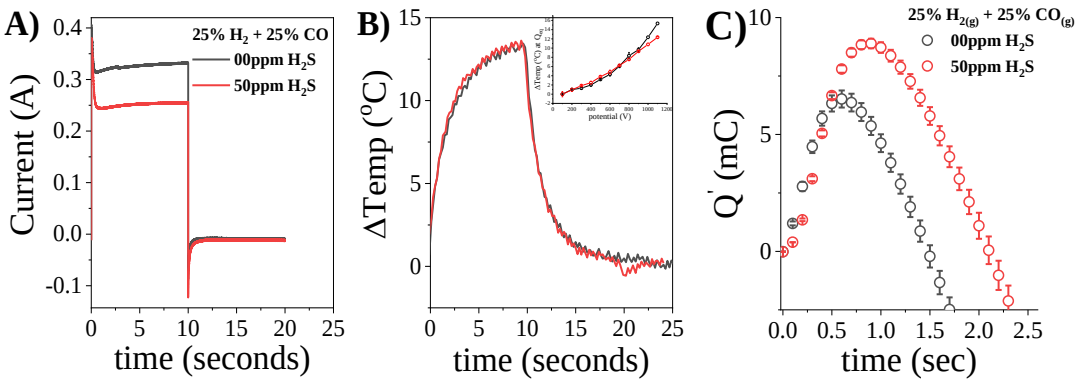

Figure 30 (A) Current measured during a chronocoulometry experiment under syngas containing 25% H_2 + 25% CO without (black) and with (red) 50 ppm(v) H_2S at 800 °C. The potential step displayed is at an overpotential (η) of 1.0 V followed by a second potential step back to E_{ocv}. (B) The anode surface temporal temperature response corresponding to the chronocoulometry experiment shown in A) (same color scheme as A)). The inset displays the ΔT_{eq} as a function of η in the absence (black) and presence of (red) 50ppm(v) H_2S. (C) Plot of the Q vs η intercepts (Q´) for each time point of the experiments (same color scheme as A)).

We treat the data collected in the presence of H_2S following an approach similar to the one used for H_2S-free syngas to quantify the magnitude of α_H in order to understand how adsorption and dissociation of H_2S on the surface of the anode affects fuel oxidation. This approach suggests that 1) S occupies active sites formerly occupied by either H, CO, or C^*, and 2) S is electrochemically active and compensates for the loss of charge transfer reactions from CO adsorption or C^* formation at the TPB. The competitive inhibition of H_2 adsorption by S followed by its $4e^-$ electrochemical oxidation to SO_2 has been shown to occur when operating under H_2 in the presence of H_2S.[122] In the present case, the expression for α_H is similar to Equation 27 where the $Q_{ads,syn}$ term in the numerator on the right hand side of the Equation is replaced with $Q_{ads,syn+H2S}$. That is, if the α_H obtained under syngas in the absence of H_2S represents the upper bound in the number of available H sites then

$$Q_{ads,S} = \alpha'_{H,S} n_H Q_{ads,syn} + \left(1 - \alpha'_{H,S}\right) n_S Q_{ads,syn} \qquad (28)$$

and

$$\alpha'_{H,S} = \frac{4}{3} - \left(\frac{1}{3}\right)\left(\frac{Q_{ads,S}}{Q_{ads,syn}}\right) \quad (29)$$

where $Q_{ads,S}$ is the charge harvested due to the surface adsorbed species present under syngas in the presence of H_2S and $\alpha'_{H,S}$ is the fraction of electrochemically active sites occupied by H under syngas in the presence of H_2S relative to that without H_2S. In this way we obtained values for $\alpha'_{H,S}$ ranging between 0.8 and 0.9 for syngas mixtures with 50 ppm(v) H_2S (Table 4) indicating that the fractional occupation of electroactive sites by H is reduced by sulfur adsorption. The fractional population of the total electroactive sites by H is then the product $(\alpha'_{H,S})(\alpha_H)$ so that in the presence of H_2S, the fraction of electrochemically active sites occupied by H before polarization decreases to values between 0.4 and 0.5 under contaminated syngas mixtures. This finding is consistent with results obtained under H_2 fuels [94, 122] where data showed that adsorption of S decreased the number of H present at the anode. The slight increase in anode surface temperature is consistent with the exothermic oxidation of adsorbed S.

CO (%)	**H_2 (%)**	**E_{ocv} (V)**	**I_{max} (A cm^{-2})**	**P_{max} (W cm^{-2})**	**Q_{ads} (mC)**	**α_H'**	**($\alpha_{H,S}'$) (α_H)†**
5	45	1.05	0.215	0.052	8.36	0.82	0.40
25	25	1.03	0.194	0.045	8.89	0.88	0.51

† **values for α_H obtained from Table 3**

Table 4. Electrochemical data obtained under syngas fuels at 800 °C in the presence of 50 ppm(v) H_2S. Error values are ≤ 10%.

$$S + O_2 \rightarrow SO_2 \quad (30)$$

ΔH = -297 kJ mol^{-1}

In Equation 30, the reaction enthalpy was estimated by Hess's Law using values for the standard enthalpies of formations found in the CRC Handbook of Chemistry and Physics 95th edition.[131]

Unfortunately, Equations 28 and 29 cannot quantify the effect of H_2S on the number of electroactive sites occupied by CO or C*. However, from the trends obtained for α_{CO} in the absence of H_2S we have estimated an approximate ~ 20% decrease in the number of CO or C* present at the anode surface in the presence of 50 ppm(v) H_2S. This assumes that the values obtained for α'_{CO} (which are simply 1-α'_H) correspond to the fraction of the original α_{CO} still occupied by CO or C* after displacement by S. A generalized mechanism is therefore proposed for the utilization of H_2 and CO in syngas fuels in the absence and presence of H_2S that allows for both models/pathways described above (Figure 31). In this mechanism, adsorbed H_2 acts as the dominant fuel upon initial polarization. CO acts to block electroactive sites at the TPB, or form carbon deposits at these same sites by the reverse Boudouard reaction, contributing little to the overall power. In the presence of H_2S, sulfur adsorption at the TPB 1) blocks H_2 from adsorbing to electroactive sites, 2) blocks and/or replaces CO or C* from electroactive sites, and 3) contributes to the Q_{ads} via electrochemical oxidation to form SO_2.

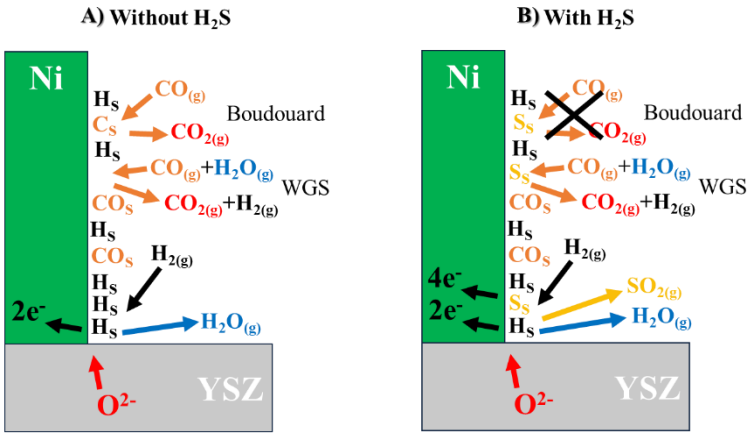

Figure 31 Proposed mechanisms of syngas utilization under polarization in the absence (left) and presence (right) of H_2S. A) In the absence of of H_2S, CO present in the fuel stream results in formation of C via the Boudouard reaction; adsorbed H is the dominant source of power. B) In the presence of H_2S, S blocks H adsorption sites and, presumably, CO/C adsorption sites.

Conclusions

Chronocoulometry is employed to quantify the differences in adsorbed H_2 and syngas fuel coverage and consumption at a Ni-YSZ electrolyte-supported MEA. The effect of the sulfur-containing contaminant, H_2S, on the coverage and consumption of fuels at the anode is also quantified. The electrochemical oxidation of H appears to be the dominant power generating process at early times under syngas operation. Adsorbed CO likely does not participate in early power generation from adsorbed fuel on the electrode surface. This suggests that, on these timescales, the role of CO present in the syngas is likely to form carbon deposits on the surface of the anode. These deposits probably block electrochemically active sites on the anode, decreasing the surface coverage by H and participating in the WGS reaction which can regenerate H_2 to be reused as fuel at the anode. The fraction of electrochemically active sites occupied by H in syngas ranges from 40% to

60% with no discernable dependence on the concentration of H. In the presence of H_2S the population of electrochemically active sites occupied by H decreases by ~ 30%, presumably from competitive adsorption by S. By extension, it is believed that adsorption of S also decreases the amount of CO and/or C^* present at the anode by ~ 20%. The data also suggest that S adsorbed at or near the TPB is oxidized, presumably by the four-electron reaction to produce SO_2.

Acknowledgments

The authors gratefully acknowledge support for this work from the Office of Naval Research (N00014-17-1-2808 and N0001420WX01034).

CHAPTER FIVE

MECHANISTIC INSIGHT INTO CARBON REMOVAL FROM SOLID OXIDE FUEL CELLS VIA OPERANDO STUDIES.

Contribution of Authors and Co-Authors

Manuscript in Chapter 5

Author: Elias D. Pomeroy

Contributions: Conceptualization, methodology, data analysis, writing-original draft, review and editing

Co-Author: William A. Maza

Contributions: Conceptualization, methodology, data collection, writing-review and editing

Co-Author: Daniel A Steinhurst

Contributions: Data collection, writing-review and editing

Co-Author: Stansilav Tsoi

Contributions: Conceptualization, writing-review and editing

Co-Author: John Kirtley

Contributions: Conceptualization, methodology, writing-review and editing

Co-Author: Bryan C. Eigenbrodt

Contributions: Conceptualization, methodology, writing-review and editing

Contribution of Authors and Co-Authors Continued

Co-Author: Jeffrey C. Owrutsky

Contributions: Supervision, funding acquisition, writing-review & editing

Co-Author: Robert A. Walker

Contributions: Supervision, funding acquisition, writing-review & editing

Manuscript Information

Elias D. Pomeroy, William A. Maza, Daniel A. Steinhurst, Stanislav Tsoi, John Kirtley, Bryan C. Eigenbrodt, Jeffery C. Owrutsky, and Robert A. Walker.

Journal of Physical Chemistry, C

Status of Manuscript:
_x__ Prepared for submission to a peer-reviewed journal
____ Officially submitted to a peer-reviewed journal
____ Accepted by a peer-reviewed journal
____ Published in a peer-reviewed journal

MECHANISTIC INSIGHT INTO CARBON REMOVAL FROM SOLID OXIDE FUEL CELLS VIA OPERANDO STUDIES

Elias D. Pomeroy[a], William A. Maza[b], Daniel A. Steinhurst[c], Stanislav Tsoi[b], John D. Kirtley[d], Bryan C. Eigenbrodt[e], Jeffery C. Owrutsky[b], and Robert A. Walker[a,f].

[a] Department of Chemistry and Biochemistry, Montana State University, Bozeman, MT 59717, USA

[b] Chemistry Division, Naval Research Laboratory, Washington, DC 20375, USA

c Nova Research, Inc., Alexandria, VA 22308

[d] Chemistry and Geochemistry Department, Montana Technological University, Butte, MT 59701, USA

[e] Department of Chemistry, Villanova University, Villanova, PA 19085, USA

[f] Montana Materials Science Program, Montana State University, Bozeman, MT 59717

Abstract

Graphitic carbon formation remains the primary degradation mechanism for solid oxide fuel cells (SOFCs) operating on carbon containing fuels, and processes for the remediation of carbon induced degradation remains an important topic of study. The mechanisms for the remediation of carbon induced degradation via electrochemical gasification and gasification using molecular oxygen and steam was studied using combined *operando* optical and electrochemical techniques, including Near Infrared Thermal Imaging (NIRTI), Fourier Transform Infrared Emission Spectroscopy (FTIRES), chronoamperometry/chronopotentiometry (CA/CP), and mass spectrometry (MS). Carbon

removal was determined to follow a stepwise mechanism, first oxidizing surface carbon to CO, and then subsequently to CO_2. CO oxidation was found to require a catalytic surface in order to proceed. CO_2 formed via this mechanism also played a key role in removing graphitic carbon (C) via reverse Boudouard chemistry. NIRTI revealed spatially heterogenous chemistry which gave mechanistic insight into the C removal process, including elucidating the role of surface oxygen species. These species are formed from dissociative adsorption and non-faradaic oxide flux through the electrolyte, as well as O_2 transport limited processes occurring due to high O_2 utilization. C removal from electrochemical oxidation and steam appeared to be more global spatially than from O_2, in part due to the surface species involved in the former, and the transport limitations of the latter. O_2 also appeared to leave C remaining within the cell, despite electrochemical measurement results indicating the contrary. Taken together these experiments significantly develop the mechanisms responsible for remediation of graphitic C induced degradation on operating SOFCs and highlight the importance of spatially resolved techniques to study the entire cell simultaneously to account for spatially heterogenous chemistries occurring therein.

Introduction

Human activity continues to add increasing amounts of CO_2 into our atmosphere as global energy demand concurrently increases.[132] In the United States, this rising energy demand is accommodated, in part, by growing contributions from renewable resources. However, natural gas consumption has also increased to meet growing demands.[133] The maximum thermal efficiencies of natural gas power plants is typically limited to 55%,

meaning about half of the methane that is burned goes directly to waste heat, rather than usable power.[134] Fuel cells present a more efficient solution for directly converting carbon containing fuels into usable electrical power. The most mature fuel cells are proton exchange membranes fuel cells (PEMFCs). While these devices are efficient and are now used in commercially available vehicles, PEMFCs also require extremely pure H_2 fuel and expensive Pt catalysts for electrochemical operation.[135] Additionally, the need to maintain a hydrated exchange membrane limits fuel transport kinetics, lowers overall electrical efficiencies, and increases plant complexity.[135, 136] A solid oxide fuel cell (SOFC) is an alternative fuel cell that does not suffer from the same limitations as PEMFCs. SOFCs boast fuel flexibility, meaning that these devices can produce electricity from any carbon containing fuel including methane, coal, syn-gas, biogas and even renewable materials such as methanol.[22, 48, 79, 137-139] Together with their very high efficiencies – upwards of 85% with cogeneration of electricity, either with combined heat and power or with an additional gas turbine – SOFCs represent an attractive bridging technology that can utilize existing fuel feedstocks with greater efficiencies today and continue to contribute to power production in a future H_2-based economy.[1, 2, 140] In principle, SOFC technology is also reversible and can reduce CO_2 and H_2O to syngas (a mixture of CO and H_2) with high faradaic efficiencies, providing an energy storage mechanism for renewable sources, as well as a feedstock for petrochemicals via Fischer Tropsch synthesis [2, 141]

The benefits of SOFCs, namely their fuel flexibility and high efficiencies, stems from their need to operate at high temperature (600-1000 °C). Conventional SOFC assemblies consist of a solid oxide electrolyte (typically 8% yttria stabilized zirconia

(YSZ), a mixed ion-electron conducting cathode and a Ni-based, ceramic-metallic (cermet) composite anode. Given an activation energy of oxide transport through YSZ of ~100 kJ/mole, SOFCs must operate at elevated temperatures to maintain sufficient current.[4] At these temperatures, Ni is an excellent catalyst for CH bond activation and has been widely used for cracking petrochemicals for decades.[142] Ni cermet anodes do present challenges in SOFCs, however. While they are more tolerant than PEMFCs to gas phase contaminants, Ni-cermet anodes are susceptible to degradation from fuel stream contaminants such as sulfur and chlorine and carbon accumulation (or coking).[31, 69, 71, 74, 143, 144]

Coke diminishes the electrochemically and catalytically active area of the anode, blocks pores, and can even remove Ni from the cell via metal dusting.[19, 79] Ni's tendency for coking has been well known and highly studied with catalytic systems for decades, and the information gained from studying those systems has been used to improve C tolerance in SOFCs.[18, 25, 142, 145-148] For example, C deposition during steam cracking is known to be favored at Ni-grain boundary sites, and C formation can be reduced by altering C-H-O ratios in the inlet gases. [25, 147]Alloying Ni with noble metals, increasing the alkalinity of catalyst support materials, and added oxygen with the addition of CeO_2 in electrolyte materials have all been effective in reducing graphitic C formation in catalytic applications. Many of these strategies have been adapted for SOFCs with some success.[19, 27, 149] Adding reforming agents to the gas stream, typically oxidizers including O_2, steam, and CO_2, can also shift the C-H-O ratios to regimes that make Ni-cermet anodes less susceptible to coking.

SOFCs are more than catalytic systems, however, so any changes to the anode that reduce coking cannot adversely impact electrochemical oxidation and conversion efficiency. Simply alloying Ni with other metals may improve C tolerance, but also decreases electrocatalytic activity.[32] Furthermore, the addition of reforming agents reduces electrical efficiency by lowering the open circuit voltage of the cells, as indicated by the Nernst equation. Additionally, even with these strategies, C formation can still occur on the SOFC anodes, and methods to regenerate SOFC anodes deactivated by C remain an active area of intense research.

Mechanisms responsible for C formation and removal on functional SOFC anodes are difficult to identify, since SOFCs operate at such high temperatures with the additional need for dual atmosphere and polarization control. Coking on functional SOFCs is typically studied with a combination of electrochemical and ex situ experiments, where the cell's performance under a set condition is monitored with electrochemical measurements, and the cell is subsequently disassembled and analyzed.[18, 26, 27, 150] Observed changes to the cell's microstructure and the presence or absence of coke are then assigned as the cause for the performance changes that were measured electrochemically.[26, 150] An alternative approach studies C formation using SOFC electrode chips in a single atmosphere, with C formation being measured with thermogravimetric analysis (TGA), Temperature Programed Oxidation (TPO), or similar techniques, without the use of concurrent electrochemical measurements.[10, 18, 149] Findings from these and related studies are instructive, but claims about how results can transfer to fully functioning devices are necessarily tentative.

To fully understand coke formation and removal in SOFCs, experiments must be capable of making real-time, direct measurements that report on the chemical condition of an SOFC anode at temperature and in a functioning (dual atmosphere) environment. Advances during the past decade have led to novel optical techniques that can assess the thermal load across an anode surface (Near IR thermal imaging or NIRTI)[53], monitor the gas composition above the anode (FTIR emission spectroscopy or FTIRES)[151], and identify material changes on the anode as a function of fuel identity, temperature and electrochemical load (Raman spectroscopy).[20, 21, 37, 48, 50, 57] When coupled with both voltammetry and impedance measurements, data from these operando optical techniques can be used to develop species and material-specific mechanisms describing electrochemical oxidation and materials degradation that directly reflect the anode's electrochemical condition. For example, previous studies have included monitoring C removal kinetics under gas phase reactants, as well as electrochemical C removal, using Raman spectroscopy, and found that steam was faster than either CO_2 or O_2 in removing C, and O_2 resulted in the greatest amount of performance degradation and microstructural changes.[20, 24, 37]

Findings reported in this work present a complete and comprehensive description of carbon removal from Ni-cermet anodes via several different methods, namely direct electrochemical oxidation, oxidation by O_2(g), and steam gasification. Drawing from simultaneous, operando NIRTI and FTIRES measurements together with independent electrochemical monitoring and mass spectrometric analyses of gas phase exhaust, these studies track the time dependent changes in anode chemistry and correlate these changes

with the SOFC's overall electrochemical capabilities. Findings show that C removal follows a stepwise mechanistic process; first, C is oxidized to CO which is subsequently oxidized to CO_2, though only when a catalytic Ni surface is available. CO_2 generated during C removal also played a key role in further C removal via reverse Boudouard chemistry during all experiments, but especially during electrochemical oxidation. Lastly, spatially heterogenous chemistry also occurred during each experiment, and played a significant role in determining mechanistic insight, including non-faradaic oxide flux occurring during C removal with steam, and sluggish oxygen transport kinetics due to high oxygen consumption rates.

Experimental

Experiments were carried out on button-style, anode supported membrane electrode assemblies (MEAs) purchased from Fuel Cell Materials (https://fuelcellmaterials.com) and consisting of a 25 mm diameter, 400 µm-thick NiO-YSZ anode with 12 µm functional layer, a 25 mm-diameter, 3 µm-thick YSZ electrolyte, a 25 mm-diameter, 3 µm-thick gadolinium-doped ceria (GDC) barrier layer, and a 12.5 mm-diameter, 12 µm-thick lanthanum strontium cobaltite (LSC) cathode. These cells were pasted to an alumina tube using alumina paste to form a gas tight seal between anode and cathode chambers, and the assembly used a sapphire window for optical access. Additional details about the assembly have been reported elsewhere.[21, 50, 57]

The experimental apparatus enables operando studies of SOFCs at temperatures up to 950 °C, using a duplex NIR thermal imaging (NIRTI)/Fourier Transform Infrared Emission Spectroscopy (FTIRES) with coupled electrochemical (voltammetry and EIS)

capabilities and MS analysis of exhaust gas. Thermal images were acquired with a 5 Hz collection rate using a 14-bit, 656 by 492 pixel, CCD camera (Allied Vision Technologies, Stingray F033B ASG). A long pass filter (Hoya R72) with a nominal cut-off of 720 nm was used to remove visible light from the images. FTIRES was performed with an FTIR spectrometer (Mattson Instruments, Inc. Model Number: RS-10000) with acquisition times of ~60 seconds. NIRTI and FTIRES were performed concurrently in a bespoke duplex setup (Figure 32). Electrochemical measurements, chronoamperometry (CA) and chronopotentiometry (CP) were carried out with a Gamry 3000 potentiostat. Gas analysis was performed with a Pfeiffer Thermostar quadrupole mass spectrometer fitted with an ambient pressure inlet (MS). To eliminate effects from gas residence time, MS measurements were shifted temporally, correlated to dramatic electrochemical changes induced by changes to gas composition (i.e. OCV changes subsequent to H_2 introduction), and peaks in FTIRES data. These experiments were performed at 800 °C, under a total gas flow of 100 sccm. Cells were heated overnight to 750 °C at 1 °C/min, where initial NIRTI calibration took place, and then subsequently heated to operational temperature at 1 °C/min, where final NIRTI calibration took place. The MS was calibrated by varying the flow rate of CO, CO_2, and H_2 from 0-100 sccm in the assembly with a YSZ chip in place of the MEA and performing a linear calibration on the measured current at steady state vs partial pressure. All other MS data reports the current as measured by the MS.

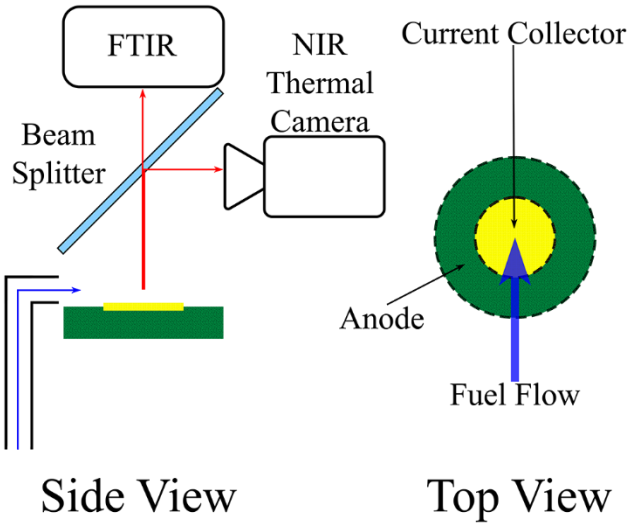

Figure 32 Illustration of the NIRTI and FTIRES duplex apparatus

Since all experiments were carried out with a total flow rate of 100 sccm, values of gas partial pressure will be reported as percentages or as atmospheres (atms), with the balance being Ar. After calibration, the anode was reduced using 20% H_2 for 30 minutes, and then using 50% H_2 for 1 hour. Carbon was deposited on the cell using a 25% methane flow for 10 minutes. The anode headspace was purged with 100% Ar for 10 minutes before oxidants were introduced (at t=0 s). For electrochemical oxidation experiments, the cells were polarized with an 800 mV overpotential (to an approximate cell voltage of 0.4 V). Molecular oxygen was introduced at 3%. Steam was introduced by providing a stoichiometric gas mixture of 6% H_2 and 3% O_2. Kinetics calculations (not included) predict $\geq$ 90% conversion of this mixture to steam within the first 3 ms of exposure to the MEA, and empirical evidence using the MS indicate complete conversion to steam. Consequently, we report results as 6% steam as the putative oxidant/carbon removal agent. During these experiments, CO and CO_2 partial pressures were monitored using FTIRES,

and all other gas phase components were monitored using MS. Thermal changes to the cell were measured using NIRTI, and OCV/current were measured using the potentiostat.

Results and Discussion

Carbon removal by electrochemical oxidation

Data Carbon can be removed from an SOFC anode by a number of oxidizing agents including steam, carbon dioxide, molecular oxygen, and oxide ions transported electrochemically from the cathode to the anode.[20, 30, 35-38] Each strategy for removing carbon has advantages and disadvantages in terms of the speed and efficacy of carbon removal and possible damage done to the anode microstructure from Ni oxidation.[20, 37] Despite well-established, practical strategies for remediating carbon accumulation on SOFC anodes, however, the mechanism(s) responsible for carbon removal remain largely unknown. To identify and evaluate the steps leading to carbon remediation on SOFC anodes, the electrochemical removal of carbon was first analyzed, since this approach enabled the widest variety of operando tools, including NIRTI, FTIRES, mass spectrometry, and electrochemistry.

To clarify how O^{2-} oxidizes C (i.e., coke) in the Ni-YSZ anode, electrochemical experiments began by depositing carbon on the anode by exposing it to dry methane for 10 minutes and then purging the system with Ar and allowing the cell to equilibrate for 10 minutes. Following this preparation, a constant 0.8V applied overpotential was applied to the cell, for a measured cell voltage of 0.4V, and used to define t=0 s for CA, NIRTI, and MS/FTIRES experiments. False color thermal images, seen in Figure 33, show that initially the temperature of the cell surface remains constant and uniform, with slight 0.5-1.5 °C

heating around the current collector (Figure 33-54 and 59 s), until around 495 s (Figure 33-495 s), where some slight cooling can be seen around the current collector). By 1524 s, the region around the current collector shows an apparent dramatic decrease in temperature (Figure 33-1524 s). The cool area expands to roughly the area of the underlying cathode (Figure 33-1623 s) before expanding beyond those bounds at 1693 s (Figure 33-1693 s). The cool area continues to grow (Figure 33-1957 s) until the end of the experiment, when the entire anode appears to have cooled between 6-10 °C (Figure 33-2610s). The NIRTI data do not appear to vary with gas phase composition of any species of interest, nor with the current.

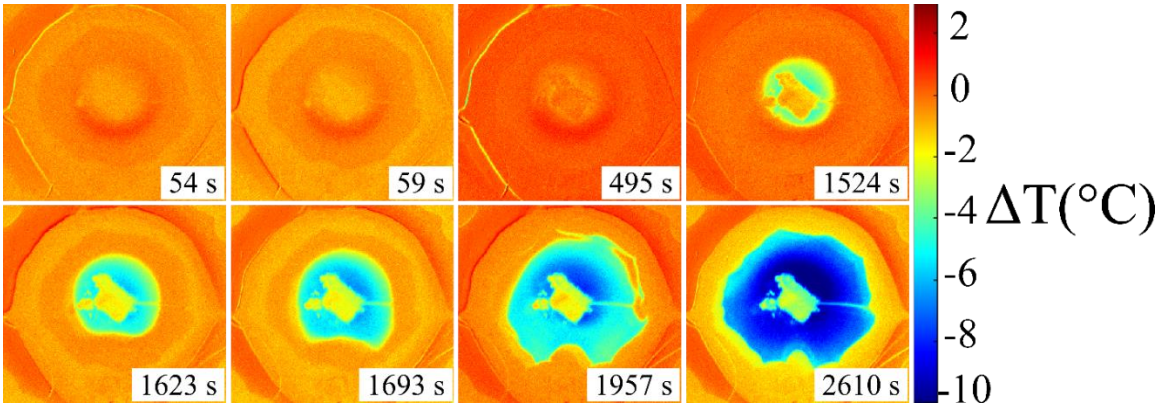

Figure 33 False color NIRTI images from electrochemical oxidation experiment showing change in temperature from initial temperature between 2.5 and -10 °C at relevant times (54 s, 59 s, 495 s, 1524 s, 1624 s, 1693 s, 1957 s, and 2610 s).

The measured cell current, shown in Figure 34a, is proportional to the rate of electrochemical reactions. Inflection points provide clear evidence of multiple mechanisms over the duration of the experiment, and are most clear in the differentiated current vs time plot in Figure SI-1. In Figure 34a, the current starts high, at 253 mA and decreases steeply to 176 mA at 55 s, the first inflection point in the current. The current continues to decrease

rapidly to 130 mA at 93 s, the second inflection point. The current continues to drop to 59.8 mA at the third inflection point (495 s), and then linearly to 19.9 mA at the final inflection point at 1693 s. These inflection points provide clear landmarks to divide the experiment into Periods. The Periods are indicated in Figure 34a as the colored boxes on plots. Period I is defined as the time between 0 and the first inflection point (0-55 s), Period II between the 1st and 2nd (55-93 s), Period III between the 2nd and 3rd (93-495 s), Period IV between the 3rd and 4th (495-1693 s), and Period V the 4th and end (1693-3000 s).

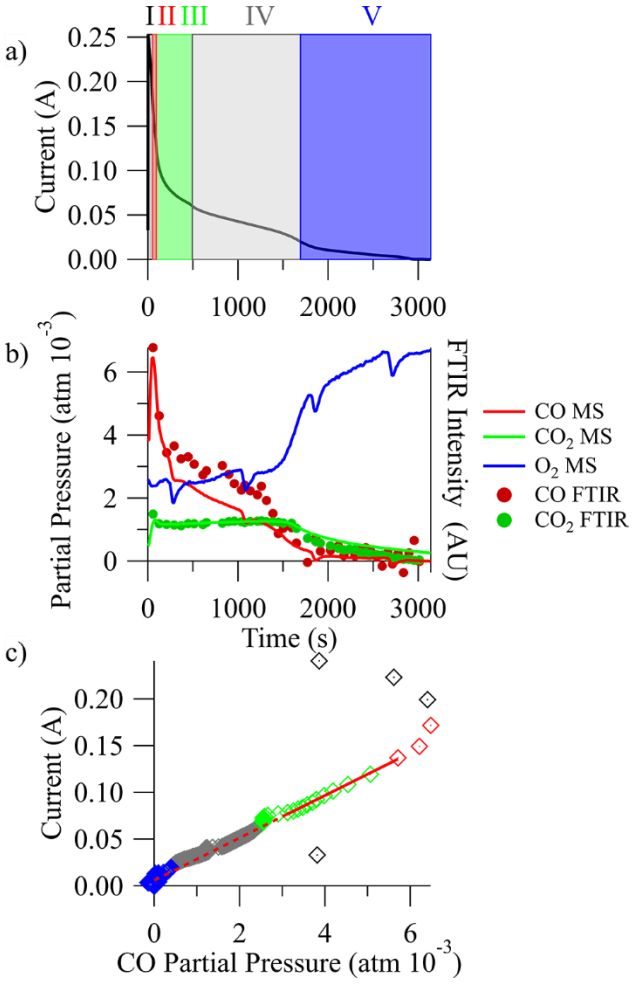

Figure 34 Data collected as part of the electrochemical oxidation experiments with a) CA, b) MS and FTIRES data, and c) Plot of current as a function of P_{CO}, with marker colors to indicate the period during which the data was collected.

The time dependence of the species abundance measured by FTIRES and MS (Figure 34b) are similar, indicating the partial pressures (P_x where x = CO, CO_2, O_2, etc) measured by these methods agree. The MS data also show apparent dips in some (e.g., O_2 and CO) of the gas phase components, most notably for the O_2 (m/z = 32). These dips are semiregular, occurring roughly every 5 minutes, and do so synchronously for the different gases. As a result, we believe these are an instrumental artifact and do not arise from chemical changes occurring in the SOFC. Subsequent to these experiments, the MS filament was replaced, and the phenomena stopped, further supporting that the periodic dips were an instrument artifact. CO is present at the onset of the experiment with sharp rise to a peak value near the end of Period I. The P_{CO} then decreases for the remainder of the experiment, rapidly until just before the end of Period III, then more slowly until it reaches a minimum just after the start of Period V. After 360 s the P_{CO} continues to decrease more slowly to a concentration of 8.0×10^{-4} atm at 1495s. From there, the P_{CO} decreases further to 1.5×10^{-4} atm at 2000 s and does not change for the remainder of the experiment. The initial P_{CO_2} increases to a maximum near the start of Period II. The P_{CO_2} then diminishes slightly after which it remains relatively constant, until just before the end of Period IV. At this point the concentration decreases continuously to near the starting value. Lastly, the MS data for P_{O_2} is not reported in absolute pressures due to gas handling limitations. The P_{O_2} remains constant until the start of Period IV, after which it increased gradually until the same time where P_{CO_2} drops, near the end of Period IV, where the signal increases by roughly 15%.

Interpretation With all these interrelated pieces of data, we can draw some conclusions about the mechanisms responsible for removing C electrochemically from SOFC anodes in the time periods defined above. In Period I (0-55s), the cell begins in a state where we assume that all Ni surfaces are saturated with at least a monolayer of adsorbed C (Figure 35a). This carbon can be divided into three types, which is consistent with other literature reporting on C removal.[18] The first is electrochemically available carbon (EAC), carbon on a Ni surface near the triple phase boundary (TPB) that is connected electronically to the current collector (denoted in Figure 35a). The second type of carbon is easily oxidizable carbon (EOC) that is either not near a TPB or is on an isolated Ni particle not connected to the circuit but accessible to reforming (oxidizing) gases. (denoted with green circular boarders). The third carbon type is termed hard to oxidize carbon (HOC) (denoted with blue rectangular boarder). HOC may be inaccessible, isolated deep in the anode's porous microstructure and/or highly ordered graphite that is less labile than graphite having many grain boundaries or point defects.[18, 20, 93]

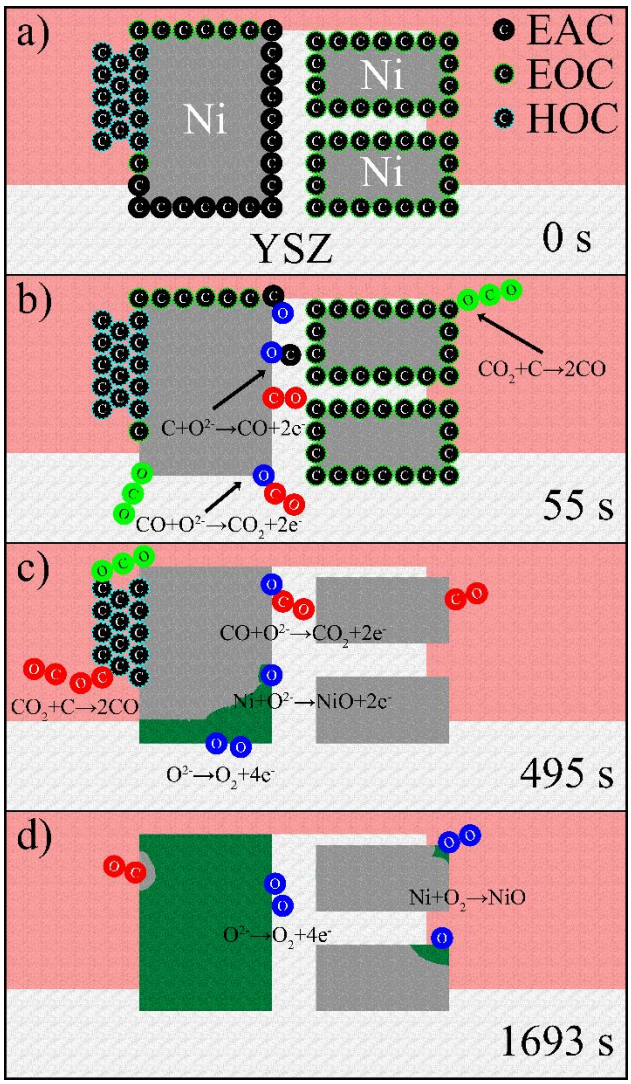

Figure 35 Schematic for the mechanisms responsible for C removal via electrochemical oxidation. a) indicates where EAC (C with no border), EOC (C with green circular border), and HOC (C with blue square border) are located on the cell. b) Chemistry occurring at the transition between Periods I and II, c) Periods III and IV, d) Periods IV and V.

The relevant elementary reactions, including some that can remove carbon from the anode electrochemically, are shown below:

$$C + O^{2-} \rightarrow CO + 2e^- \quad (30)$$

$$C + 2O^{2-} \rightarrow CO_2 + 4e^- \quad (31)$$

$$CO + O^{2-} \rightarrow CO_2 + 2e^- \quad (32)$$

$$2CO \rightleftharpoons CO_2 + C \qquad \Delta H=-172.45^{100} \quad (33)$$

$$2O^{2-} \rightarrow O_2 + 4e^- \quad (34)$$

$$Ni + O^{2-} \rightarrow NiO + 2e^- \quad (35)$$

$$2C + O_2 \rightarrow 2CO \qquad \Delta H=-359.71^{100} \quad (36)$$

$$C + O_2 \rightarrow CO_2 \qquad \Delta H=-393.51^{100} \quad (37)$$

Since the anode remains under Ar atmosphere, the current during Period I must be due to the electrochemical oxidation of EAC (Equation 30 and 31). The rate of carbon oxidation is reflected in the rise in CO detected by MS. Interestingly, the maximum P_{CO} signal precedes the maximum P_{CO_2} signal by ~30 seconds implying that first carbon is oxidized to CO in a single step and the CO product immediately desorbs. Additionally, P_{CO} is the highest as the CA passes through its first inflection point. These two factors taken together point to the primary electrochemical carbon oxidation mechanism as being the two-electron oxidation of C to CO, Equation 30, and with little to no contribution from Equation 31.

At the beginning of Period II (55-96s) a new process becomes the dominant source of electrons measured in the CA response, suggesting that EAC is nearly depleted. This analysis begins by noting that the concentration of CO and current are strongly correlated. This correlation becomes clear by plotting the current (Figure 34a), a rate, vs. P_{CO}, as measured by MS (Figure 34b) and is shown in Figure 34c. A linear regression between data acquired at 86 s and 230 s has an R^2 of 0.997, indicated by the endpoints of the solid red line in Period 3c. During this period neither the current nor the concentration of CO were linear with time, reinforcing the linear correlation between P_{CO} and current which

represents the charge transfer kinetics. Extending this line to the x axis, the dotted line in Figure 34c, shows that this linear correlation between measured current and P_{CO} persists until 1022 s, well into Period IV, after which it begins to underpredict the amount of current generated. This correlation also enables us to express the current (or rate at which electrons are produced) as follows:

$$\frac{de}{dt} \propto i \propto k_3[\mathrm{CO}] \tag{38}$$

These factors point to the dominant electrochemical mechanism occurring during Period II being the electrochemical oxidation of CO to produce CO_2, Equation 32, and the above expression would be consistent with a kinetics expression based on that elementary reaction. At the start of Period II, the cell's condition would be in a state similar to the one shown schematically in Figure 35b, where nearly all of the electrochemically available C has been oxidized to form CO and the cell is beginning to operate on CO as fuel.

At the beginning of Period III (93s to 495s) an additional inflection point occurs indicative of different mechanisms predominantly driving the current. The cell is still operating on CO as fuel, as evidenced by the linear correlation between P_{CO} and current, the likely origin of that CO is EOC. Concurrently, P_{CO_2}, instead of closely following P_{CO}, decreases slightly and then remains constant. We propose that even as CO_2 is produced (through electrochemical CO oxidation), it is also consumed in an unidentified reversible process. The most likely process is the reverse Boudouard Equation, Equation 33, given the favorable conditions of locally high P_{CO_2} and high temperature (>730˚C).[100, 137] If the reverse Boudouard reaction is important, then CO_2 acts as an oxidizing agent, reacting with EOC (Figure 35b) resulting in the formation of two equivalents of CO (Figure 35b) which

can, themselves, be oxidized. This conclusion is further evidenced by plotting the current as a function of $t^{-1/2}$, see Figure SI-2. A linear region clearly appears shortly after the start of Period III, and continues until just before the start of Period IV, which is indicative of a transport limited process. Collectively, this points to the reverse Boudouard reaction determining kinetics during Period III.

The direct dependence of current on P_{CO}, as well as the steady-state P_{CO_2} well into Period IV imply CO oxidation and reverse Boudouard chemistry occur at rates that preserve the relationship established in Equation 38 and the approximately steady P_{CO_2} concentration. The electrochemistry, however, indicates that the majority of current is created by a new process which implies that the EOC is completely consumed by the end of Period III, making HOC the ultimate the origin of C containing exhaust gases. Throughout most of Period IV the concentration of oxygen slowly increases, providing clues to the identity of the fuel being oxidized in Period IV. Given earlier studies that correlated electrochemical behavior with carbon oxidation, we expect that the major current source is Ni oxidation.[20] At the beginning of this period, the condition of the cell is represented schematically in Figure 34c. At this time, the cell's EOC is fully converted to CO and the diminishing amount of CO is adsorbed to the TPB. In the limit of growing regions that are fuel starved, O^{2-} electrochemically oxidizes Ni forming NiO. In addition, as more Ni at the TPB is irreversibly converted to insulating NiO, small amounts of O_2 are subsequently produced. Molecular oxygen can oxidize and consume available gas phase and adsorbed CO, though more likely the latter, given the results found in later sections. HOC can react with slowly diminishing amount of CO_2, creating additional CO that can

still be electrochemically oxidized. Around 1500s, there is a precipitous drop in the P_{CO_2}, a quick rise in the P_{O_2}, and an apparent cooling of the cell in the region near the current collector. The apparent cooling is attributed to the formation of NiO. The precise mechanism by which NiO formation leads to cooling is unknown, as NiO has a higher emissivity than a polished Ni surface.[152] However, the emissivity of Ni foams, not an unreasonable comparison to the Ni-YSZ cermet, can have emissivity near that of NiO with sufficiently high porosity.[153] As the porosity of the Ni foam decreases, so too does the emissivity.[153] As NiO forms, it takes up more space than the Ni metal, closing the pores that formed during initial conditioning of the cell, leading to a smoother, and therefore less emissive, surface. The decrease in emissivity from decreased porosity competes with the increased emissivity from NiO, resulting in a total decrease in emissivity of about 1%, which appears as about 10 °C cooling from the equilibrium temperature. The formation of NiO at the end of these experiments is further supported by studies using spectrochronopotentiometry, where Raman directly associated the formation of NiO with the consumption of the HOC.[20, 154]

By the start of Period V, the current reaches its final inflection point, and the cell appears as seen in Figure 35d. Here, all HOC has been converted to CO, which is quickly oxidized by O_2 to CO_2. The electrically accessible Ni is fully converted to NiO, resulting in the formation of O_2. Since all electrochemically available fuel, including Ni, must be consumed at this point, the cell serves solely as an O_2 pump. Gas phase O_2 formed at the anode then oxidizes isolated Ni and any remaining CO. The apparent drop in temperature extends beyond the area adjacent to the current collector (isolated Ni), until the entire

surface of the anode has apparently cooled. P_{O_2} tapers off as the applied potential is producing as much O_2 as it can. The P_{CO_2} continues to slowly decrease to 0 as any CO_2 diffuses out of the electrode and any remaining HOC is oxidized by gas phase O_2.

Carbon removal with molecular oxygen

Data Molecular oxygen can also be used to remediate graphitic carbon induced degradation. Previous studies report that O_2 removes carbon from Ni cermet anodes more slowly and with greater microstructural damage than steam.[37] However, carbon gasification with O_2 is both effective and a chemically simpler system to characterize, so this strategy for carbon remediation will be examined next. Like the experiments discussed above, O_2 oxidation experiments began by depositing carbon on the anode by exposing it to dry methane for 10 minutes and then purging the system with Ar and allowing the cell to equilibrate for 10 minutes. Following this preparation, a 3 % O_2 in Ar mixture was introduced and used to define t=0 s for the NIRTI, CP at open circuit (OCV), and MS/FTIRES experiments.

In contrast to the electrochemical oxidation results, experiments performed with molecular oxygen lack clear inflection points to differentiate mechanistic regimes. Instead, NIRTI, Figure 36, suggests three distinct periods of different chemistry occurring in the cell. For clarity, all changes in temperature are referenced to the initial equilibrium temperature. The first Period, Period I, occurs from 0 s to around 170 s. The surface temperature during this period remains relatively constant (Figure 36-73 and 117 s). Period II begins at approximately 170 s upon the appearance of local heating near the fuel inlet (Figure 36-167 s), increasing the temperature there by about 3 °C. Interestingly, the half

of the cell opposite the fuel inlet appears to cool initially by about 2 °C during the same time interval. The local heating by the inlet continues to increase (by approximately 10 ˚C, see Figure 36-236 s) and spreads to cover more surface area of the cell over the next 150 s (until Figure-5 331 s). A thermal wave moves across the cell during this interval (Figure 36-273 and 291 s). This wave is most apparent at 291 s, where there is a region of slightly lower temperature between the ~5 °C area in the center of the cell and the ~5 °C line across the cell, see SI-Figure 3 for a higher resolution image. Period III starts at 330s (Figure 36-331 s), during which the cell remains warm, but gradually cools (Figure 36-387, 415, 594, 683, and 831 s), with apparent cooling originating from the outer edges of the cell and continuing to the center, until the entire cell has cooled ~4 °C (Figure 36-831 s).

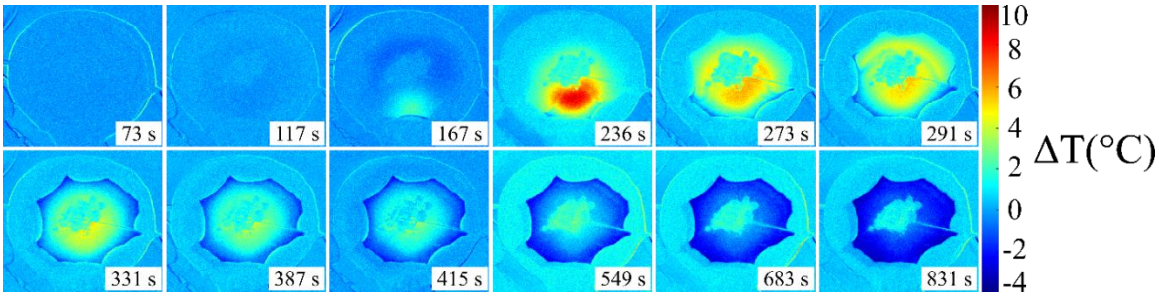

Figure 36 False color NIRTI images from C removal with oxygen experiment showing change in temperature from initial temperature between 10 and -4 °C at relevant times (73 s, 117 s, 167 s, 236 s, 273 s, 291 s, 331s, 387 s, 415 s, 549 s, 683 s, and 831 s)

CP, Figure 37a, shows the cell's potential remaining at its equilibrium OCV, -1.25 V, during the first half of Period I, until around 60s, where it gradually increases to -1.18 V at 101 s. During the second half of Period I, the potential plateaus for about 50s, increasing more gradually to -1.16 at 150 s. At the start of Period II (170 seconds), the potential increases steeply to -0.69 V. The potential remains there during Period III, until around 750s where it begins to sharply increase again. The measured potential contains

information about the changing chemical composition of reactants and products that can be deduced from the Nernst potential of various species (CO, CO_2, O_2, Ni) across the entire anode surface. The spatially heterogeneous reactions inferred from the NIRTI experiments are likely not well differentiated by the CP, making differentiating between periods from electrochemical data challenging.

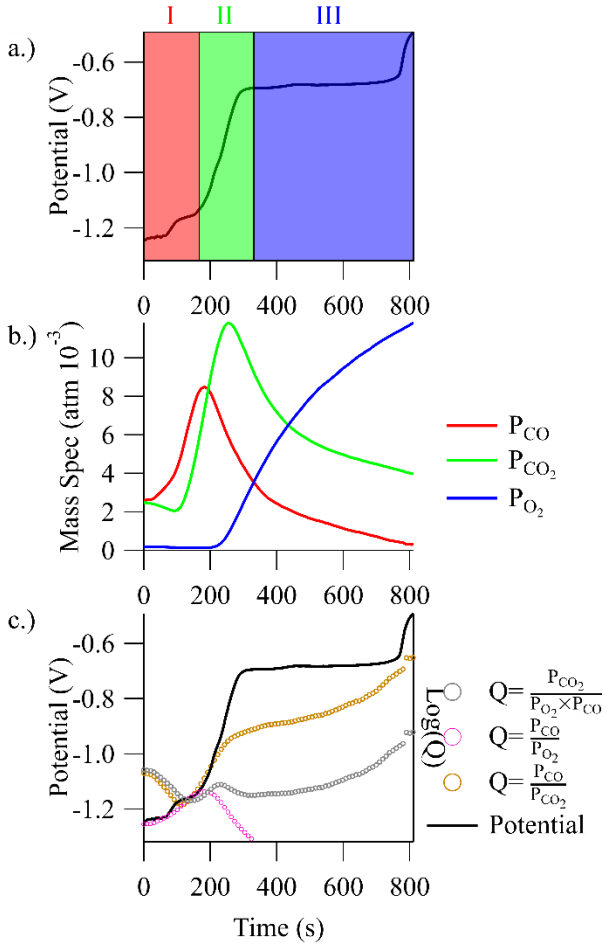

Figure 37 Data collected as part of the molecular oxygen experiments with a) CP, b) MS and c) Plot of OCV with the logarithm of relevant reaction quotients for Equations 39, 36, and 33, respectively.

The MS data, Figure 37b, are of the exhaust stream composition and therefore a global measurement (reflecting no spatial information). FTIRES measurements correlated

quite closely to measured MS values, and are not included in the figure for clarity, but can be found in SI-Figure 4. During Period I, P_{CO} begins to rise sharply, peaking near the transition between Period I and Period II. P_{CO} then monotonically decreases. P_{CO_2} decreases slightly during the first half of Period I, then increases, eventually eclipsing P_{CO}. P_{CO_2} reaches its maximum near the midpoint of Period II and then decreases monotonically. P_{O_2} remains constant and very low until ~180 second (in Period II) when it begins to monotonically increase.

Interpretation As with electrochemical oxidation, carbon removal with molecular oxygen can be related to a series of elementary reactions that include direct oxidation and Boudouard chemistry. The relevant elementary reactions, including removal of C by O_2 are:

$$2CO \rightleftharpoons CO_2 + C \qquad \Delta H=-172.45^{100} \qquad (33)$$

$$2C + O_2 \rightarrow 2CO \qquad \Delta H=-110.53^{100} \qquad (36)$$

$$C + O_2 \rightarrow CO_2 \qquad \Delta H=-393.51^{100} \qquad (37)$$

$$2CO + O_2 \rightarrow 2CO_2 \qquad \Delta H=-282.98^{100} \qquad (39)$$

$$2Ni + O_2 \rightarrow 2NiO \qquad \Delta H=-479.4^{155} \qquad (40)$$

Equation 40 is included to acknowledge that O_2 can react with the anode as well as any deposited carbon. To determine those Equations most responsible for processes occurring during Period I, we consider the relevant reaction quotients (Q) as a function of time for some of the above elementary steps. Specifically, we note that the logarithm (log) of these reaction quotients should be proportional to the OCV, and many of these reaction quotients can be approximated using the MS data shown in Figure 37b. The log(Q) of Equations 33

(in reverse), 36, and 39 are plotted in Figure 37c along with the CP data. From Figure 37a log(Q) for both Equation 39 and the reverse of Equation 33 show an opposite trend to that seen in the potential during the first half of Period I. Only Equation 36 appears to match the trend observed in the potential, indicating that Equation 36 is the dominant reaction during the first half of this Period. If Equation 36 is dominant in the early stages of carbon oxidation, then this reaction is either insufficiently exothermic (ΔH=-110 kJ/mol) or too kinetically limited to produce enough heat to alter the observed cell temperature. Additionally, until the observed rise in potential around 60 s, the electrode appears to be insensitive to changes in partial pressure of the product gases. Complete carbon coverage of the anode at early times, thereby forming a blocking layer on the electrode, could explain the limited potential response to changes in gas phase components and apparent steady temperature of the anode surface after the introduction of O_2. A sufficient erosion of the blocking layer, thereby exposing Ni to the headspace and sensitizing the anode to reactant partial pressure explains that rise in potential. The plots of log(Q) during the plateau all share a similar shape to the potential during the second half of Period I, implying that some combination of Equation 33, 36, and 39 all playing a role in the chemistry during this time.

Simultaneously to the OCV plateau, the P_{CO_2} begins to increase, further supporting Equation 33 and 39 playing a role in the chemistry observed during the second half of Period I. The timing of P_{CO_2}'s rise and the sensitization of the anode to gas phase components could indicate a catalytic requirement for Equation 39, indicating the reaction is proceeding heterogeneously on the electrode as opposed to homogenously in the gas phase, and supports the hypothesis regarding the blocking layer of C. As more Ni sites

become exposed, k_{10} increases, leading to the rise in P_{CO_2} observed as well as the anode's improved sensitivity to gas phase components. However, prior to the rise in potential and P_{CO_2} (the first half of Period I), P_{CO_2} was monotonically decreasing, which is odd considering the elementary reactions. If Equation 33 were responsible for the production of CO_2 during the equilibration time prior to O_2 exposure, then we would expect as P_{CO} increased to see an increase in P_{CO_2} via chemical shift. If Equation 37 or 39 are responsible for CO_2 production at t=0, then an increase in P_{CO} and P_{O_2} would also lead to an increase in P_{CO_2}. The decrease in P_{CO_2} must, therefore, result from some process which increases the utilization rate of CO_2, which could only be the reverse of Equation 33. If Equation 33 follows Ahhrenius behavior, then the rate constant for the reverse of Equation 33, k_{-4}, depends on the temperature of the cell, the activation energy, and, since catalytic Ni is likely covered initially, the surface area of C. The temperature of the cell is constant during this period, suggesting that the increase in k_{-4} is caused by either a change in the activation energy or the surface area of C. If we assume that C grew in such a way as to minimize its surface area (increasing the volume to surface area ratio), and surface energy (reacting at C sites with higher energy first), reversing that process by removing C would increase surface area and surface energy. Additional modeling and/or surface area measurements would be necessary to deconvolute the effects of surface area and activation energy.

We can therefore propose a mechanism for removal of C during Period I, which is seen in Figure 38. Since Equation 36 appears to be the dominant mechanism by which C is removed during the first half of Period I then the rate of C removal can be expressed as

$$-\frac{dC}{dt} = k_7 P_{O_2} \tag{41}$$

Or the rate of C removal depends on P_{O_2} and k_7. Since detected P_{O_2} remains at its initial value for the duration of this period, the consumption rate of O_2 must be near unity for this period. An extremely high consumption rate for a reactant that is being constantly added to a system is indicative of a rapid kinetic process followed by a sluggish process, thereby tying up the reactant in an intermediate form. As with our discussion of k_{-4}, k_7 is also dependent on the surface area of C and the activation energy for that reaction. If we assume for simplicity that the activation energy remains constant, then since P_{O_2} and the surface area of C have maximum values, the magnitude of Equation 41 would approach a constant. To explore how the kinetics of C removal on the cell evolve with time, we can define a region with a constant and small distance from the fuel inlet, R_1 in Figure 38. As P_{O_2} increases in R_1, the magnitude of Equation 41 approaches the maximum, $\delta_{C,max}$, Figure 38b Once that maximum is reached, excess P_{O_2} would be free to diffuse to R_2, Figure 38c This process repeats for each region until carbon removal kinetics are uniform across the fuel cell Figure 38d. At that point O_2 would begin to be detected in the exhaust gas. This kinetic system would give the area near the fuel inlet a head start on C removal and create spatially dependent carbon coverage values (θ_C), depending on the distance from the fuel inlet, Figure 38e.

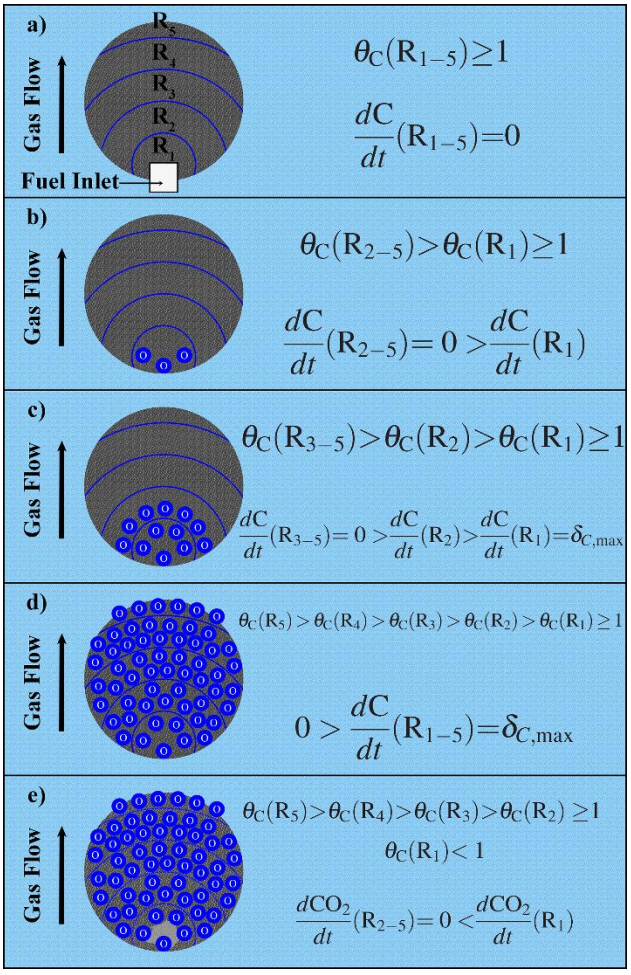

Figure 38 Schematic for the relationship between O_2 (blue O's) and spatially dependent C removal kinetics ($\frac{dC}{dt}$) in different regions (R_x) of on the anode, leading to regionally dependent C surface coverage (θ_C). a) Prior to oxygen exposure through the fuel inlet, θ_C is greater than or equal to 1 and $\frac{dC}{dt}$ in $R_{1\text{-}5}$ is 0. b) Subsequent to O_2 addition, θ_C and $\frac{dC}{dt}$ in R_1 begins to decrease, until c) P_{O_2} has reached its maximum in a R_1, $\left|\frac{dC}{dt}\right|$ also reaches a maximum ($\delta_{C,max}$), and O_2 is free to move to R_2, where θ_C and $\frac{dC}{dt}$ begin to decrease. d) This process continues for all regions, leaving spatially dependent θ_C, which is least in R_1 and greatest in R_2, until e) θ_C becomes less than 1 in R_1, and $\frac{dCO_2}{dt}$ begins to rise via Equation 39 in that region.

Spatially dependent θ_C provides a reasonable framework for the spatially dependent chemistry observed in Period II. First, the identity of the reaction responsible for heating

needs to be determined. At the onset of cell heating, P_{CO} passes through its maximum and begins to diminish rapidly. P_{CO_2} continues to increase rapidly eclipsing P_{CO} and rising until the middle of Period II (~300 sec). Taken together, these observations indicate that the heating observed on the fuel cell results from heat produced via Equation 39 (ΔH=-300 kJ/mol). Since the temperature of the fuel cell is increasing, the chemical reaction must be proceeding heterogeneously, as opposed to homogenously in the gas phase. Taken with the decrease in P_{CO_2} observed during the first half of Period I, and P_{CO_2} production increasing only subsequent to removal of the blocking layer of C, Equation 39 must be dependent on catalysis.

Over the duration of Period II, localized heating moves across the cell, until the temperature becomes uniformly elevated by ~5˚C across the cell. The localized heating, with directionality away from the fuel inlet, and the clear thermal front observed at 273 and 291 s, point to a process with rapid kinetics (Equation 36) and slow transport (O_2 flow across the anode) where the local concentration of a reactant is playing an important role in the chemistry. Understanding how the temperature of the cell changes is key to identifying that reactant. The change in temperature of any region of the cell is proportional to the rate of heat produced via exothermic chemistry less the rate of heat consumed via the gas and heat flow in the system. If the values for the rate of thermal energy consumption stays roughly constant, then the change in temperature is proportional to the rates of chemical processes occurring in that region. Given Equation 39's clear role and catalytic requirements, the rate is proportional to P_{CO}, P_{O_2}, and the number of Ni active sites. These three components then are the candidates for the reactant responsible for the observed

spatial dependence of the thermal response during this period. Since P_{CO} is increasing for the duration of Period I without thermal changes, while P_{O_2} remains constant until suddenly increasing just after 180 s, P_{O_2} would be an obvious candidate for the reactant responsible. However, while P_{O_2} appears dynamic, since it is appearing in the exhaust gas at this point, P_{O_2} should be relatively uniform across the cell, as discussed previously. Since O_2 is detected in the exhaust almost 150 s before the hotspot has moved across the cell, a P_{O_2} gradient cannot be solely responsible for the dynamic thermal changes. Therefore, Ni active sites must be involved in the spatially dependent kinetics. Likely then, the hypothesis proposed for the role of Equation 41 on the rate of C removal, and the formation of spatially heterogenous θ_C is correct, and responsible for the observed spatially heterogenous chemistry observed during Period II. At the start of Period II, carbon coverage at the fuel inlet was sufficiently low to allow significant catalysis for Equation 39, generating sufficient heat to overcome thermal equilibrium. The thermal front then is where the remaining EOC was oxidized to CO via Equation 36, exposing enough Ni sites for rapid catalysis of Equation 39 before CO can diffuse. If $\delta_{C,max}$ is roughly constant, then the amount of time for P_{O_2} to equilibrate across the whole cell, and start appearing in the exhaust (about 180s), will be about the same as the time it takes for the thermal front to reach the point furthest from the fuel inlet after forming, roughly 160 s, which is precisely what is observed during Period II.

Period III is defined by the gradual cooling of the cell from its maximum during Period II. The cooling is too gradual to be simply all exothermic processes halting and the cell returning to thermal equilibrium, which took about 30 s for electrolyte supported cells

heated to 820 °C electrochemically during chronocoulometry experiments.[120, 122] Rather it is more likely that as reactants and Ni active sites are irreversibly oxidized, their population gradually approach 0. At the start of Period III, P_{CO} is 30% greater than its initial value, and 40% of its peak value, while P_{O_2} must be roughly uniform across the cell. The OCV at this point has reached the Ni/NiO potential, therefore the Nernst potential corresponding to Equation 39 must be less than that corresponding to Equation 40. The rate by which P_{CO_2} decreases does not show a $t^{1/2}$ dependence (see S.I.), indicating that residual CO_2 is not simply diffusing from the porous anode. Rather, it is more likely that at the start of Period III there is still some C remaining on the cell. By the end of Period III, P_{CO_2} is higher than its initial value and P_{O_2} has not equilibrated, indicating that there are still some reactants remaining on the cell, including C. Despite this, according to the increase in potential at the end of Period III the accessible Ni is nearly, if not fully oxidized, and the same can be said for electrochemically accessible C. Alternatively, the increase in potential at the end of Period III could be caused by the formation of an insulating NiO layer between the electrode and the current collector, rather than all Ni being consumed. In this scenario the measured potential would then be determined by the difference between P_{O_2} in the anode and cathode chambers, which would be roughly -90 mV. The source of C for continued CO and CO_2 production during Period III then must reside on isolated Ni particles deep within the anode's porous network where gas access is obstructed, limited, or partially occluded. Given the spatial dependence of C removal on the surface of the cell, where there are no barriers to diffusion, C removal within the pores must be even slower. Therefore, C and Ni remaining within the pores at the end of the experiment would be reasonable.

The apparent cooling observed at the end of the experiment is not as extreme as seen during electrochemical oxidation, meaning whatever process causes that apparent cooling is not as extensive with O_2 as with electrochemical oxidation. If this apparent cooling is caused by decreased porosity, then as the porosity near the surface decreases, the rate by which O_2 can diffuse into those pores is limited, decreasing the rate of NiO formation according to Equation 40. Additionally, the dynamics of that cooling are different as compared to electrochemical oxidation. Where with electrochemical carbon removal the cooling spread from the center of the cell to the outer edges, the cooling observed with oxygen starts at the edges of the cell and moves inward. The apparent cooling can be observed as early as 273 s, near the bottom edge of the anode. The underlying cause for the onset of Ni oxidation from the edge of the cell is uncertain, though one hypothesis is that there is some unreduced NiO below the alumina paste on the cell. This NiO could act as a seed, allowing more NiO to form at the interface between NiO and Ni. Further analysis, including depth of NiO crystal growth, is needed to verify this hypothesis.

Carbon removal with steam.

Data Steam removes carbon from Ni-based SOFC anodes safely and effectively. Previous reports have shown that removing C with small amounts of steam in an inert carrier gas happened quickly and induced less damage to the anode microstructure relative to carbon removal with molecular oxygen.[37] From a mechanistic perspective, using steam to remove carbon adds chemical complexity, and has, therefore, been left for last in the analysis. As with both previously discussed experiments (electrochemical oxidation and

molecular oxygen), these experiments began by depositing C on the anode by exposing it to dry methane for 10 minutes, and then purging the system with Ar and allowing the cell to equilibrate for 10 minutes. Following this preparation, a mixture of 6% H_2 and 3% O_2 in Ar was introduced and used to define t=0 s for NIRTI, CP, and MS/FTIRES experiments. Kinetics experiments performed (not included) indicate that under these experimental conditions, more than 90% of the H_2/O_2 mixture convert to steam within 1 millisecond, and empirical experiments performed with MS indicate that this mixture reacts to completion to provide 6% steam in Ar, maintaining the same stoichiometric amount of atomic oxygen as the oxygen removal experiments. Results were also qualitatively similar to those performed with Ar passed through a bubbler, though the stoichiometric consistency was not maintained.

Unlike in the previous carbon remediation cases considered, carbon removal by steam shows less evidence of clear, differentiated removal mechanisms or of transitions between mechanisms. We attribute this less well-defined process to the chemical complexity brought on by having both hydrogen and oxygen present in the form of steam. While no single measurement can define specific carbon removal regimes, a combination of observations can still be used to infer how steam is removing carbon from the Ni anode. For consistency with previous sections, we will define Period I as occurring from 0 to ~ 60 s, Period II from 60s to 90s, Period III from 90s to ~120 s, Period IV from 120s to 200 s, Period V from 200-500s, and Period VI is from 500s to the end of the experiment at 1100 seconds. Justification for these designations is provided in the analyses below.

As with the above experiments, the results for C removal with steam begin by considering the NIRTI data, Figure 39. The temperatures referenced here are versus the initial temperature of the cell at t=0 s. During Period I, the cell remains at the initial temperature, see Figure 39-45 s. Then, during Period II the cell begins to cool globally by approximately -2 °C, Figure 39-67 s. The cooling continues until the end of Period II, where it reaches the coolest temperature across the cell, see Figure 39-85 s. At the start of Period III the cell begins to gradually warm to a $\Delta T=0$ °C, first in the area directly opposite the cathode, Figure 39-120 s. At the end of Period III, Figure 39-133 s, the area directly opposite the cathode has returned to the thermal equilibrium temperature (See SI -Figure 5 for a higher resolution image), and during Period IV, the remainder of the cell begins to warm, starting at the area directly in front of the fuel inlet (Figure 39-133 s), then spreading across the cell in the direction of the gas stream, with the areas adjacent to the fuel inlet warming last, Figure 39-155s. The cell remains at the initial temperature until Period VI, where the cell's edges begin to cool, starting with those areas outside the fuel stream and directly opposite the cathode Figure 39-568 s and 622 s. That cooling spreads to the whole cell, Figure 39-806 s and 858 s, with the area directly in the gas stream and not above the cathode remaining near the equilibrium temperature the longest, Figure 39-707 s. The cell eventually cools to -10 °C by the end of Period VI, Figure 39a-1111 s, similar to the end of electrochemical oxidation, Figure 33-2610 s.

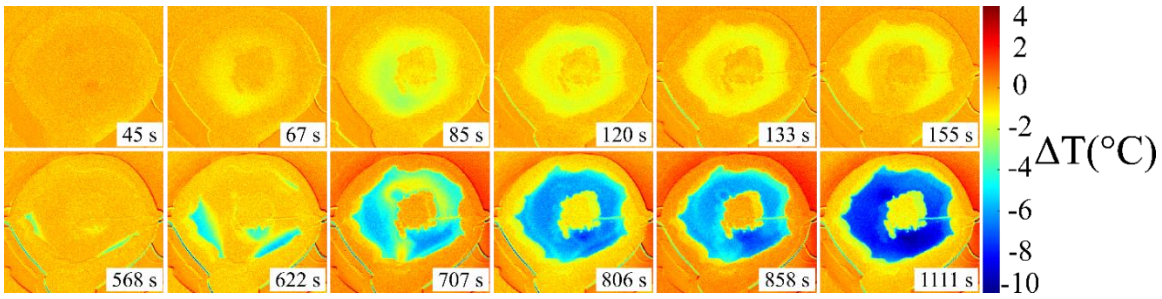

Figure 39 False color NIRTI images from C removal with steam experiment showing change in temperature from initial temperature between 4 and -10 °C at relevant times (45 s, 67 s, 85 s, 120 s, 133 s, 155 s, 568 s, 622 s, 707 s, 806 s, 858 s, and 1111 s)

CP data during Period I (Figure 40a) shows some consistency to behavior observed during carbon removal with O_2. Electrochemical data fluctuate between -1.1 and -1.08 V, without corresponding changes to gas phase partial pressure, but generally remains flat until the start of Period II, when it begins to rise gradually with some slight fluctuations. The OCV begins to rise more smoothly in Period III (90-120 s) before increasing rapidly in Period IV (120-200 s). In Period V (200-500 s) the OCV continues to rise and eventually converges to the Ni/NiO potential of 0.7 V shortly after the start of Period VI where it remains until the end of the experiment. The constant OCV in Period VI implies that Ni oxidation with steam is self-limiting, with Ni oxidation by steam's oxygen balanced by NiO's reduction by steam's hydrogen, see Equation 45.

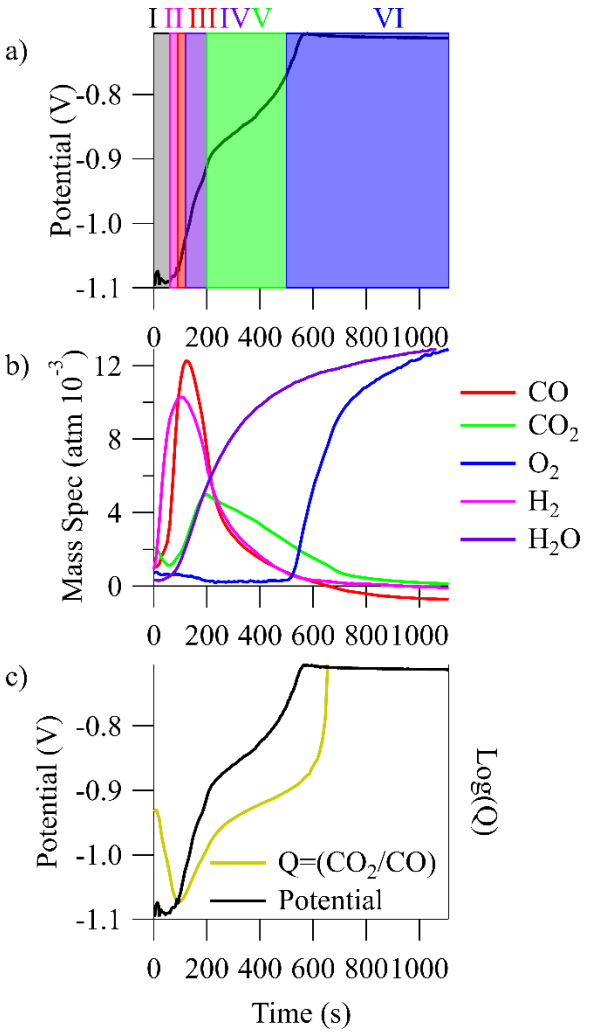

Figure 40 Data collected as part of the steam experiments with a) CP, b) MS and c) Plot of current with the logarithm of reaction quotient for Equation 49.

As with C removal by molecular oxygen, FTIRES results matched closely to MS, so were excluded from Figure 40b, but can be found in SI-Figure 6. The MS results, Figure 40b, appear at first glance to be like those observed with both C removal by electrochemical oxidation and by molecular oxygen with P_{CO} peaking before P_{CO_2}. P_{CO} begins slowly rising at the beginning of Period I, and peaks at the transition between Period II and III, before decreasing for the remainder of the experiment. The value of P_{CO} eventually decreases below the value determined to be 0 during Period VI. P_{CO_2} decreases during Period I, begins

to rise at the end of that period, peaks around the start of Period IV, then gradually decreases until the end of the experiment. P_{O_2} remains at 0 until the start of Period VI (nominally the start of the Ni/NiO equilibrium via Figure 40a), when it rapidly begins to climb, leveling off at ~700 seconds. The maximum current measured by the MS for P_{O_2} is an order of magnitude less than what was observed during carbon removal with molecular oxygen. P_{H_2} begins rising at the start of the experiment, peaks before P_{CO} at the end of Period II, then decreases until the end of the experiment. P_{H_2O} begins to rise around the same time as P_{H_2} peaks, the beginning of Period III, and then rapidly rises before approaching an asymptotic limit in Period VI.

Interpretation With the introduction of steam, the likely reactions occurring become more complicated compared to those when O_2 was added. Potential reactions with steam are:

$$2CO \rightleftharpoons CO_2 + C \qquad \Delta H=-172.45^{100} \qquad (33)$$

$$C + H_2O \rightleftharpoons H_2 + CO \qquad \Delta H=131.296^{100} \qquad (42)$$

$$CO_2 + H_2 \rightleftharpoons H_2O + CO \qquad \Delta H=41.154^{100} \qquad (43)$$

$$O_2 + 2H_2 \rightarrow 2H_2O \qquad \Delta H=-241.826^{100} \qquad (44)$$

$$Ni + H_2O \rightleftharpoons NiO + H_2 \qquad \Delta H=2.126^{100,\ 155} \qquad (45)$$

$$H_2O \rightleftharpoons 2H^* + O^* \qquad \Delta H=927.002^{100} \qquad (46)$$

$$H_2 \rightleftharpoons 2H^* \qquad \Delta H=435.996^{100} \qquad (47)$$

$$O_2 \rightleftharpoons 2O^* \qquad \Delta H=249.18^{100} \qquad (48)$$

$$CO + O^* \rightarrow CO_2 \qquad \Delta H=-359.71^{100} \qquad (49)$$

The existence of atomic oxygen (O*) - likely adsorbed to the anode surface – is partially evidenced by the formation of molecular oxygen later in the experiment. The appearance of O_2 in the MS data is also presaged by the appearance of H_2 – implying adsorbed atomic hydrogen (H*) at much earlier times. These equations play important roles in identifying the chemistry that occurs during each Period of these steam experiments. Again, it is assumed that for this experiment that Equation 44 has gone to completion by the start of the experiment.

We can now begin to explore the chemical processes occurring during each Period of the experiment. Similarly, to C removal with molecular oxygen, the spatially heterogeneous chemistry necessitates the description of specific regions on the cell, Figure 41a, with R_1 being that area directly under the fuel inlet, R_2 being those areas outside the fuel stream, and R_3 the area directly opposite the cathode.

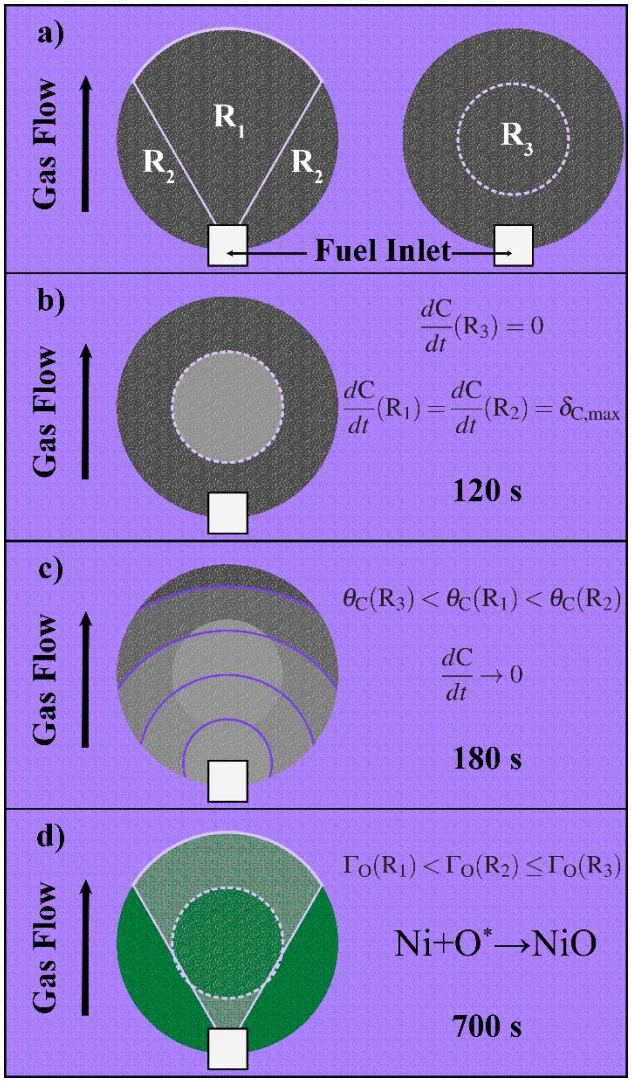

Figure 41 Schematic depicting the origins of spatially dependent chemistry occurring during C removal with steam. a) the Regions of interest on the cell R_1, the area in the directly in fuel stream, R_2 those areas outside the fuel stream, and R_3 the region opposite the cathode. b) $\frac{dC}{dt}$ in the region opposite the cathode (R_3) has ended at the start of Period III but is constant in the other areas of the cell. c) During Period IV the θ_C is decreasing in a manner reminiscent of C removal with O_2 as $\frac{dC}{dt}$ ends. d) NiO formation in R_2 and R_3 resulting from spatially dependent Γ_O.

Both NIRTI and CP during Period I indicate that very little chemistry is occurring, but the MS data suggest a different story. Given the simultaneous increase in P_{CO} and P_{H_2} during Period I, the most likely reaction occurring during Period I is Equation 42. The

decrease in P_{CO_2} during Period I has two equally plausible causes. First, P_{CO_2} could decrease from Equation 43, with increasing P_{H_2} and P_{CO}. Second, an increasing C surface area /activation energy, as was observed with the molecular oxygen experiments, related to Equation 33, could also plausibly explain the decrease in P_{CO_2}, especially since P_{CO_2} begins increasing before P_{H_2} peaks. Deconvoluting these two mechanisms is impossible with the available tools, though the decreasing rate for the production of H_2 toward the end of Period I does indicate that there is some validity to the latter hypothesis.

A combination of changes in MS, NIRTI, and CP signify the end of Period I and the beginning of Period II. First, P_{CO_2} reaches a minimum and then begins to increase. Simultaneously, the global cooling of the fuel cell begins, and OCV begins to rise. The global cooling indicates that the partial pressure of the reactants for whichever reaction is causing the cooling are well distributed over the cell, unlike the spatially heterogenous reactivity observed for C removal with molecular oxygen. Additionally, the rise in OCV indicates that the cell is becoming more sensitive to changing partial pressure of gases and, like the previous experiment, that catalytic Ni is becoming exposed, a hypothesis supported by the rise in P_{CO_2}. The reaction scheme described above does not include endothermic processes that would cause P_{CO_2} to increase meaning that there is no simple explanation for the observed cooling. However, if P_{H_2O} had diffused across the cell, reaching its maximum partial pressure, then the rate of the Equation 43 would have reached a high value, possibly sufficiently high to counteract the rate of heat being added to the system and thereby cooling the electrode. The global nature of the cooling indicates that the reactants causing that cooling are well distributed, supporting this hypothesis. The

temperature of the cell reaches a minimum at the end of Period II just before H_2 production reaches a maximum and the CO_2 loss is at its lowest point. As the experiment moves into Period III, the dominance of Equation 43 will begin to wane as Equation 49 supersedes the kinetics of C removal. If the global cooling is, in fact, the result of Equation 43, then we conclude that carbon is being removed from the cell globally, unlike the spatially heterogeneous carbon removal observed when molecular oxygen was introduced.

Shortly after the beginning of Period III, H_2 concentration begins to decrease as P_{H_2O} begins to rise, indicating that P_{H_2O} is now in excess across the cell. The increasing steam observed could either be unreacted steam added to the system, or newly formed steam from recombining H* and O*, Equation 46 reversed. The monotonically rising OCV is qualitatively matched closely by the $\log(P_{CO_2}/P_{CO})$ (Figure 40c) indicating that the cell potential during Periods III and IV are largely controlled by CO/CO_2 oxidation. NIRTI shows that the temperature of the cell is returning to $\Delta T = 0$ °C in those areas opposite the cathode. We attribute this warming to the kinetics of CO oxidation by surface oxygen species (Equation 49) overtaking those of C removal, Figure10b). The fact that this warming begins opposite the cathode is not only evidence of the role of surface oxygen species, but also the diffusion of these species through the electrolyte at no applied overpotential. The reversibility of the temperature changes strongly indicates that the cell actually cooled during Period II, rather than experience a change in material composition (and emissivity) resulting in an apparent cooling as is seen at the end of experiments when the Ni anode is oxidized to NiO. By the end of Period III, P_{CO} has reached a maximum value, indicating that CO oxidation is now faster than CO production.

At the start of Period IV, those areas directly in front of the fuel inlet first begin to return to thermal equilibrium, in a manner very reminiscent of C removal with molecular oxygen, indicating the end of Eq 13. As was the case with C removal with molecular oxygen, since these areas were the first to be exposed to oxidant, these are also the areas where C removal begins, and so are the areas where heterogenous C removal finishes first and CO oxidation kinetics overtake them, Figure 41c. Unlike what was observed with C removal with molecular oxygen, those areas opposite the cathode appear to have some significant source of oxidants for C removal, resulting in those areas beginning to oxidize CO earlier. By the end of Period IV, the entire cell has returned to initial temperature, and P_{CO_2} begins to decrease. Period V then is defined by the more slowly rising OCV, which is likely caused by Equation 49 given the OCV's dependence on $\log(P_{CO_2}/P_{CO})$. As with electrochemical oxidation, the reverse of Equation 33 appears to play an important role in the formation of CO, which is subsequently oxidized by atomic oxygen from steam dissociation to produce additional CO_2. This source of CO is in addition to the CO produced via Equation 42, although the lack of additional H_2 produced at this time may indicate that Equation 33 is dominant in CO production for this period. However, given the extremely high rate of H_2 oxidation it's not surprising that H_2 is not observed in the exhaust.

The latter stages of the experiment are dominated by Ni being converted to NiO. Our analysis begins by assuming that H_2O dissociatively chemisorbs on the Ni surface, creating populations of surface hydrogen (H*) and oxygen (O*). H* being consumed faster than O* goes a long way to explaining the spatially dependent NiO formation observed during Period VI, Figure 39. Given that the OCV has reached the Ni/NiO potential shortly,

less than 20 seconds, before NiO begins appearing on the cell (as evidenced by apparent cooling in the NIRTI), as well as the low values for P_{CO} and P_{CO_2}, we anticipate that nearly all of the C, even C deep in the porous anode, has likely been fully removed by the start of Period VI. P_{O_2} also begins increasing at the start of Period VI, indicating that there are no longer any oxidizable reactants available for O* to react with other than itself, allowing O* to recombine and O_2 to begin evolving off the cell. The significantly lower P_{O_2} signal from these experiments, as compared to those during carbon removal with molecular oxygen, further supports this hypothesis. Since NiO begins forming outside of the gas stream on the cell, likely then R_2 and R_3 represent the greatest concentration of excess O*, Γ_O. Since O* and H* form via Equation 46, and given H*'s clear reactivity, then H* likely does not stay on the cell long enough to diffuse to areas outside the gas stream, despite H*'s higher surface diffusion resulting in a Γ_O in R_2, Figure 41d). Additionally, the non-faradaic oxide flux, first observed in Period II, also explains the increased Γ_O in R_3. Excess Γ_O is why NiO begins forming in R_2 and R_3 in Figure 39 at 568s. The apparently warmer R_1 at 622 s and 707 s then indicate where the gas stream is directed over the cell, and where a slightly higher Γ_H could exist. Interestingly, despite the presence of molecular oxygen, the OVC of the cell never exceeds the Ni/NiO potential, unlike C removal with molecular oxygen.

Comparison of C removal methodology

While each experiment removes C using different oxidants, there are a few behaviors which all three methodologies share. First, CO appears and peaks prior to CO_2 in all cases. This supports the hypothesis that CO_2 is produced is a stepwise manner, first C is oxidized to CO which is subsequently oxidized to CO_2. The separation between peaks

for CO and CO_2 is least for electrochemical oxidation, merely 20 s, whereas steam and oxygen are both separated by about 90 s. The closeness of the CO and CO_2 peaks for electrochemical oxidation is likely related to the interdependence of CO production via CO_2 during that experiment. Second, CO_2 appears to be playing an important role in removing C from the cell via Reverse Boudouard chemistry in all cases. For electrochemical oxidation, that Reverse Boudouard chemistry provides fuel for an extended period, long after the EAC has been removed from the cell, and even when Ni has become a major source of electrons. The evidence for Reverse-Boudouard chemistry for C removal with molecular oxygen and steam come from the Nernst potential plots. Third, all three methodologies end with the cell at an apparently lower temperature than they began the experiment with. Since we attribute this apparent cooling to NiO formation, it is not surprising that these cells end with some NiO formation, however the irreversible nature of that cooling supports that the apparent change in temperature is from a change in emissivity. The degree of cooling for molecular oxygen appears to be less extreme than for either steam or electrochemical C removal, likely due to the more global oxidation occurring with both steam and electrochemical oxidation and the limited ability for oxygen to diffuse through the cell. Fourth, spatially heterogeneous chemistry occurs in all three cases, and in each case reveals much information about the mechanism by which C is removed from the cell. Spatially heterogenous chemistry occurring on SOFCs has long been either ignored or mentioned and subsequently discounted in literature. The spatial heterogenic chemistry is only revealed by imaging the entire cell simultaneously, and such information cannot be gained from either global measurement, such as MS or

electrochemistry, or point source information, such as Raman spectroscopy. By observing the spatial heterogeneity, we were able to determine that non-faradaic oxide flux through the electrolyte occurs during these experiments, and that for steam at least, is important for removing C from the cell. Additionally, the fact that C removal with molecular oxygen is limited by oxygen transport, and that using oxygen to remove C in that manner can lead to spatially heterogenous C surface coverage could not have been determined without the use of NIRTI.

The gas phase oxidants, molecular oxygen and steam, both have similar behaviors which are not shared with electrochemical oxidation. First, P_{CO_2} initially decreases during both reactions. This dip in CO_2 further supports that C is not directly oxidized to CO_2 and that CO needs a catalytic surface to be oxidized to CO_2. For molecular oxygen, the dip in CO_2 is highly suggestive of an increase in C surface area or energy since, unlike steam, there is only a single process by which CO_2 can be consumed, and all other kinetics arguments would indicate that it's partial pressure should be increasing. The likely reason P_{CO_2} doesn't decrease during the initial periods of electrochemical oxidation is that as C has formed a blocking layer on the cell, similar to what was observed during the other two experiments, and therefore must be oxidized first at the TPB sites. Once those sites have become clear, they immediately become available for CO oxidation, and the CO produced from that initial C oxidation can be oxidized before it diffuses away. Second, there is strong evidence that CO_2 production requires a catalytic surface during these experiments. As just stated, both experiments see an initial dip in P_{CO_2}, and, importantly, P_{CO_2} only begins to increase once the electrochemistry becomes sensitive to changes in gas phase partial

pressures. This suggests that CO_2 production cannot begin until there is sufficient Ni surface area to catalyze CO oxidation. Electrochemical CO oxidation likely also requires a catalytic surface, however, since the C is removed from TPB sites first, the evidence for obligate catalysis during that experiment is less clear. Lastly, there is clear evidence using both methodologies that C removal rates have some transport related process occurring, leading to spatially distributed C surface coverage. This is evidenced by changes in temperature moving from the fuel inlet toward the outlet. That process occurs much more quickly with steam than it does with oxygen, suggesting that oxygen has a higher reactivity than steam, and is therefore consumed faster than it diffuses.

Carbon removal with steam and electrochemical oxidation also share similar behaviors which carbon removal with molecular oxygen lack. First, the area on the anode surface opposite the cathode appear to be playing a key role in the observed chemistry. This behavior for electrochemical oxidation is trivially explained since oxide flux through the electrolyte must be highest where oxide vacancies can be readily filled by the cathode. The fact that this area appears to be important with steam is interesting, and clear evidence of non-faradaic oxide flux and the importance of surface oxygen species for carbon removal. The non-faradaic oxide flux may have important implications for ideal operation conditions for SOFCs. For example, operating condition for high voltage, low current applications may be different than high current, low voltage applications. Second, the apparent cooling at the end of these experiments is more extreme than that observed for C removal with molecular oxygen. If the change in emissivity is due to changes in porosity, this could indicate that there are more overall changes to cell microstructure using these

methods than are found when using molecular oxygen. The increased changes in cell microstructure might be balanced by the third factor shared between electrochemical oxidation and steam, the lower partial pressure of all C containing species at the end of the experiment. Both experiments end with significantly lower P_{CO_2}, whereas C removal with molecular oxygen ends with 30% more P_{CO_2} than the experiment began with. This could indicate that both electrochemical oxidation and steam are more effective at clearing the cell of C than molecular oxygen. Third, both of these experiments had more clearly defined periods than molecular oxygen. This is likely due to the more global chemistry occurring during these periods, whereas with molecular oxygen the spatial distribution of chemistries leads to temporally distributed mechanistic periods, convoluting data from the global measurements of MS and electrochemistry. Finally, during both electrochemical oxidation and carbon removal with steam experiments, the cell remains at or near the initial temperature throughout most of the experiments. Likely this is due to the dominance of reversible reactions occurring during these experiments, and balance between endothermic and exothermic reactions.

Lastly, each experiment has unique behaviors which are not shared between them. First, the dynamics of NiO formation are different during each experiment. Electrochemical oxidation saw NiO forming first in the center of the cell and expanding out, while molecular oxygen formed NiO from the outside of the cell and worked its way toward the center. NiO formation under steam was almost a hybrid of the two, with NiO forming first at both the center of the cell and those areas outside the fuel stream. The dynamics of NiO formation provided key information about the dynamics of other

reactions occurring on the cell. For electrochemical oxidation, the formation of NiO at the area opposite the cathode informs us that C removal, and CO oxidation, occur primarily in that region, with little to no electrochemical reactions occurring outside that region. Second, C removal with molecular oxygen was the only experiment which saw dramatic heating occurring on the cell. This is likely related to the reactivity of oxygen, and the lack of reversible reactions occurring. The relative heights of P_{CO} and P_{CO_2} during C removal with molecular oxygen are also evidence of less Reverse Boudouard chemistry occurring, rather than evidence of "more complete" C oxidation. This is especially true given the high residual P_{CO_2} value at the end of the molecular oxygen experiment. Finally, the chemistry occurring with steam is more complex than with either electrochemical oxidation or molecular oxygen. This is evidenced not only by the increased variety of products observed in the MS, but also in the increased number of mechanistic periods. Despite the increased complexity, the periods also remain remarkably distinct, with evidence of a change in mechanism clearly observable in both MS and NIRTI simultaneously. This suggests that while C removal with steam is more complex than the other two reactions, it is also well distributed across the entire cell, allowing changes to mechanisms to be more distinct than with C removal with molecular oxygen.

Conclusion

Together, these experiments represent a significant development in the understanding of C removal on SOFC anodes. By combining operando optical and electrochemical measurements, the mechanisms for the remediation of SOFC anodes degraded by graphitic C via electrochemical oxidation, molecular oxygen and steam were

further developed. It was determined that C removal proceeds in a stepwise manner, first C is oxidized to CO, which is subsequently oxidized to CO_2. The latter process only occurs when a Ni surface is available to act as catalyst. CO_2 generated by C oxidation also played a key role in continuing to remove C from the cell via reverse Boudouard chemistry. Electrochemical oxidation and steam removed C in a more global (spatially) manner than O_2, which appeared to leave significant C remaining on the cell, despite electrochemical measurements indicating the complete oxidation of the cell. Spatially heterogenous chemistry was observed throughout all experiments and played a key role in determining the mechanisms for C removal, including transport dependent processes with both O_2 and H_2O. That spatially heterogeneity must be considered when studying SOFCs, since both global measurements of fuel cell performance, electrochemistry and MS, as well as point source measurements for fuel cell materials (Raman Spectroscopy) cannot differentiate the spatial dependencies of their measurements.

Acknowledgements

The authors acknowledge support for this work from the Office of Naval Research, USA (N00014-17-1-2808 and N0001420WX01034).

CHAPTER SIX

CONCLUSIONS AND FUTURE DIRECTIONS

Conclusions

The experiments conducted for this dissertation were carried out to fundamentally advance the community's understanding of the chemical mechanisms responsible for SOFC anode degradation and regeneration. To do so, a combination *operando* optical and coupled electrochemical techniques were applied to monitor and characterize SOFC anode degradation and regeneration from S and graphitic C. Coupling these techniques provided insight into how S reduces SOFC performance, and the mechanisms that remove graphitic C from anodes whose performance has been degraded by coke. This work represents the latest efforts in the long-term collaboration between researchers at Montana State University and the Naval Research Laboratory in Washington D.C.

Chapter 2 developed the theory and limitations of an electrochemical technique newly adapted to SOFC, Chronocoulometry. The more common form of chronocoulometry, double-potential-step chronocoulometry (DPSCC), proved ineffective for monitoring adsorbed reactants on SOFCs since overpotentials sufficient to drive the cell to a diffusion limited current were sufficient to oxidize the electrode. Fortunately, multi-potential-step chronocoulometry (CC), while less common than DPSCC, proved effective at characterizing changes in SOFC performance that could be modeled as a loss of anode triple phase boundary. CC exploits the heterogeneous chemistry of SOFC anodes to enable the direct characterization TPB boundary length by monitoring the potential

independent charge produced from a series of potential steps. The necessity for accurate overpotential applications to the working electrode necessitated a three-electrode geometry to minimize voltage loss through the bulk resistance of the electrolyte, and a highly functional SOFC electrode is necessary to enable measurements to be physically significant.

Chapter 3 and Chapter 4 used CC with simultaneous *operando* N-IR thermal imaging (NIRTI) to characterize electrolyte supported cells operating with sulfur contaminated hydrogen and syngas from 600-800 °C. During Chapter 3, findings implied that TPB length varies with operational temperatures, likely due to deactivation of TPB sites by the formation of a reduced zirconia phase at lower temperatures. S contamination was confirmed to be more severe at lower temperatures than higher and was found to be more complex than S simply blocking active sites in the TPB. Rather, S participates in electrochemical reactions, decreasing electrode performance through sluggish S oxidation kinetics, rather than by simply limiting the number of TPB active sites. Simultaneous thermal imaging enabled the determination, through an Arrhenius analysis, that a synergistic effect between oxide transport and exothermic hydrogen oxidation was responsible for a positive concavity in CC data, and that H oxidation appears to follow first order kinetics. That first order dependence ends at lower temperatures with high S partial pressures, suggesting that S oxidation becomes rate limiting under those conditions. Chapter 4 again employed CC with simultaneous NIRTI to characterize electrolyte supported cells operating with sulfur contaminated syngas at 800 °C. CC found that CO diminished TPB length in a manner that was insensitive to CO partial pressure, either by

not participating in electrochemical reactions or by forming a layer of graphitic carbon. Upon the introduction of S, TPB length increased beyond what would be expected for syngas, suggesting that S prevents CO adsorption, preventing CO from blocking electrochemically active sites and/or graphitic C formation.

During Chapter 5, *operando* NIRTI, in combination with simultaneous Fourier Transform Infrared Emission Spectroscopy (FTIRES), Mass Spectrometry (MS), and Chronopotentiometry/Chronoamperometry (CP and CA respectively), monitored graphic C removal from precoked anode supported SOFCs at 800 °C using electrochemical oxidation, molecular oxygen, and steam. During each of the experiments, distinct mechanistic periods were observed, and the reactants responsible during those periods were determined. Each experiment found that C is not directly oxidized to CO_2, rather first to CO, and subsequently to CO_2. CO oxidation to CO_2 was also found to require a catalytic surface and was unable to proceed prior to the exposure of catalytic Ni. Spatially heterogenous chemistry was observed during each experiment, and the details of specific reactions in specific regions of the cell played a key role in determine the overall, sequential mechanisms of C removal from the cell. Both steam and electrochemical oxidation remove C in a less spatially heterogenous manner than molecular oxygen. Carbon removal with molecular oxygen showed sluggish transport of a reactive front across the cell due to high oxygen consumption rates closer to the gas inlet. During both the C removal experiments using steam and electrochemical oxidation the area opposite the cathode played a previously unreported key role in C removal. This observation is trivial for electrochemical oxidation, however for C removal with steam it suggests that nonfaradaic oxide flux

through the electrolyte and surface oxygen species play a key role in C removal. The formation of molecular oxygen during the experiments with steam also implies that surface oxygen is responsible for C removal on SOFCs. Finally, oxygen appeared to be less effective at removing C from the cell than either electrochemical oxidation or steam, as evidenced by lingering CO_2 in the exhaust gas, despite CP measurements indicating that all other reducing agents had been depleted (C and Ni).

Together, these experiments demonstrate the utility of combining quantitative electrochemical techniques with simultaneous *operando* optical measurements when studying the complex chemistry and material changes occurring during SOFC operation. While additional experimentation is required to further validate and explore SOFC chemistries, this work represents significant process in elucidating SOFC mechanisms.

Future Directions

Sulfur Passivation of SOFC Anodes for Coke Free Operation

SOFCs represent an exciting frontier that bridges heterogeneous catalysis and electrochemistry. Experiments performed in this dissertation explore that relationship, using electrochemical methods simultaneously with *operando* optical techniques to quantify heterogenous chemistry occurring in fully functional devices. The interrelated chemistries occurring naturally draw parallels between SOFCs and heterogenous catalysts, especially in systems that use the same catalyst materials: Ni, and gas phase reactants, hydrocarbons. Some of the degradation pathways that exist for these catalytic systems (e.g., graphitic C and S) also exist in SOFCs, and many of the solutions to improve the efficiency and durability of catalytic systems have also been applied to SOFC electrode design, as

discussed in Chapter One. For example, one of the primary solutions for C formation during catalytic methane reforming on Ni catalysts for syngas production is the use of S to selectively poison the C formation reaction while leaving the steam cracking pathway open, in a process known as sulfur passivated reforming (SPARG), which is distinct from sparging.[147, 156-158] For syngas production, SPARG has the advantage of increasing the CO to H_2 ratio, as well as enabling stable operation under conditions where C would likely form.[156, 158] Sulfur is believed to limit C into smaller assemblies, maintaining a C surface area and low C surface coverage, by preferentially blocking Ni grain boundary sites at which C formation is more favored.[147] The role S plays in C formation on SOFCs is entirely unstudied, probably due to the inability for most methods to monitor C formation directly, and instead inferring C formation from performance degradation during operation, or from *ex situ* analysis.[18, 28-30, 36, 159] Since our experimental assembly enables simultaneous observation of both C formation and electrochemical performance degradation, a comparative study of C formation and electrochemical performance degradation of sulfur passivated SOFC anodes is the next logical step to continue to explore the relationship between heterogeneous catalysis and electrochemical performance.

Recent experiments performed on electrolyte supported cells at 800 °C under dry methane indicate that C formation is significantly reduced with 10 ppm H_2S, see Figure 42. Future experiments will monitor electrochemical performance degradation with EIS and LSV, along with C formation, at lower H_2S partial pressures will seek to determine if C formation is degraded faster than electrochemical performance. Should results prove general, they suggest that for SOFC systems, there is an optimal C/S ratio that would enable

coke free operation without the use of reformates. Additional studies using thermal imaging to monitor CH_4 conversion, which has a distinct thermal signature, as well as MS and FTIRES to monitor CO-CO_2 partial pressures during operation are also logical next steps.

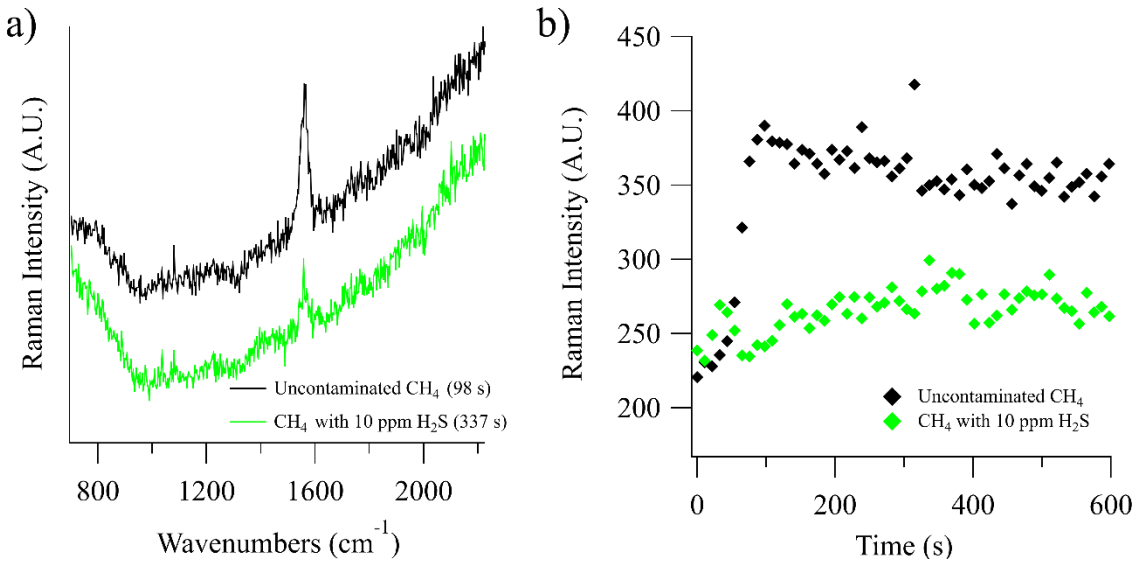

Figure 42 Raman Spectroscopy measurements of C formation at 800 °C on an electrolyte supported Ni-YSZ anode with and without 10 ppm H_2S with a) the highest over baseline peaks and b) evolution of C intensity over 10 minutes.

Additionally, the $Q_{ads}(\tau)$ behavior under hydrogen shortly after coking showed secondary maximum after the initial, which was approximately 8 times larger than the first, see Figure 43. Further analysis is required, but a secondary peak may indicate the ability for CC to monitor the kinetics of adsorbed reactant oxidation. These chronocoulometry experiments, taken with the S passivated experiments will further develop our understanding of SOFCs chemical mechanisms, and will offer directions to improve their performance.

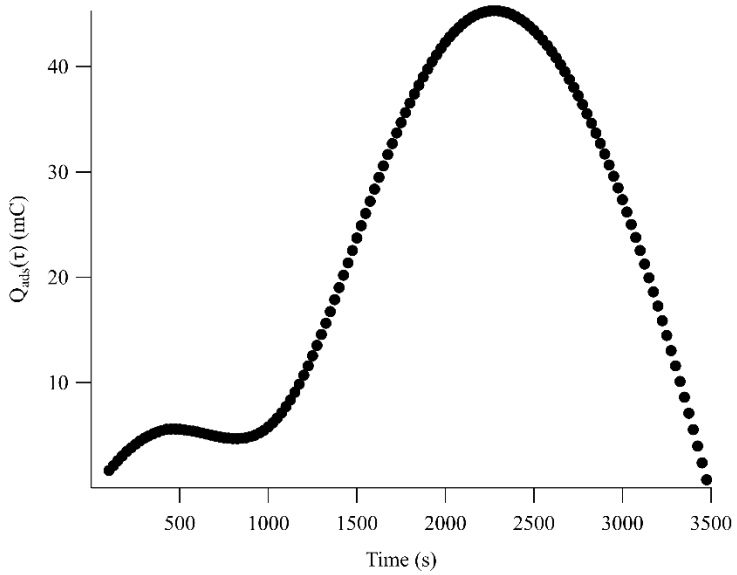

Figure 43 $Q_{ads}(\tau)$ plot of electrolyte supported cell at 800 °C under 50% H_2 after coking but prior to decoking

REFERENES CITED

1. Jia, J. X.; Li, Q. A.; Luo, M.; Wei, L. M.; Abudula, A., Effects of gas recycle on performance of solid oxide fuel cell power systems. *Energy* **2011,** *36* (2), 1068-1075.

2. Graves, C.; Ebbesen, S. D.; Mogensen, M.; Lackner, K. S., Sustainable hydrocarbon fuels by recycling CO2 and H2O with renewable or nuclear energy. *Renew. Sust. Energ. Rev.* **2011,** *15* (1), 1-23.

3. Larminie, J.; Dicks, A., *Fuel Cell Systems Explained*. J. Wiley: Chichester, West Sussex, 2003.

4. Goodenough, J. B., Oxide-ion electrolytes. *Ann. Rev. Mater. Res.* **2003,** *33*, 91-128.

5. Singhal, S. C.; Kendall, K., *High-temperature Solid Oxide Fuel Cells: Fundamentals, Design and Applications*. Elsevier Science: 2003.

6. Ormerod, R. M., Solid oxide fuel cells. *Chemical Society Reviews* **2003,** *32* (1), 17-28.

7. Wojcik, A.; Middleton, H.; Damopoulos, I.; Van herle, J., Ammonia as a fuel in solid oxide fuel cells. *J. Power Sources* **2003,** *118* (1-2), 342-348.

8. McIntosh, S.; Gorte, R. J., Direct hydrocarbon solid oxide fuel cells. *Chem. Rev.* **2004,** *104* (10), 4845-4865.

9. Ni, M.; Leung, M. K. H.; Leung, D. Y. C., Parametric study of solid oxide fuel cell performance. *Energy Conv. Manag.* **2007,** *48* (5), 1525-1535.

10. Niakolas, D. K., Sulfur poisoning of Ni-based anodes for Solid Oxide Fuel Cells in H/C-based fuels. *Applied Catalysis A: General* **2014,** *486*, 123-142.

11. Gong, M.; Liu, X.; Trembly, J.; Johnson, C., Sulfur-tolerant anode materials for solid oxide fuel cell application. *J. Power Sources* **2007,** *168* (2), 289-298.

12. Din, Z. U.; Zainal, Z. A., Biomass integrated gasification-SOFC systems: Technology overview. *Renew. Sust. Energ. Rev.* **2016,** *53*, 1356-1376.

13. Egorova, M.; Prins, R., Hydrodesulfurization of dibenzothiophene and 4,6-dimethyldibenzothiophene over sulfided NiMo/gamma-Al2O3, CoMo/gamma-Al2O3, and Mo/gamma-Al2O3 catalysts. *J. Catal.* **2004,** *225* (2), 417-427.

14. Sasaki, K.; Susuki, K.; Iyoshi, A.; Uchimura, M.; Imamura, N.; Kusaba, H.; Teraoka, Y.; Fuchino, H.; Tsujimoto, K.; Uchida, Y.; Jingo, N., H2S poisoning of solid oxide fuel cells. *J. Electrochem. Soc.* **2006,** *153* (11), A2023-A2029.

15. Matsuzaki, Y.; Yasuda, I., The poisoning effect of sulfur-containing impurity gas on a SOFC anode: Part I. Dependence on temperature, time, and impurity concentration. *Solid State Ionics* **2000,** *132* (3-4), 261-269.

16. Hagen, A.; Rasmussen, J. F. B.; Thyden, K., Durability of solid oxide fuel cells using sulfur containing fuels. *J. Power Sources* **2011,** *196* (17), 7271-7276.

17. Ramos, T.; Hjelm, J.; Wandel, M.; Hagen, A.; Mogensen, M., Performance and Electrochemical Characterisation of Thin Electrolyte SOFCs. *ECS Transactions* **2008,** *13*.

18. Finnerty, C. M.; Coe, N. J.; Cunningham, R. H.; Ormerod, R. M., Carbon formation on and deactivation of nickel-based/zirconia anodes in solid oxide fuel cells running on methane. *Catal. Today* **1998,** *46* (2-3), 137-145.

19. Boldrin, P.; Ruiz-Trejo, E.; Mermelstein, J.; Menendez, J. M. B.; Reina, T. R.; Brandon, N. P., Strategies for Carbon and Sulfur Tolerant Solid Oxide Fuel Cell Materials, Incorporating Lessons from Heterogeneous Catalysis. *Chem. Rev.* **2016,** *116* (22), 13633-13684.

20. Kirtley, J. D.; Halat, D. M.; McIntyre, M. D.; Eigenbrodt, B. C.; Walker, R. A., High-Temperature "Spectrochronopotentiometry": Correlating Electrochemical Performance with In Situ Raman Spectroscopy in Solid Oxide Fuel Cells. *Anal. Chem.* **2012,** *84* (22), 9745-9753.

21. Kirtley, J. D.; Pomfret, M. B.; Steinhurst, D. A.; Owrutsky, J. C.; Walker, R. A., Toward a Working Mechanism of Fuel Oxidation in SOFCs: In Situ Optical Studies of Simulated Biogas and Methane. *J. Phys. Chem. C* **2015,** *119* (23), 12781-12791.

22. Kirtley, J. D.; Steinhurst, D. A.; Owrutsky, J. C.; Pomfret, M. B.; Walker, R. A., In situ optical studies of methane and simulated biogas oxidation on high temperature solid oxide fuel cell anodes. *Phys. Chem. Chem. Phys.* **2014,** *16* (1), 227-236.

23. McIntyre, M. D.; Kirtley, J. D.; Halat, D. M.; Reeping, K. W.; Walker, R. A. In *In situ Spectroscopic Studies of Carbon Formation in SOFCs Operating with Syn-gas*, 13th International Symposium on Solid Oxide Fuel Cells (SOFC-XIII), Okinawa, JAPAN, Oct 06-11; Okinawa, JAPAN, 2013; pp 1267-1275.

24. McIntyre, M. D.; Kirtley, J. D.; Singh, A.; Islam, S.; Hill, J. M.; Walker, R. A., Comparing in Situ Carbon Tolerances of Sn-Infiltrated and BaO-Infiltrated Ni-YSZ Cermet Anodes in Solid Oxide Fuel Cells Exposed to Methane. *J. Phys. Chem. C* **2015,** *119* (14), 7637-7647.

25. Sasaki, K.; Teraoka, Y., Equilibria in fuel cell gases - II. The C-H-O ternary diagrams. *J. Electrochem. Soc.* **2003,** *150* (7), A885-A888.

26. Lin, Y. B.; Zhan, Z. L.; Liu, J.; Barnett, S. A., Direct operation of solid oxide fuel cells with methane fuel. *Solid State Ionics* **2005,** *176* (23-24), 1827-1835.

27. Niakolas, D. K.; Ouweltjes, J. P.; Rietveld, G.; Dracopoulos, V.; Neophytides, S. G., Au-doped Ni/GDC as a new anode for SOFCs operating under rich CH4 internal steam reforming. *Int. J. Hydrog. Energy* **2010,** *35* (15), 7898-7904.

28. Alzate-Restrepo, V.; Hill, J. M., Carbon deposition on Ni/YSZ anodes exposed to CO/H-2 feeds. *J. Power Sources* **2010,** *195* (5), 1344-1351.

29. Alzate-Restrepo, V.; Hill, J. M., Effect of anodic polarization on carbon deposition on Ni/YSZ anodes exposed to methane. *Applied Catalysis a-General* **2008,** *342* (1-2), 49-55.

30. Subotic, V.; Harter, P.; Kusnezoff, M.; Napporn, T. W.; Schroettner, H.; Hochenauer, C., Identification of carbon deposition and its removal in solid oxide fuel cells by applying a non-conventional diagnostic tool. *Sustain. Energ. Fuels* **2021,** *5* (7), 2065-2076.

31. Koh, J. H.; Yoo, Y. S.; Park, J. W.; Lim, H. C., Carbon deposition and cell performance of Ni-YSZ anode support SOFC with methane fuel. *Solid State Ionics* **2002,** *149* (3-4), 157-166.

32. Itome, M.; Nelson, A. E., Methane oxidation over M-8YSZ and M-CeO2/8YSZ (M = Ni, Cu, Co, Ag) catalysts. *Catal. Lett.* **2006,** *106* (1-2), 21-27.

33. Qiao, J.; Zhang, N.; Wang, Z.; Mao, Y.; Sun, K.; Yuan, Y., Performance of mix-impregnated CeO2-Ni/YSZ Anodes for Direct Oxidation of Methane in Solid Oxide Fuel Cells. *Fuel Cells* **2009,** *9* (5), 729-739.

34. Welander, M. M.; Drasbk, D. B.; Traulsen, M. L.; Sudireddy, B. R.; Holtappels, P.; Walker, R. A., What does carbon tolerant really mean? Operando vibrational studies of carbon accumulation on novel solid oxide fuel cell anodes prepared by infiltration. *Phys. Chem. Chem. Phys.* **2020,** *22* (17), 9815-9823.

35. Subotic, V.; Schluckner, C.; Stoeckl, B.; Preininger, M.; Lawlor, V.; Pofahl, S.; Schroettner, H.; Hochenauer, C., Towards practicable methods for carbon removal from Ni-YSZ anodes and restoring the performance of commercial-sized ASC-SOFCs after carbon deposition induced degradation. *Energy Conv. Manag.* **2018,** *178*, 343-354.

36. Schluckner, C.; Subotic, V.; Lawlor, V.; Hochenauer, C., CFD-simulation of effective carbon gasification strategies from high temperature SOFC Ni-YSZ cermet anodes. *Int. J. Hydrog. Energy* **2017,** *42* (7), 4434-4448.

37. Kirtley, J.; Singh, A.; Halat, D.; Oswell, T.; Hill, J. M.; Walker, R. A., In Situ Raman Studies of Carbon Removal from High Temperature Ni-YSZ Cermet Anodes by Gas Phase Reforming Agents. *J. Phys. Chem. C* **2013,** *117* (49), 25908-25916.

38. Li, X. X.; Liu, M. F.; Lai, S. Y.; Ding, D.; Gong, M. Y.; Lee, J. P.; Blinn, K. S.; Bu, Y. F.; Wang, Z. H.; Bottomley, L. A.; Alamgir, F. M.; Liu, M. L., In Situ Probing of the Mechanisms of Coking Resistance on Catalyst-Modified Anodes for Solid Oxide Fuel Cells. *Chem. Mat.* **2015,** *27* (3), 822-828.

39. Huang, Q. A.; Hui, R.; Wang, B. W.; Zhang, H. J., A review of AC impedance modeling and validation in SOFC diagnosis. *Electrochim. Acta* **2007,** *52* (28), 8144-8164.

40. Bard, A. J., *Electrochemical methods : fundamentals and applications*. 2nd ed.. ed.; New York : Wiley: New York, 2001.

41. Jorgensen, M. J.; Mogensen, M., Impedance of solid oxide fuel cell LSM/YSZ composite cathodes. *J. Electrochem. Soc.* **2001,** *148* (5), A433-A442.

42. Primdahl, S.; Mogensen, M., Gas diffusion impedance in characterization of solid oxide fuel cell anodes. *J. Electrochem. Soc.* **1999,** *146* (8), 2827-2833.

43. Reeping, K. W.; Walker, R. A., In Operando Vibrational Raman Studies of Chlorine Contamination in Solid Oxide Fuel Cells. *J. Electrochem. Soc.* **2015,** *162* (12), F1310-F1315.

44. Noren, D. A.; Hoffman, M. A., Clarifying the Butler-Volmer equation and related approximations for calculating activation losses in solid oxide fuel cell models. *J. Power Sources* **2005,** *152* (1), 175-181.

45. Zha, S. W.; Cheng, Z.; Liu, M. L., Sulfur poisoning and regeneration of Ni-based anodes in solid oxide fuel cells. *J. Electrochem. Soc.* **2007,** *154* (2), B201-B206.

46. Li, N. H.; Lipkowski, J., Chronocoulometric studies of chloride adsorption at the Pt(111) electrode surface. *J. Electroanal. Chem.* **2000,** *491* (1-2), 95-102.

47. Anson, F. C., Innovations In Study Of Adsorbed Reactants By Chronocoulometry. *Anal. Chem.* **1966,** *38* (1), 54-&.

48. Eigenbrodt, B. C.; Pomfret, M. B.; Steinhurst, D. A.; Owrutsky, J. C.; Walker, R. A., Direct, In Situ Optical Studies of Ni-YSZ Anodes in Solid Oxide Fuel Cells Operating with Methanol and Methane. *J. Phys. Chem. C* **2011,** *115* (6), 2895-2903.

49. Jasinski, M.; Ziewiec, K.; Wojciechowska, M., Real Time Thermal Imaging Of Solid Oxide Fuel Cell. *Archives of Metallurgy and Materials* **2019,** *64* (4), 1207-1212.

50. Kirtley, J. D.; Qadri, S. N.; Steinhurst, D. A.; Owrutsky, J. C., In situ, simultaneous thermal imaging and infrared molecular emission studies of solid oxide fuel cell electrodes. *J. Power Sources* **2016,** *336*, 54-62.

51. Kirtley, J. D.; Tsoi, S.; Qadri, S. N.; Steinhurst, D. A.; Reeping, K. W.; Walker, R. A.; Owrutsky, J. C., In Situ Optical Investigations of Contaminants in Operating Solid Oxide Fuel Cells. *Solid Oxide Fuel Cells 15 (Sofc-Xv)* **2017,** *78* (1), 1261-1272.

52. Montanini, R.; Quattrocchi, A.; Piccolo, S. A.; Amato, A.; Trocino, S.; Zignani, S. C.; Lo Faro, M.; Squadrito, G., Real-time thermal imaging of solid oxide fuel cell cathode activity in working condition. *Applied Optics* **2016,** *55* (25), 7142-7148.

53. Pomfret, M. B.; Steinhurst, D. A.; Kidwell, D. A.; Owrutsky, J. C., Thermal imaging of solid oxide fuel cell anode processes. *J. Power Sources* **2010,** *195* (1), 257-262.

54. Pomfret, M. B.; Steinhurst, D. A.; Owrutsky, J. C. In *Thermal Imaging of Solid Oxide Fuel Cell Anode Degradation with Dry and Wet Ethanol Fuel Flows*, 12th International Symposium on Solid Oxide Fuel Cells (SOFC), Montreal, CANADA, May 01-06; Montreal, CANADA, 2011; pp 1563-1570.

55. Reeping, K. W.; Kirtley, J. D.; Bohn, J. M.; Steinhurst, D. A.; Owrutsky, J. C.; Walker, R. A., Chlorine-Induced Degradation in Solid Oxide Fuel Cells Identified by Operando Optical Methods. *J. Phys. Chem. C* **2017,** *121* (5), 2588-2596.

56. Robinson, J. B.; Brown, L. D.; Jervis, R.; Taiwo, O. O.; Heenan, T. M. M.; Millichamp, J.; Mason, T. J.; Neville, T. P.; Clague, R.; Eastwood, D. S.; Reinhard, C.; Lee, P. D.; Brett, D. J. L.; Shearing, P. R., Investigating the effect of thermal gradients on stress in solid oxide fuel cell anodes using combined synchrotron radiation and thermal imaging. *J. Power Sources* **2015,** *288*, 473-481.

57. Pomfret, M. B.; Steinhurst, D. A.; Kidwell, D. A.; Owrutsky, J. C., Thermal imaging of solid oxide fuel cell anode processes. *J POWER SOURCES* **2010,** *195* (1), 257-262.

58. Li, X. X.; Blinn, K.; Fang, Y. C.; Liu, M. F.; Mahmoud, M. A.; Cheng, S.; Bottomley, L. A.; El-Sayed, M.; Liu, M. L., Application of surface enhanced Raman spectroscopy to the study of SOFC electrode surfaces. *Phys. Chem. Chem. Phys.* **2012,** *14* (17), 5919-5923.

59. Yu, J. S.; Zhang, Z. X., Double potential-step chronoamperometry and chronocoulometry at an ultramicrodisk electrode: Theory and experiment. *J. Electroanal. Chem.* **1997,** *439* (1), 73-80.

60. Stankovich, M. T.; Bard, A. J., Electrochemistry Of Proteins And Related Substances .3. Bovine Serum-Albumin. *J. Electroanal. Chem.* **1978,** *86* (1), 189-199.

61. Rutman, J.; Riess, I., Placement of reference electrode in solid electrolyte cells. *Electrochim. Acta* **2007,** *52* (20), 6073-6083.

62. Primdahl, S.; Mogensen, M., Oxidation of hydrogen on Ni/yttria-stabilized zirconia cermet anodes. *J. Electrochem. Soc.* **1997,** *144* (10), 3409-3419.

63. Finklea, H.; Chen, X. K.; Gerdes, K.; Pakalapati, S.; Celik, I., Analysis of SOFCs Using Reference Electrodes. *J. Electrochem. Soc.* **2013,** *160* (9), F1055-F1066.

64. Offer, G. J.; Shearing, P.; Golbert, J. I.; Brett, D. J. L.; Atkinson, A.; Brandon, N. P., Using electrochemical impedance spectroscopy to compensate for errors when measuring polarisation curves during three-electrode measurements of solid oxide fuel cell electrodes. *Electrochim. Acta* **2008,** *53* (26), 7614-7621.

65. Abdelrahman, A.; Abel, B.; Varga, A., Towards rational electrode design: quantifying the triple-phase boundary activity of Pt in solid acid fuel cell anodes by electrochemical impedance spectroscopy. *J. Appl. Electrochem.* **2017,** *47* (3), 327-334.

66. Doppler, M. C.; Fleig, J.; Opitz, A. K., The Influence of Sulfur Poisoning and YSZ Substrate Orientation on Electrochemical Properties of Nickel Pattern Anodes. *ECS Transactions* **2015,** *68* (1), 1383-1390.

67. Sukeshini, A. M.; Habibzadeh, B.; Becker, B. P.; Stoltz, C. A.; Eichhorn, B. W.; Jackson, G. S., Electrochemical oxidation of H-2, CO, and CO/H-2 mixtures on patterned Ni anodes on YSZ electrolytes. *J. Electrochem. Soc.* **2006,** *153* (4), A705-A715.

68. Utz, A.; Stormer, H.; Gerthsen, D.; Weber, A.; Ivers-Tiffee, E., Microstructure stability studies of Ni patterned anodes for SOFC. *Solid State Ionics* **2011,** *192* (1), 565-570.

69. Trembly, J. P.; Gemmen, R. S.; Bayless, D. J., The effect of coal syngas containing HCl on the performance of solid oxide fuel cells: Investigations into the effect of operational temperature and HCl concentration. *J. Power Sources* **2007,** *169* (2), 347-354.

70. Rasi, S.; Veijanen, A.; Rintala, J., Trace compounds of blogas from different blogas production plants. *Energy* **2007,** *32* (8), 1375-1380.

71. Marina, O. A.; Pederson, L. R.; Thomsen, E. C.; Coyle, C. A.; Yoon, K. J., Reversible poisoning of nickel/zirconia solid oxide fuel cell anodes by hydrogen chloride in coal gas. *J. Power Sources* **2010,** *195* (20), 7033-7037.

72. Reeping, K. W.; Bohn, J. M.; Walker, R. A., Palliative effects of H-2 on SOFCs operating with carbon containing fuels. *J. Power Sources* **2017,** *372*, 188-195.

73. Reeping, K. W.; Bohn, J. A.; Walker, R. A., Chlorine-induced degradation in SOFCs operating with biogas. *Sustain. Energ. Fuels* **2017,** *1* (6), 1320-1328.

74. Haga, K.; Adachi, S.; Shiratori, Y.; Itoh, K.; Sasaki, K., Poisoning of SOFC anodes by various fuel impurities. *Solid State Ionics* **2008,** *179* (27-32), 1427-1431.

75. Gong, M. Y.; Liu, X. B.; Trembly, J.; Johnson, C., Sulfur-tolerant anode materials for solid oxide fuel cell application. *J. Power Sources* **2007,** *168* (2), 289-298.

76. Cheng, Z.; Wang, J. H.; Choi, Y. M.; Yang, L.; Lin, M. C.; Liu, M. L., From Ni-YSZ to sulfur-tolerant anode materials for SOFCs: electrochemical behavior, in situ characterization, modeling, and future perspectives. *Energy Environ. Sci.* **2011,** *4* (11), 4380-4409.

77. Sasaki, K.; Haga, K.; Yoshizumi, T.; Minematsu, D.; Yuki, E.; Liu, R. R.; Uryu, C.; Oshima, T.; Ogura, T.; Shiratori, Y.; Ito, K.; Koyama, M.; Yokomoto, K., Chemical durability of Solid Oxide Fuel Cells: Influence of impurities on long-term performance. *J. Power Sources* **2011,** *196* (22), 9130-9140.

78. Zeng, Z. H.; Bjorketun, M. E.; Ebbesen, S.; Mogensen, M. B.; Rossmeisl, J., Origin of electrolyte-dopant dependent sulfur poisoning of SOFC anodes. *Phys. Chem. Chem. Phys.* **2013,** *15* (18), 6769-6772.

79. Gur, T. M., Comprehensive review of methane conversion in solid oxide fuel cells: Prospects for efficient electricity generation from natural gas. *Progress in Energy and Combustion Science* **2016,** *54*, 1-64.

80. Mahato, N.; Banerjee, A.; Gupta, A.; Omar, S.; Balani, K., Progress in material selection for solid oxide fuel cell technology: A review. *Progress in Materials Science* **2015,** *72*, 141-337.

81. Niu, B. B.; Jin, F. J.; Fu, R. J.; Feng, T.; Shen, Y.; Liu, J. C.; He, T. M., Pd-impregnated Sr1.9VMoO6-delta double perovskite as an efficient and stable anode for solid-oxide fuel cells operating on sulfur-containing syngas. *Electrochim. Acta* **2018,** *274*, 91-102.

82. Xue, S. S.; Shi, N.; Wan, Y. H.; Xu, Z. D.; Huan, D. M.; Zhang, S. W.; Xia, C. R.; Peng, R. R.; Lu, Y. L., Novel carbon and sulfur-tolerant anode material FeNi3@PrBa(Fe,Ni)(1.9)Mo0.1O5+delta for intermediate temperature solid oxide fuel cells. *Journal of Materials Chemistry A* **2019,** *7* (38), 21783-21793.

83. Roushanafshar, M.; Yan, N.; Chuang, K. T.; Luo, J. L., Electrochemical oxidation of sour natural gas over La0.4Ce0.6O1.8-La0.4Sr0.6TiO3 +/-delta anode in SOFC: A mechanism study of H2S effects. *Appl. Catal. B-Environ.* **2015,** *176*, 627-636.

84. Blinn, K. S.; Abernathy, H.; Li, X. X.; Liu, M. F.; Bottomley, L. A.; Liu, M. L., Raman spectroscopic monitoring of carbon deposition on hydrocarbon-fed solid oxide fuel cell anodes. *Energy Environ. Sci.* **2012,** *5* (7), 7913-7917.

85. Yamada, Y.; Okubo, R.; Kinoshita, M.; Niwa, E.; Hashimoto, T.; Tomomichi, K.; Sasaki, K., Prevention of Sulfur Poisoning and Performance Recovery of Sulfur-Poisoned-Anode Electrode by Shifting Anode Electrode Potential. *J. Electrochem. Soc.* **2015,** *162* (10), F1107-F1113.

86. Lohsoontorn, P.; Brett, D. J. L.; Brandon, N. P., Thermodynamic predictions of the impact of fuel composition on the propensity of sulphur to interact with Ni and ceria-based anodes for solid oxide fuel cells. *J. Power Sources* **2008,** *175* (1), 60-67.

87. Wang, J. H.; Cheng, Z.; Bredas, J. L.; Liu, M. L., Electronic and vibrational properties of nickel sulfides from first principles. *J. Chem. Phys.* **2007,** *127* (21).

88. Yap, Y. K.; Inagaki, M.; Nakajima, S.; Mori, Y.; Sasaki, T., High-power fourth- and fifth-harmonic generation of a Nd:YAG laser by means of a CsLiB6O10. *Opt. Lett.* **1996,** *21* (17), 1348-1350.

89. Cheng, Z.; Liu, M. L., Characterization of sulfur poisoning of Ni-YSZ anodes for solid oxide fuel cells using in situ Raman micro spectroscopy. *Solid State Ionics* **2007,** *178* (13-14), 925-935.

90. Dong, J.; Cheng, Z.; Zha, S. W.; Liu, M. L., Identification of nickel sulfides on Ni-YSZ cermet exposed to H-2 fuel containing H2S using Raman spectroscopy. *J. Power Sources* **2006,** *156* (2), 461-465.

91. Cheng, Z.; Abernathy, H.; Liu, M. L., Raman spectroscopy of nickel sulfide Ni3S2. *J. Phys. Chem. C* **2007,** *111* (49), 17997-18000.

92. Thi, H. H. M.; Saubat, B.; Sergent, N.; Pagnier, T., In situ Raman and optical characterization of H2S reaction with Ni-based anodes for SOFCs. *Solid State Ionics* **2015,** *272*, 84-90.

93. Pomfret, M. B.; Owrutsky, J. C.; Walker, R. A., In situ studies of fuel oxidation in solid oxide fuel cells. *Anal. Chem.* **2007,** *79* (6), 2367-2372.

94. Pomeroy, E.; Maza, W.; Steinhurst, D.; Owrutsky, J.; Walker, R., Assessing Sulfur-Induced Degradation Mechanisms in SOFCs with Chronocoulometry and Operando Optical Imaging. *ECS Transactions* **2019,** *91*, 1815-1825.

95. Welander, M. M.; Zachariasen, M. S.; Hunt, C. D.; Sofie, S. W.; Walker, R. A., Operando Studies of Redox Resilience in ALT Enhanced NiO-YSZ SOFC Anodes. *J. Electrochem. Soc.* **2018,** *165* (3), F152-F157.

96. Rasmussen, J. F. B.; Hagen, A., The effect of H2S on the performance of Ni-YSZ anodes in solid oxide fuel cells. *J. Power Sources* **2009,** *191* (2), 534-541.

97. Stoltz, C.; Varughese, B.; Walker, R. A.; Pomfret, M. B.; Stoltz, C.; Varughese, B.; Walker, R. A., Structural and Compositional Characterization of Yttria-Stabilized Zirconia: Evidence of Surface-Stabilized, Low-Valence Metal Species. *ANAL CHEM* **2005,** *77* (6), 1791-1795.

98. Rostrupnielsen, J. R., Chemisorption of Hydrogen Sulfide on a Supported Nickel Catalyst. *J. Catal.* **1968,** *11* (3), 220-+.

99. Prasad, B.; Janardhanan, V. M., Modeling Sulfur Poisoning of Ni-Based Anodes in Solid Oxide Fuel Cells. *J. Electrochem. Soc.* **2014,** *161* (3), F208-F213.

100. Burgess, D., NIST Chemistry Webbook: NIST Standard Reference Database Number 69. In *NIST Chemistry Webbook: NIST Standard Reference Database Number 69*, NIST: 2000.

101. Ong, K. M.; Lee, W. Y.; Hanna, J.; Ghoniem, A. F., Isolating the impact of CO concentration in syngas mixtures on SOFC performance via internal reforming and direct oxidation. *Int. J. Hydrog. Energy* **2016,** *41* (21), 9035-9047.

102. Radenahmad, N.; Azad, A. T.; Saghir, M.; Taweekun, J.; Abu Bakar, M. S.; Reza, M. S.; Azad, A. K., A review on biomass derived syngas for SOFC based combined heat and power application. *Renew. Sust. Energ. Rev.* **2020,** *119*.

103. Somano, V.; Ferrero, D.; Santarelli, M.; Papurello, D., CFD model for tubular SOFC directly fed by biomass. *International Journal of Hydrogen Energy* **2021,** *46* (33), 17421-17434.

104. Papurello, D.; Silvestri, S.; Modena, S., Biogas trace compounds impact on high-temperature fuel cells short stack performance. *International Journal of Hydrogen Energy* **2021,** *46* (12), 8792-8801.

105. Martinez, A.; Gerdes, K.; Gemmen, R.; Poston, J., Thermodynamic analysis of interactions between Ni-based solid oxide fuel cells (SOFC) anodes and trace species in a survey of coal syngas. *Journal of Power Sources* **2010,** *195* (16), 5206-5212.

106. Lanzini, A.; Madi, H.; Chiodo, V.; Papurello, D.; Maisano, S.; Santarelli, M.; Van Herle, J., Dealing with fuel contaminants in biogas-fed solid oxide fuel cell (SOFC) and molten carbonate fuel cell (MCFC) plants: Degradation of catalytic and electro-catalytic active surfaces and related gas purification methods. *Progress in Energy and Combustion Science* **2017,** *61*, 150-188.

107. Etsell, T. H.; Flengas, S. N., Overpotential Behavior Of Stabilized Zirconia Solid Electrolyte Fuel Cells. *J. Electrochem. Soc.* **1971,** *118* (12), 1890-&.

108. Fu, Z. M.; Wang, M. Y.; Zuo, P. J.; Yang, Z. X.; Wu, R. Q., Importance of oxygen spillover for fuel oxidation on Ni/YSZ anodes in solid oxide fuel cells. *Phys. Chem. Chem. Phys.* **2014,** *16* (18), 8536-8540.

109. Hanna, J.; Lee, W. Y.; Shi, Y.; Ghoniem, A. F., Fundamentals of electro- and thermochemistry in the anode of solid-oxide fuel cells with hydrocarbon and syngas fuels. *Progress in Energy and Combustion Science* **2014,** *40*, 74-111.

110. Kee, R. J.; Zhu, H.; Sukeshini, A. M.; Jackson, G. S., Solid Oxide Fuel Cells: Operating Principles, Current Challenges, and the Role of Syngas. *Combustion Science and Technology* **2008,** *180* (6), 1207-1244.

111. Lauvstad, G. O.; Tunold, R.; Sunde, S., Electrochemical oxidation of CO on Pt and Ni point electrodes in contact with an yttria-stabilized zirconia electrolyte - II. Steady-state and impedance measurements. *J. Electrochem. Soc.* **2002,** *149* (12), E506-E514.

112. Matsuzaki, Y.; Yasuda, I., Electrochemical oxidation of H-2 and CO in a H-2-H2O-CO-CO2 system at the interface of a Ni-YSZ cermet electrode and YSZ electrolyte. *J. Electrochem. Soc.* **2000,** *147* (5), 1630-1635.

113. Ong, K.; Hanna, J.; Ghoniem, A. F., Investigation of a Combined Hydrogen and Oxygen Spillover Mechanism for Syngas Electro-Oxidation on Ni/YSZ. *J. Electrochem. Soc.* **2017,** *164* (2), F32-F45.

114. Patel, H. C.; Tabish, A. N.; Comelli, F.; Aravind, P. V., Oxidation of H-2, CO and syngas mixtures on ceria and nickel pattern anodes. *Applied Energy* **2015,** *154*, 912-920.

115. Yurkiv, V.; Utz, A.; Weber, A.; Ivers-Tiffee, E.; Volpp, H. R.; Bessler, W. G., Elementary kinetic modeling and experimental validation of electrochemical CO oxidation on Ni/YSZ pattern anodes. *Electrochim. Acta* **2012,** *59*, 573-580.

116. Bian, L. Z.; Chen, Z. Y.; Wang, L. J.; Li, F. S.; Chou, K. C., Electrochemical performance and carbon deposition of anode-supported solid oxide fuel cell exposed to H-2-CO fuels. *Int. J. Hydrog. Energy* **2017,** *42* (20), 14246-14252.

117. Jin, X. F.; Ku, A.; Verma, A.; Ohara, B.; Huang, K.; Singh, S., The Performance of Syngas-Fueled SOFCs Predicted by a Reduced Order Model (ROM): Temperature and Fuel Composition Effects. *J. Electrochem. Soc.* **2018,** *165* (10), F786-F798.

118. Jiang, Y.; Virkar, A. V., Fuel composition and diluent effect on gas transport and performance of anode-supported SOFCs. *J. Electrochem. Soc.* **2003,** *150* (7), A942-A951.

119. Kuramoto, K.; Hosokai, S.; Matsuoka, K.; Ishiyama, T.; Kishimoto, H.; Yamaji, K., Degradation behaviors of SOFC due to chemical interaction between Ni-YSZ anode and trace gaseous impurities in coal syngas. *Fuel Processing Technology* **2017,** *160*, 8-18.

120. Maza, W. A.; Pomeroy, E. D.; Steinhurst, D. A.; Walker, R. A.; Owrutsky, J. C., Operando optical studies of sulfur contamination in syngas operation of solid oxide fuel cells. *J. Power Sources* **2021,** *510*, 7.

121. Reeping, K. W.; Halat, D. M.; Kirtley, J. D.; McIntyre, M. D.; Walker, R. A. In *In situ optical and electrochemical studies of SOFC carbon tolerance*, Symposium on Ionic and Mixed Conducting Ceramics held during the 225th Meeting of the Electrochemical-Society (ECS), Orlando, FL, May 11-15; Orlando, FL, 2014; pp 57-63.

122. Pomeroy, E. D.; Maza, W. A.; Steinhurst, D. A.; Owrutsky, J. C.; Walker, R. A., Electrochemical Sulfur Oxidation in Solid Oxide Fuel Cells Studied by Near Infrared Thermal Imaging and Chronocoulometry. *J. Electrochem. Soc.* **2020,** *167* (16), 11.

123. Kissinger, P. T.; Heineman, W. R., *Laboratory techniques in electroanalytical chemistry*. 2nd ed.; Marcel Dekker, Inc.: New York, 1996; p xvii, 986 p.

124. *Physical Methods of Chemistry*, *Part 2A, Electrochemical Methods*. John Wiley and Sons, Inc.: New York, 1971; Vol. 1, p 217.

125. Harboe, S.; Sohn, Y. J.; Guillon, O.; Menzler, N. H., Investigation of LSM-8YSZ cathode within an all ceramic SOFC. Part I: Chemical interactions. *Journal of the European Ceramic Society* **2020,** *40* (10), 3608-3617.

126. Rojek-Wockner, V. A.; Opitz, A. K.; Brandner, M.; Mathe, J.; Bram, M., A novel Ni/ceria-based anode for metal-supported solid oxide fuel cells. *Journal of Power Sources* **2016,** *328*, 65-74.

127. Tabish, A. N.; Patel, H. C.; Aravind, P. V., Electrochemical Oxidation of Syngas on Nickel and Ceria Anodes. *Electrochim. Acta* **2017,** *228*, 575-585.

128. Hagen, A., Sulfur Poisoning of the Water Gas Shift Reaction on Anode Supported Solid Oxide Fuel Cells. *J. Electrochem. Soc.* **2013,** *160* (2), F111-F118.

129. He, H. P.; Wood, A.; Steedman, D.; Tilleman, M., Sulphur tolerant shift reaction catalysts for nickel-based SOFC anode. *Solid State Ionics* **2008,** *179* (27-32), 1478-1482.

130. Maier, L.; Schadel, B.; Delgado, K. H.; Tischer, S.; Deutschmann, O., Steam Reforming of Methane Over Nickel: Development of a Multi-Step Surface Reaction Mechanism. *Topics in Catalysis* **2011,** *54* (13-15), 845-858.

131. Haynes, W. M., *CRC handbook of chemistry and physics*. CRC press: 2014.

132. Masson-Delmotte, V.; Zhai, P.; Pirani, A.; Connors, S. L.; Pean, C.; Berger, S.; Caud, N.; Chen, Y.; Goldfarb, L.; Gomis, M. I.; Huang, M.; Leitzell, K.; Lonnoy, E.; Matthews, J. B. R.; Maycock, T. K.; Waterfield, T.; Yelkçi, O.; Yu, R.; Zhou, B. *Climate*

Change 2021: The Physical Science Basis. Contribution of Working Group I to the Sixth Assessment Report of the Intergovernmental Panel on Climate Change IPCC: 2021, 2021.

133. *Annual Energy Outlook 2021*; U.S. Energy Information Administration: 2021.

134. U.S.E.I.A. Average Operating Heat Rate for Selected Energy Sources. https://www.eia.gov/electricity/annual/html/epa_08_01.html (accessed 04/16/2017).

135. Chandan, A.; Hattenberger, M.; El-Kharouf, A.; Du, S. F.; Dhir, A.; Self, V.; Pollet, B. G.; Ingram, A.; Bujalski, W., High temperature (HT) polymer electrolyte membrane fuel cells (PEMFC) - A review. *J. Power Sources* **2013,** *231*, 264-278.

136. Gur, T. M., Critical Review of Carbon Conversion in "Carbon Fuel Cells". *Chem. Rev.* **2013,** *113* (8), 6179-6206.

137. Gur, T. M.; Homel, M.; Virkar, A. V., High performance solid oxide fuel cell operating on dry gasified coal. *J. Power Sources* **2010,** *195* (4), 1085-1090.

138. Shiratori, Y.; Ijichi, T.; Oshima, T.; Sasaki, K., Internal reforming SOFC running on biogas. *Int. J. Hydrog. Energy* **2010,** *35* (15), 7905-7912.

139. Badwal, S. P. S.; Giddey, S.; Kulkarni, A.; Goel, J.; Basu, S., Direct ethanol fuel cells for transport and stationary applications - A comprehensive review. *Applied Energy* **2015,** *145*, 80-103.

140. Ma, Q. L.; Peng, R. R.; Tian, L. Z.; Meng, G. Y., Direct utilization of ammonia in intermediate-temperature solid oxide fuel cells. *Electrochem. Commun.* **2006,** *8* (11), 1791-1795.

141. Ni, M.; Leung, M. K. H.; Leung, D. Y. C., Technological development of hydrogen production by solid oxide electrolyzer cell (SOEC). *Int. J. Hydrog. Energy* **2008,** *33* (9), 2337-2354.

142. Bartholomew, C. H., Carbon Depsotion in Steam Reforming and Methanation. *Catal. Rev.-Sci. Eng.* **1982,** *24* (1), 67-112.

143. Trembly, J. P.; Marquez, A. I.; Ohrn, T. R.; Bayless, D. J., Effects of coal syngas and H2S on the performance of solid oxide fuel cells: Single-cell tests. *J. Power Sources* **2006,** *158* (1), 263-273.

144. Haga, K.; Shiratori, Y.; Ito, K.; Sasaki, K., Chlorine Poisoning of SOFC Ni-Cermet Anodes. *J. Electrochem. Soc.* **2008,** *155* (12), B1233-B1239.

145. Towfighi, J.; Sadrameli, M.; Niaei, A., Coke formation mechanisms and coke inhibiting methods in pyrolysis furnaces. *J. Chem. Eng. Jpn.* **2002,** *35* (10), 923-937.

146. Maier, L.; Schädel, B.; Herrera Delgado, K.; Tischer, S.; Deutschmann, O., Steam Reforming of Methane Over Nickel: Development of a Multi-Step Surface Reaction Mechanism. *Topics in Catalysis* **2011,** *54* (13), 845-858.

147. Bengaard, H. S.; Norskov, J. K.; Sehested, J.; Clausen, B. S.; Nielsen, L. P.; Molenbroek, A. M.; Rostrup-Nielsen, J. R., Steam reforming and graphite formation on Ni catalysts. *J. Catal.* **2002,** *209* (2), 365-384.

148. Trimm, D. L., Coke formation and minimisation during steam reforming reactions. *CATAL TODAY* **1997,** *37* (3), 233-238.

149. Proctor, I. A.; Hopkin, A. L.; Ormerod, R. M., Development of anodes for direct electrocatalytic oxidation of methane in solid oxide fuel cells. *Ionics* **2003,** *9* (3-4), 242-247.

150. Lanzini, A.; Leone, P., Experimental investigation of direct internal reforming of biogas in solid oxide fuel cells. *Int. J. Hydrog. Energy* **2010,** *35* (6), 2463-2476.

151. Pomfret, M. B.; Steinhurst, D. A.; Owrutsky, J. C., Identification of a Methane Oxidation Intermediate on Solid Oxide Fuel Cell Anode Surfaces with Fourier Transform Infrared Emission. *J. Phys. Chem. Lett.* **2013,** *4* (8), 1310-1314.

152. de Arrieta, I. G.; Echaniz, T.; Olmos, J. M.; Fuente, R.; Urcelay-Olabarria, I.; Igartua, J. M.; Tello, M. J.; Lopez, G. A., Evolution of the infrared emissivity of Ni during thermal oxidation until oxide layer opacity. *Infrared Physics & Technology* **2019,** *97*, 270-276.

153. Li, Y.; Xia, X.-L.; Sun, C.; Ai, Q.; Liu, B.; Tan, H.-P., Tomography-based analysis of apparent directional spectral emissivity of high-porosity nickel foams. *International Journal of Heat and Mass Transfer* **2018,** *118*, 402-415.

154. Kirtley, J. D.; McIntyre, M. D.; Halat, D. M.; Walker, R. A., Insights into SOFC Ni/YSZ anode degradation using in situ Spectrochronopotentiometry. *High Temperature Corrosion and Materials Chemistry 10* **2013,** *50* (44), 3-15.

155. Boyle, B. J.; King, E. G.; Conway, K. C., Heats Of Formation Of Nickel And Cobalt Oxides (NiO And CoO) Of Combustion Calorimetry. *J. Am. Chem. Soc.* **1954,** *76* (14), 3835-3837.

156. Rostrup-Nielsen, J. R.; Alstrup, I. B., Ensemble Control By Sulfur Poisoning of Nickel Catalysts for Steam Reforming. In *Studies in Surface Science and Catalysis*, Ward, J. W., Ed. Elsevier: 1988; Vol. 38, pp 725-732.

157. Rostrupnielsen, J., Sulfur-passivated nickel catalysts for carbon-free steam reforming of methane. *J CATAL* **1984,** *85* (1), 31-43.

158. Udengaard, N. R.; Hansen, J. H. B.; Hanson, D. C.; Stal, J. A., Sulfur Passivated Reforming Process Lowers Syngas H2/CO Ratio. *Oil & Gas Journal* **1992,** *90* (10), 62-67.

159. Nikooyeh, K.; Clemmer, R.; Alzate-Restrepo, V.; Hill, J. M., Effect of hydrogen on carbon formation on Ni/YSZ composites exposed to methane. *Applied Catalysis a-General* **2008,** *347* (1), 106-111.

APPENDICES

APPENDIX A

SUPPORTING INFORMATION FOR CHAPTER FIVE

Supporting Information

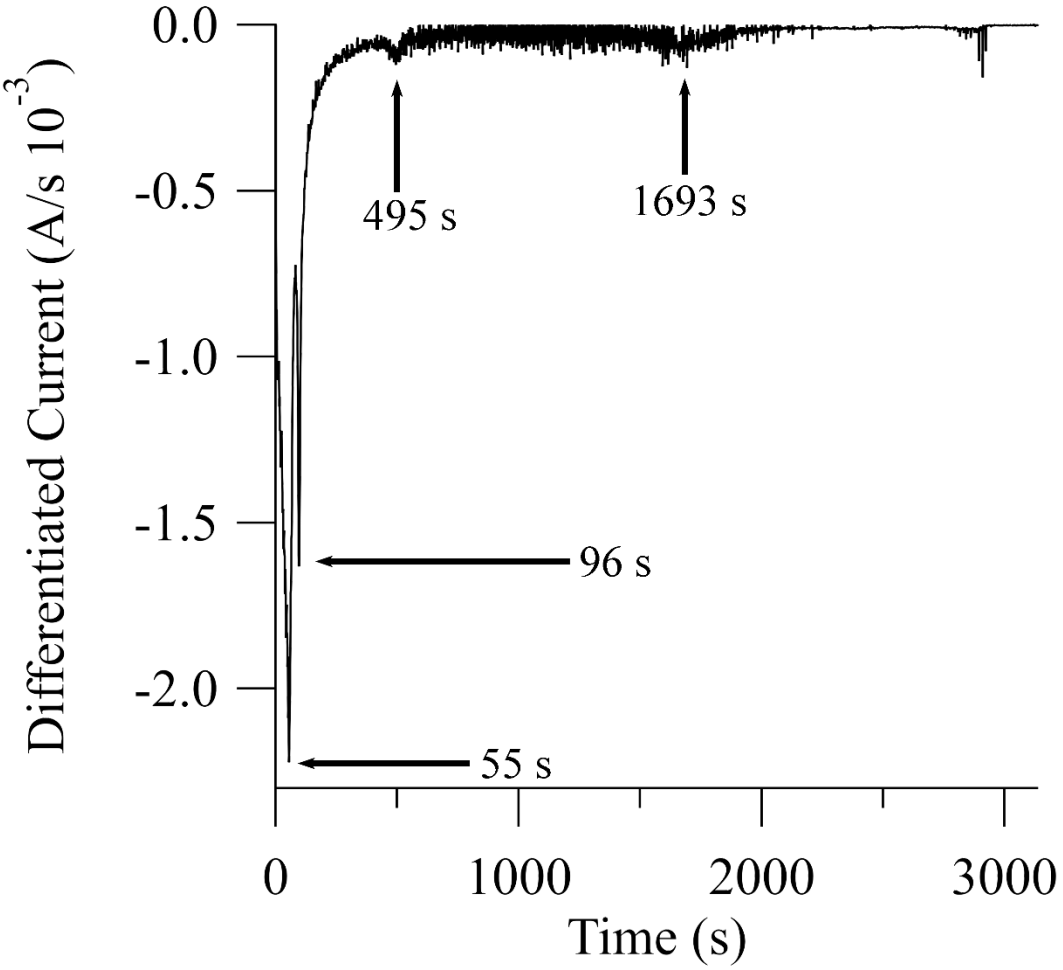

SI Figure 1 During Carbon removal by electrochemical oxidation experiments, inflection points were clear in the chronoamperometry data. To more precisely determine the location of those inflection points, a plot of differentiated current as a function of time was created. Inflection points in current data are peaks in differentiated data, and are indicated by arrows at 55 s, 96 s, 495s, 1693s.

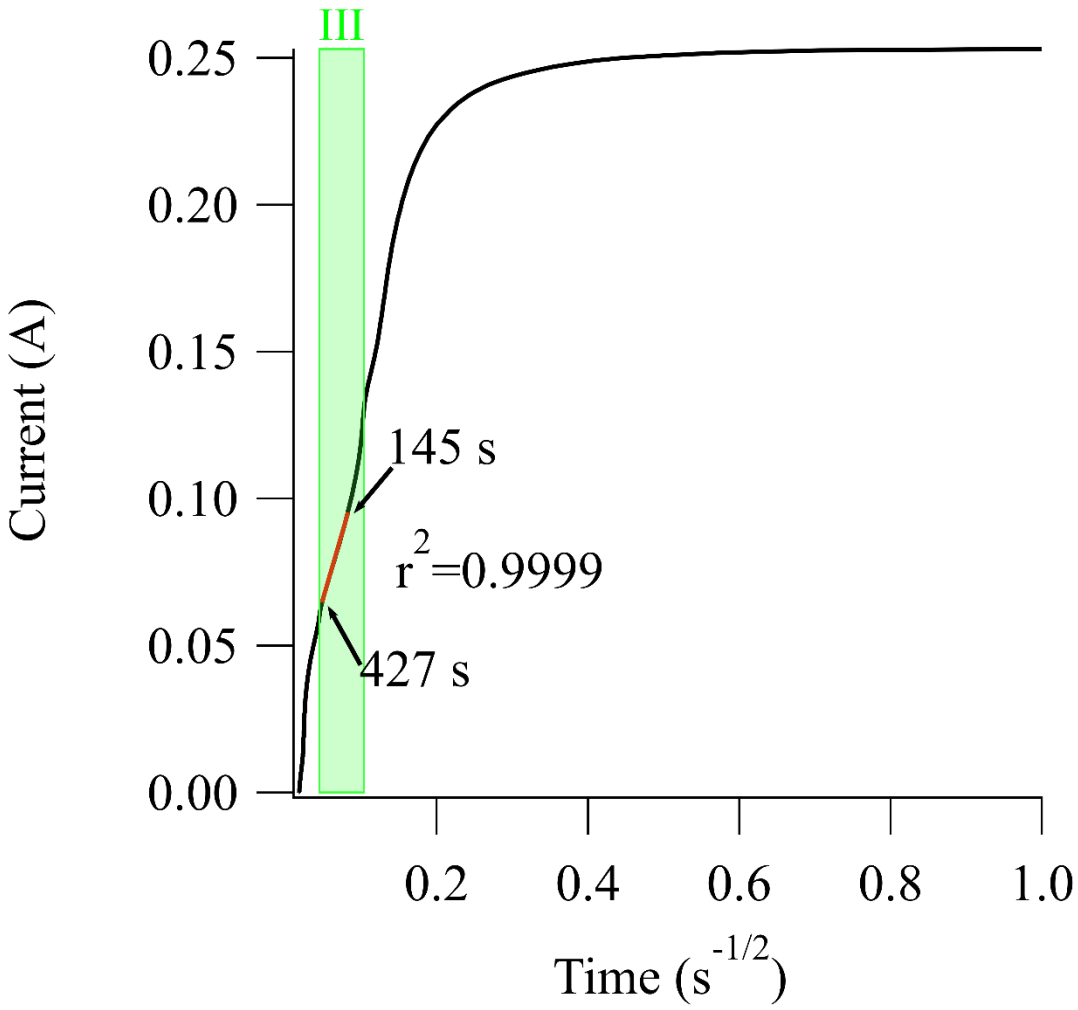

SI Figure 2 During the carbon removal via electrochemical oxidation experiments, CO oxidation was determined to be the fuel during Period II and Period III. Since there must be a change of mechanism between these experiments, a diffusion limited process was proposed to be rate determining during Period III. To validate this proposal, a plot of current as a function of the inverse square root of time was generated, revealing a highly linear region during Period III, within green box. Specifically, the linear region occurred from 127 s to 427 s, well confined by Period III. The near unity linear correlation constant of 0.9999 indicates that a diffusion limited process is indeed rate determining during this time.

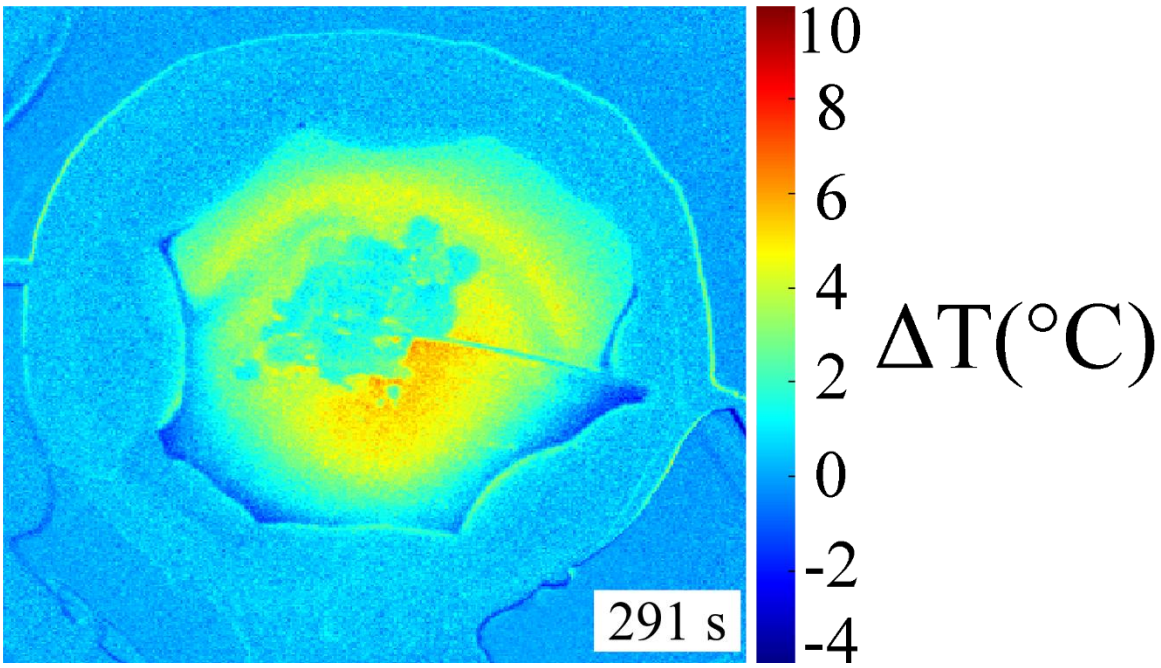

SI Figure 3 During the C removal with molecular oxygen experiments, a clear thermal front forms and moves across the cell during Period II. That linear front is most clear at 291 s in the NIRTI, as seen above. The line across the cell, with cooler areas in front of and behind the line, are strong evidence of this front. This higher resolution NIRTI image, seen here, shows the cell at 291 s, with the false color indicating temperatures as indicated by the bar on the right.

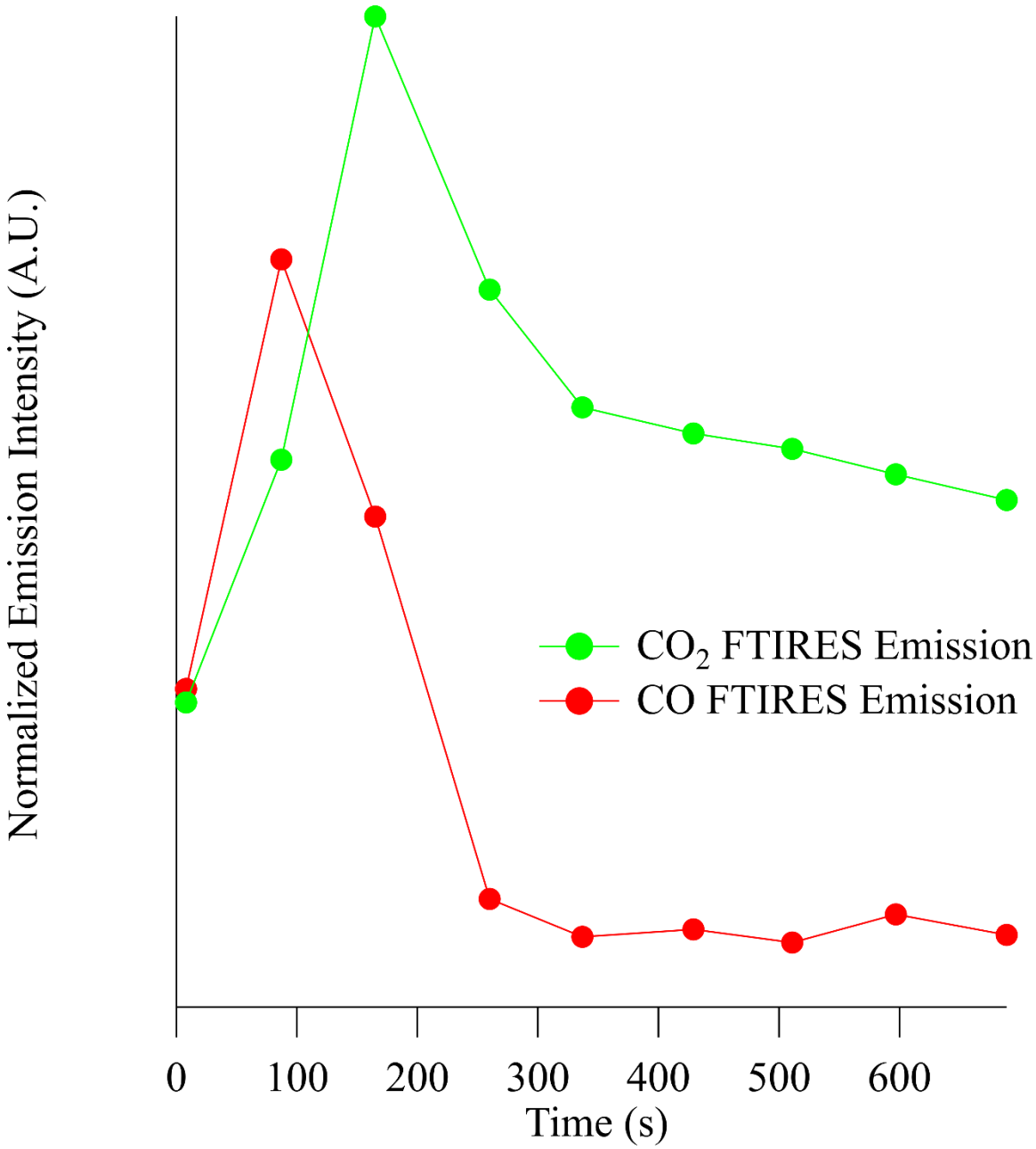

SI Figure 4 During C removal with molecular oxygen FTIRES was performed to monitor CO and CO_2 in the headspace above the cell. Included here, that FTIRES data for CO and emission normalized to peak intensity for each species. The data appeared to match closely to MS data for both species, so was excluded from the original figure for clarity (see Figure 37b).

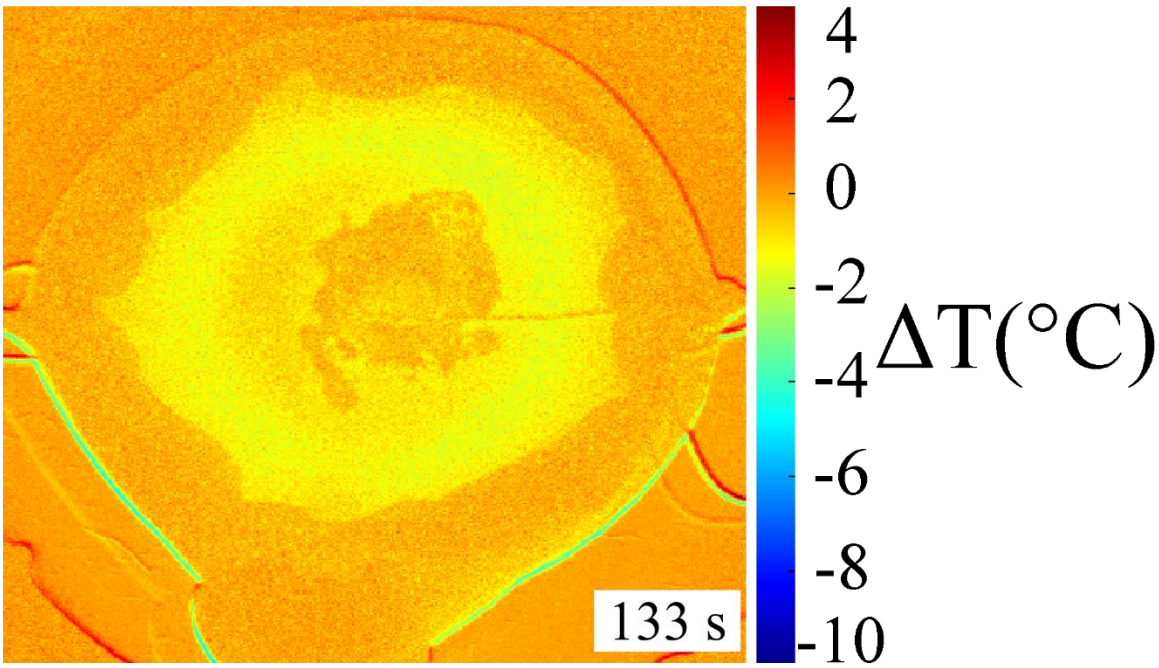

SI Figure 5 During C removal with steam, Period III ended with the area of the cell returning to thermal equilibrium, as measured with NIRTI. The manner in which the remained of the cell warmed was of interest, since a similar, though less dramatic, thermal front formed near the fuel inlet, mostly clearly observed here at 133 s. This higher resolution NIRTI image, seen here, shows the cell at 133 s, with the false color indicating temperatures as indicated by the bar on the right.

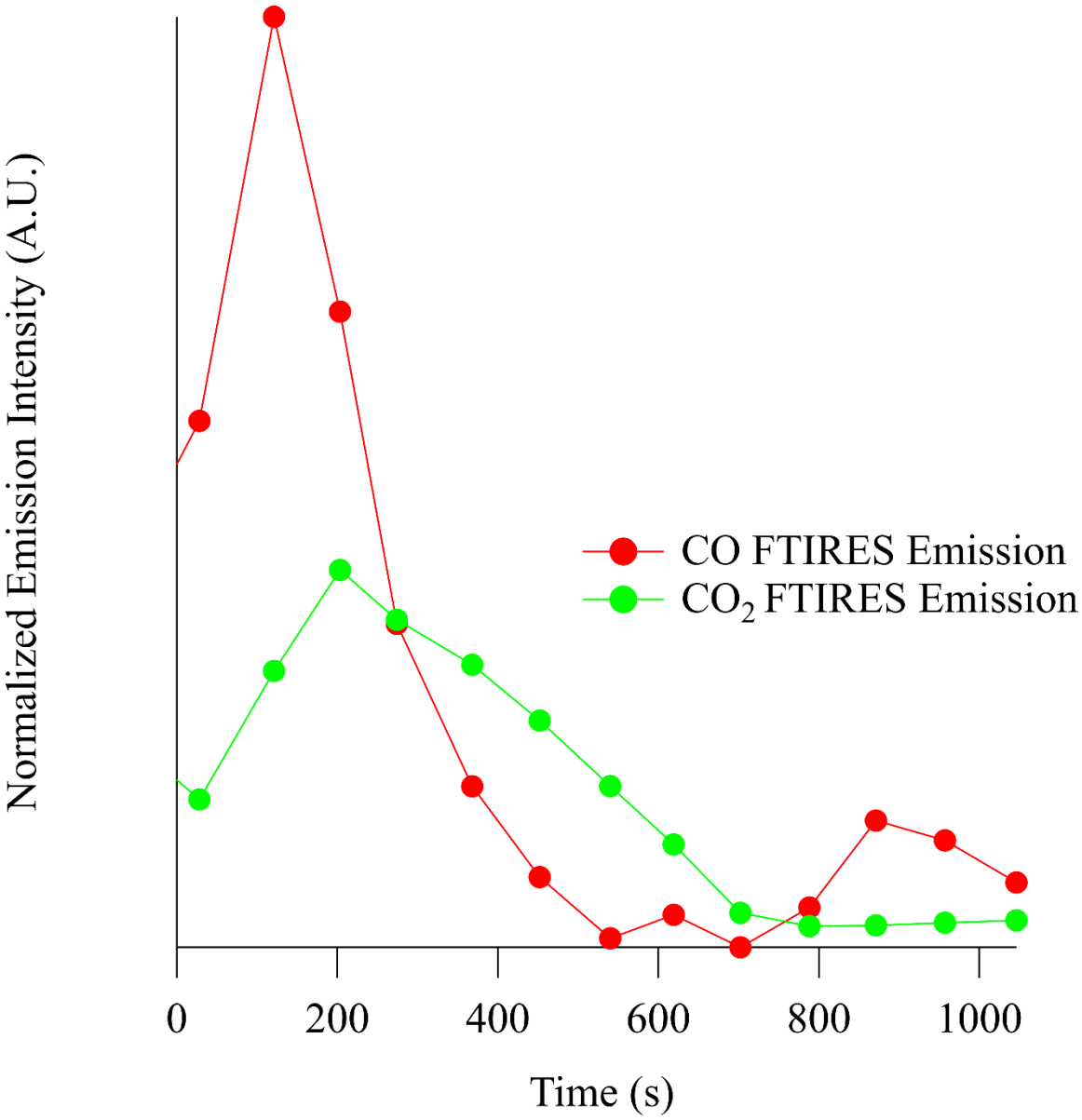

SI Figure 6 During C removal with steam FTIRES was performed to monitor CO and CO_2 in the headspace above the cell. Included here, that FTIRES data for CO and emission normalized to peak intensity for each species. The data appeared to match closely to MS data for both species, so was excluded from the original figure for clarity (see Figure 40b).